**Department of Precision and Microsystems Engineering**

# The Silent Force: Acoustic Trapping in Microfluidics

Exploring the Design and Fabrication of an Acoustofluidic Device for Microbead Trapping and Manipulation

J.M. (Maurits) Wassenaar


| | | |
|---|---|---|
| Report no | : | 2023.103 |
| Coach | : | - |
| Professor | : | Dr. S. (Sabina) Caneva<br>Dr. G.J. (Gerard) Verbiest |
| Specialisation | : | Dynamics of Micro and Nanosystems (DMN) |
| Type of report | : | Master thesis report |
| Date | : | 4 December 2023 |

# Preface

Before you lies my master thesis report about the application of acoustics in a microfluidic platform. This report not only concludes my research project but also marks the end of my graduation program in High-Tech Engineering, a specialization within the master degree Mechanical Engineering at Delft University of Technology. I started my research in September 2022 with a literature study and from February 2023 until now, December 2023, I was engaged in conducting the research and writing this thesis.

Needless to say, I have learned a lot during my studies and I have become increasingly excited about the wide variety of topics that has appeared as the field of mechanical engineering has extended into different disciplines with advancing technology. In contrast with all the interesting lectures of the first part of the degree, in the past year it was up to me to do the research. Along the way I learned about acoustics and piezoelectricity but also gained practical skills in laser cutting, microscopy and data processing. Overall I enjoyed the project. Owing to my supervisors, I had the freedom to follow my curiosity and pursue ideas I picked up. In addition, it was fun to also do more hands-on work in the laboratories and to meet other people who were doing their research. I noticed that many ideas arise from the more unexpected encounters.

This project was of course not an individual effort which is why I would also like to thank the people that supported me along the sometimes bumpy way. First and foremost I thank my supervisors Sabina Caneva and Gerard Verbiest for their guidance. Sabina was a great mentor, by helping me through each stage of the research and by showing she had confidence in the project at times when I had my doubts. Gerard, with his knowledge on acoustics, provided me with key insights and was always happy to discuss a problem I ran into, which subsequently gave new ideas to investigate. I would also like to thank everyone in the Caneva Lab group: Dong Hoon Shin, Xiliang Yang, Ze Yu, Hande Nur Açıkgöz, Yabin Wang, Evi Kesapidou and Mireia Flores Cervello. They provided me with useful feedback and were always happy to help me out in the lab. I furthermore thank the technical support staff for facilitating my research, Jacques Brenkman in particular for his insight into the electrical setup. Lastly, my thanks goes out to Rembrandt, Koen and Jan, for the fun during the much needed breaks when we were co-working, to my brother Arjen and to all other friends and family.

Maurits Wassenaar
Delft, December 2023

# Abstract

Mechanical forces are integral to the functionality and behavior of biological systems, from the cellular to the molecular level. Acoustic force spectroscopy (AFS), an emerging field, seeks to explore these intricate dynamics. Traditional methods in AFS, particularly those using bulk acoustic wave (BAW) devices, still lack sample visibility and have a low throughput. These limitations hinder the amount and type of data that can be gathered in the study of cellular and molecular mechanics. This research project addresses the challenge of enhancing visibility and throughput in AFS by developing a novel BAW device. Here we show the fabrication and implementation of a glass transversal resonator by femtosecond laser ablation and a simple glass-glass bonding technique using polyethylene film and cyanoacrylate glue, which enables two-dimensional particle trapping. Compared to existing BAW setups in AFS, our approach offers improved sample visibility and is capable of positioning particles at arbitrary locations between half- and full-wave mode equilibria by rapid mode-switching. It shows that the position can be predicted using a straightforward method to determine the stiffness of each mode. This advancement of acoustic force spectroscopy could pave the way for new approaches in biomedical research. For example, the ability to alter the force field in a predictable manner allows to form both force- and distance-clamps. More functional BAW devices could thereby not only enhance our understanding of cellular processes but also find broader application in fields like tissue engineering and medical diagnostics.

# Contents

# List of Figures

# List of Tables

# Introduction

While biological research used to be limited to the study of collections of cells and biomolecules like proteins and DNA, it is now possible to investigate the behaviour of the individual molecules. It has been shown that they can be probed by attaching them to micron sized beads. These microbeads can be levitated and steered with sub micrometer precision by means of a magnetic or electric field, or even with light using strong laser beams. Single-cell and -molecule techniques have deepened our understanding of biological processes like DNA transcription and replication, protein and RNA folding, and studies into cell elasticity and the dynamics of motor proteins [2, 4].

Recently, ultrasound has also entered the field of single-molecule biology. While it had already proven itself to be suitable for lab-on-chip applications like particle separation and immobilization [7], it has now been used for molecular force spectroscopy [8]. It was shown that measurement on individual strands of DNA could be performed and that the effect of binding proteins could be observed. The applications are not restricted to individual molecules, also cells can be trapped and investigated, owing to the wide range of forces that acoustics allow. Compared to the other techniques, these so-called acoustic tweezers are an attractive alternative due to their biocompatibility and versatility. Acoustic tweezers in addition have the potential to perform single-molecule experiments with a high-throughput, where many molecules are investigated in parallel. This makes it easier to get statistically significant results, which is more complex and time consuming with existing methods.

Research on the single-molecule level is important as it sheds light on the molecular behaviour and interactions underlying biological processes. For example, protein misfolding and protein phase separation are an important factor in several disease mechanisms [9, 10]. Even though there are ample methods available, the further development of acoustic traps could simplify and speed up future research. In addition, most of the literature on acoustic traps utilize surface acoustic waves (SAW). Bulk acoustic wave (BAW) devices on the other hand are valuable as well and can be manufactured without cleanroom equipment. A gap in the current literature on BAW devices for force spectroscopy is that visualization of the DNA is not yet possible. Applying forces and being able to visualize the sample, for instance through fluorescence imaging, gives additional insight into interactions like protein-DNA dynamics.

This study aimed to develop a new type of BAW device capable of trapping an array of microbeads and manipulating them in-plane. By fabricating the chip using mostly standard lab items, it furthermore means to lower the barrier of adopting BAW techniques.

This thesis report is structured in four sections. The report will start off with an outline of the existing single-molecule manipulation methods and a comparison in Section 1.1. After that, a deeper dive is made into the acoustic tweezers, covering the existing methods as well as a review on the forces driving these techniques. Chapter 3 elaborates on the way the research was conducted. The design process of the chip is discussed including information on the finite element simulations in COMSOL Multiphysics. In addition, the fabrication approach that was used to make the device is covered here. The last parts of the chapter contain the method of bead manipulation and the bead tracking algorithm in Python. The results are presented in Chapter 4. The first part outlines the general layout of the design. This is followed by a conclusion regarding the materials and dimensions, which were derived from insights gained through several finite element simulations. Then, the fabrication method and the subsequent characterization of the device are discussed. The last parts covers a stiffness analysis of the trapped beads and the results from manipulation the beads through mode-switching. The results are then discussed in Section 4.6. Details about the design and fabrication process are given in the appendices.

# Chapter 1

# Literature review

## 1.1 Background

This chapter provides an overview of the relevance of single-molecule biophysics and a summary of state-of-the-art tweezers, including a short comparison. In addition, the physics and working principles of acoustic tweezers are discussed.

### 1.1.1 Relevance of single-molecule techniques

Ensemble average techniques are a commonly used group of techniques in biological research where the collective behaviour of a large number of molecules are investigated. These techniques provide us with valuable information about biological systems as a whole. However, their results do not capture the full complexity of the system: the underlying behaviour and interactions of the individuals that make up the bulk are averaged out and are thus concealed. For a deeper understanding it is therefore necessary to zoom in and probe the individual molecules one by one. Over the last decades, the development of more advanced detection, imaging and manipulation techniques with higher temporal and spatial resolution has opened up the path for research at the single-molecule scale [11].

Single-molecule methods are attractive in biological studies for several reasons. First of all, the direct observation of individual molecules reveals their heterogeneity, which is especially valuable for biomolecules. This is because biological matter is intrinsically meta-stable: biomolecules can be found in a range of free energy states, divided by a few thermal energy units [12]. In addition, the dynamics of single molecules can be measured. In ensemble techniques synchronization is necessary to study kinetics of systems, which is both hard to achieve and maintain. For instance, the synchronization of enzymes dies out quickly due to the stochastic nature of their dynamical transitions [13, 14]. Furthermore, the high sensitivity of these methods allow measurements at lower concentrations, which is useful as true living cell concentrations can then be used. Finally, molecular forces and responses to mechanical manipulation can be quantified in the single-molecule domain [15].

This ability to mechanically manipulate individual molecules has extended our understanding of cellular processes as forces play an important role there. Clear examples are muscle contraction where myosin pulls on actin, and cellular cargo transport where kinesin performs a walking-like motion along microtubules [11] but the involvement of forces in micro- and nanobiology is much broader: in the structure of DNA and RNA and the dynamics of protein folding [15, 16], as well as cellular processes like adhesion, migration, signalling, and sensing, to name a few [4]. A deeper understanding of these phenomena can help us to also get a clearer picture of certain disease mechanisms. Some examples are Parkinson's and Alzheimer's disease, where protein misfolding is the main driver [10]. The multidisciplinary field that does research into the influence of mechanical forces on physiology and diseases is called mechanobiology [4].

### 1.1.2 Tweezing Techniques

To date a wide range of single-particle handling techniques exist. For this type of mechanical manipulation the term 'tweezer' is often used as it serves the same function as a household tweezer to grab tiny objects, though at a much smaller scale. Below, the basic principles and some examples of applications are described for

each technique. Common setups for single-molecule manipulation are optical tweezers, magnetic tweezers and atomic force microscopy. An overview of these configurations is shown in Figure 1.1.

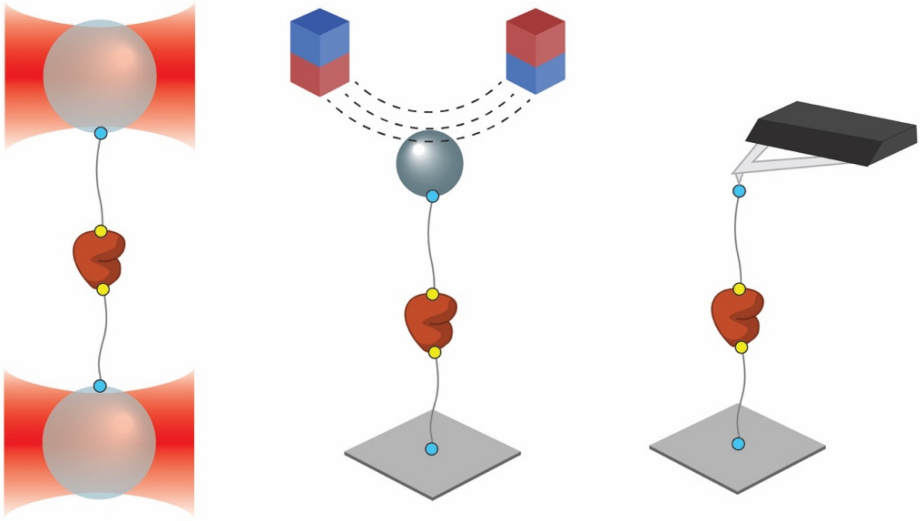

**Figure 1.1:** Overview of common configurations for single-molecule experiments on proteins with (from left to right) optical tweezers, magnetic tweezers and atomic force microscopy (AFM)[1].

### Optical tweezers

In optical tweezers, a tightly focused laser beam is used to trap particles. Light consists of photons that can carry energy and momentum, both linear and angular. The conservation of electromagnetic momentum tells us that light can exert a radiation force on matter when it scatters. To calculate this force, size regimes are often used to make simplifications that give more physical insight. For particles much smaller or much bigger than the wavelength of the light, the dipole or ray optics approximation can be used, respectively.

The dipole approximation technique assumes that the particle can be approximated as small dipoles. The optical force is then decomposed into two main forces: a non-conservative scattering force, which acts in the direction of propagation of the light, a conservative gradient force, which attracts the particle toward the focus. For stable trapping, these forces have to be balanced [17].

In the ray optics approximation, the light is seen as a collection of rays. The rays impinge on a dielectric sphere and are reflected and transmitted at each boundary they meet. Each time the ray is scattered, a change in momentum occurs for that ray. Then, in order for the momentum to be conserved, the object experiences an identical but opposite change in momentum. As the rate of change of momentum equals a force according to Newton's second law, the sum of all scattering events results in a restoring force on the particle's center of mass [3]. A schematic of the forces from both approximations is seen in Figure 1.2.

The resulting force for both approximations can be assumed to be linear around the equilibrium position for small displacements. Accordingly, the optical traps can be modelled by Hook's law for linear springs though their stiffness is not the same for all directions. Furthermore, the spring constants depend on the laser power and how tightly the beam is focused [6].

There is a vast range of optical tweezer setups [3] but all these setups have two elements in common: a high-power trapping laser and a high numerical aperture (NA) microscope objective. The laser beam is first expanded by a telescope and then guided through the high NA objective lens to obtain the steep focus needed to create a diffraction-limited spot. Often, near-infrared lasers are used as they can produce high power beams and mitigate damage to biological samples [2]. A standard setup is shown in Figure 1.2.

For small samples like proteins or RNA molecules, direct trapping is not possible as their interaction with the laser light is not sufficient. Then, micron-sized polystyrene or silica beads which can be trapped are used instead. The sample of interest is tethered to these beads with linker molecules. Often, double-stranded DNA is used for this as its contour length and behaviour is predictable and the maximal force before overstretching makes it compatible for force measurements on proteins. Using linker molecules additionally prevents non-specific interactions between the sample and the trapped bead and protects the sample from the laser beam [1, 2].

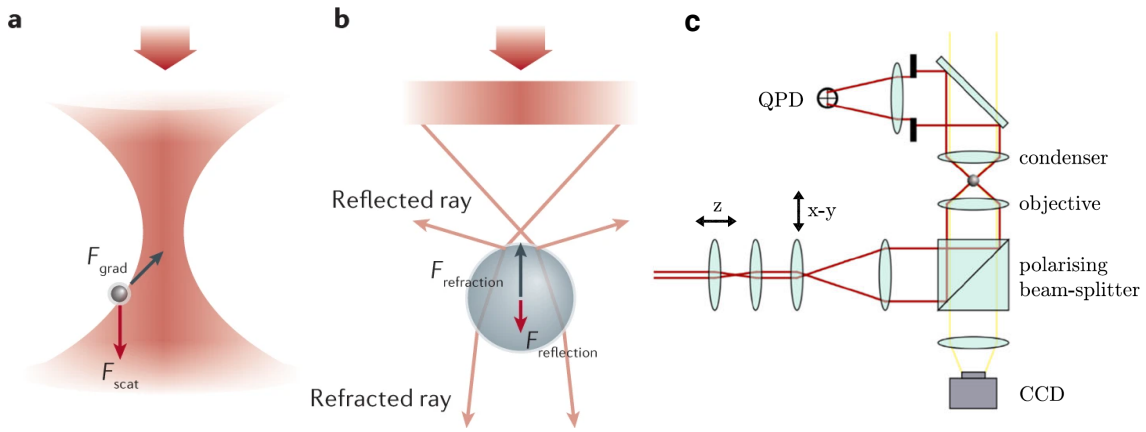


**Figure 1.2: (a)** A schematic from Bustamante et al. [2] that shows the forces derived from the dipole approximation in the case of a Rayleigh particle, which size is much smaller than the wavelength of light (**a**) and from the Ray optics approximation that assumes particles larger than the wavelength of light (**b**). **(c)** An illustration of a single-beam optical tweezer setup with a quadrant photodiode (QPD), which is used to make position measurements on the transmitted laser beam [3].

The first single-beam optical trap was developed in 1986 by Ashkin et al. [18]. Since then the technique has been applied widely. Zhao et al. [17] provide a short overview of topics that have been researched: the elastic properties of single and double stranded DNA which yielded force-extension curves [19]; protein folding dynamics that acquired data about folding rates and transient states [20, 21]; motor proteins like kinesin that revealed their ATP hydrolization mechanism [22]; and RNA polymerase which synthesizes RNA by moving along a strand of DNA [23].

### Atomic force microscopy

Atomic force microscopy (AFM) is a type of scanning probe microscopy (SPM) where the surface of a sample is probed to generate of topographic map. This is done by measuring the forces between a sharp tip and the sample surface as they are brought in close proximity to each other. At these distances, a variety of attractive and repulsive interactions like Van der Waals and Coulomb forces arise. The tip is attached to the free end of a compliant cantilever that deflects as a result of these forces. This leads to a displacement of the tip determined by Hooke's law of linear springs. By shining a laser beam on the back of the cantilever its deflection can be measured through the projection of the reflected beam onto a position-sensitive photodiode. A piezoelectric motion stage is used to move the sample in three dimensions with sub-nanometer precision. In Figure 1.3a a typical AFM setup can be seen.

The AFM was invented by Binnig et al. in 1986 [24] in view of the need for imaging nonconductive surfaces, which was not possible with the scanning tunnelling microscope. AFM has also proven to be a valuable method in force spectroscopy as it allows to manipulate individual cells and molecules [6]. The AFM tip is then fixed to the sample of interest and moved vertically via the motion stage to obtain force displacement curves or position profiles of the actuator when operating the setup as a force clamp. Common linker molecules are polyethylene glycol (PEG) polymers as they are more flexible than DNA linkers and can withstand higher forces [1]. This has been used for investigating molecular bonds, from step-wise unfolding or refolding of proteins [25] to covalent bonds [26], receptor-ligand interactions [27] and nucleic acids [28], as summarized by Neuman and Nagy [6].

### Magnetic tweezers

The working principle behind magnetic tweezers is that a force can be applied on magnetic particles that are placed in a magnetic field. Most commonly, super-paramagnetic beads are used which are collections of magnetic particles, around 10 nm to 20 nm in size, held together by a polymer. They are an attractive choice due to their high magnetic susceptibility and zero remnant magnetization. This is caused by the small size of the magnetic domains. In the absence of a magnetic field, the orientation of the magnetic domains will be randomly distributed by thermal fluctuations. The force on super-paramagnetic beads is proportional to and in the direction of the field gradient. In addition, it scales with the particle's volume. Next to the magnets

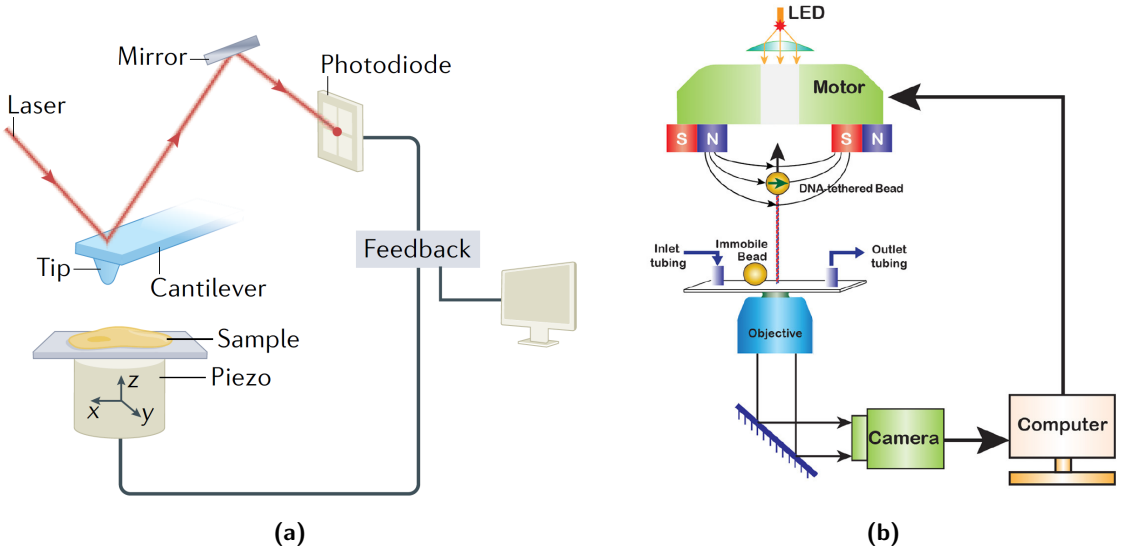


**Figure 1.3:** (a) Schematic overview from Viljoen et al. [4] of an AFM setup. (b) Magnetic tweezer setup with permanent magnets, adapted from Sarkar et al. [5].

and the flow cell, a basic setup consists of only a few other components: a motorized drive that moves the magnets to change the force field and a microscopy for monitoring the bead's position [5]. A schematic of a typical setup is shown in Figure 1.3b. For creating the magnetic field, permanent magnets or electromagnets have been implemented.

Setups with permanent magnets are attractive for their simplicity. In such a device, two permanent magnets, a few millimeter in size, are separated by a small gap. The field gradient, and thus also the force on the particle, increases proportionally as the gap size decreases and changes little over the length scale of the needed bead displacements. No force minimum exists so the beads have to be fixed to a surface using for example DNA tethers [29]. A schematic of the permanent magnet tweezer setup can be seen in Figure 1.3b.

Instead of permanent magnets also electromagnets can be used. The current through the coils then generate the magnetic field that controls the force. As with permanent magnets, there is no passive and stable equilibrium position in which the bead is trapped. Instead, feedback control is needed to constantly alter the force field and hold the beads in place. The characteristics of this feedback loop determine the effective trap stiffness [11, 30].

Magnetic tweezers have been used in a range of experiments [6, 17, 31]. For instance, the mechanical properties of supercoiled DNA and the activity of topoisomerase, an enzyme that plays a role in the regulation of DNA supercoiling, have been studied. Furthermore, the mechanism of DNA transcription using RNA polymerase has been studied, which led to the discovery of the transcription initiation process [32]. Also, research into condensins, proteins that contribute to chromosome organization, was performed using magnetic tweezers [33]. Aside from DNA research, magnetic tweezers have also been applied in protein folding, collagen proteolysis and mechanotransduction studies, as summarised by Sarkar and Rybenkov [5].

### Acoustic tweezers

Another method to trap particles is by means of acoustic waves, the main topic of this report. In essence, acoustic waves are mechanical pressure waves and can travel through gasses, liquids and solids. They are governed by equations for momentum and the conservation of mass and energy [36]. There are two types of waves, longitudinal and transversal, depending on the direction of the medium oscillation compared to the wave propagation (parallel and perpendicular, respectively) (Figure 1.4b). Furthermore, acoustic waves can be superimposed, forming standing waves. The manipulation of particles can be achieved directly through the acoustic radiation pressure, and indirectly through acoustic streaming of the fluid. Both these driving mechanisms are second order, nonlinear effects [37]. Aside from the microfluidic cell, a typical setup is shown in Figure 1.4a and consists of a piece of piezoelectric material, which is used to generate the acoustic waves, a function generator (optionally with an amplifier) and a microscope to track the position of the sample of interest. Applications of acoustic tweezers will be discussed in Section 1.2.1.

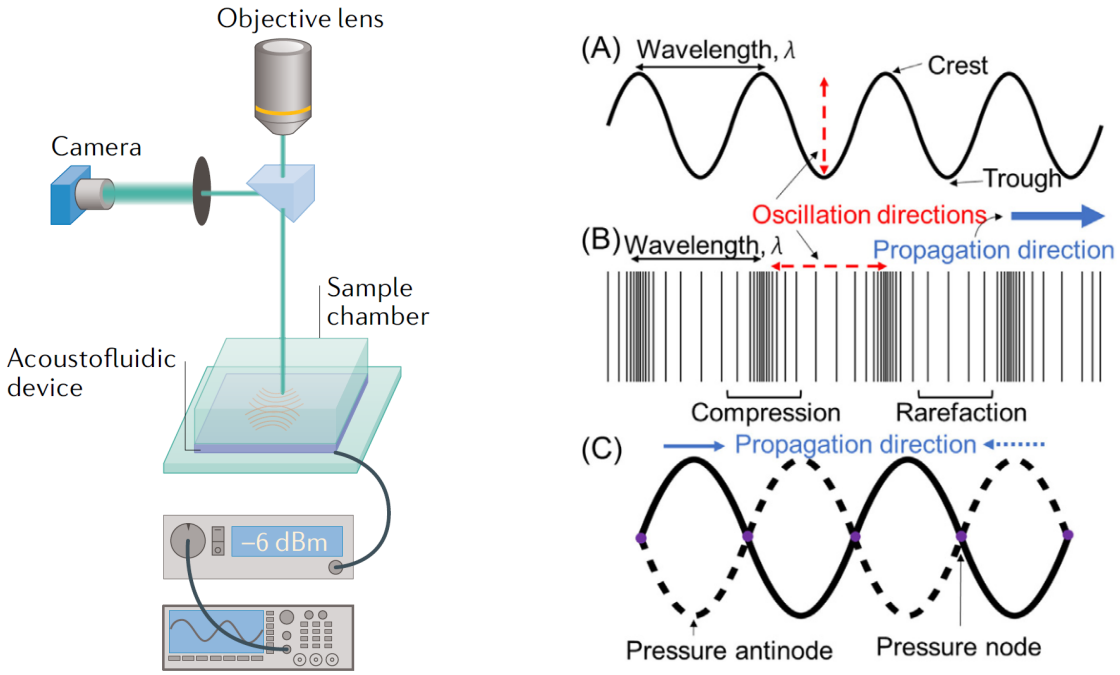


(a) (b)

**Figure 1.4:** (a) Typical setup of an acoustic tweezer, including a function generator, amplifier and an imaging system, adopted from Rufo et al. [34]. (b) Schematic from Ozcelik et al. [35] showing the propagation of transverse (A) and longitudinal (B) acoustic waves. In addition the formation of a standing wave by two counter-propagating waves is illustrated (C).

### Comparison

It is useful to compare acoustic tweezers to the other techniques to get an idea of their differences in performance. Table 1.1 is adapted from Neuman and Nagy [6] and gives an overview of some specifications.

**Table 1.1:** Comparison of specification of several tweezing techniques, adapted from Neuman and Nagy [6].

| | **Optical tweezers** | **(Electro)magnetic tweezers** | **AFM** | **Acoustic tweezers** |
|---|---|---|---|---|
| Spatial resolution (nm) | 0.1-1 | 5-10 (2-10) [38] | 0.5-1 | $10^3$-$10^4$ [38, 39] |
| Stiffness (pN nm$^{-1}$) | 0.005-1 | $10^{-3}$-$10^{-6}$ ($10^{-4}$) | 10-$10^5$ | $10^{-3}$-5 [40, 41], |
| Force range (pN) | 0.1-100 | $10^{-3}$-$10^2$ (0.01-$10^4$) | 5-$10^5$ | 10-$10^4$ [42] |
| Displacement range (nm) | 0.1-$10^5$ | 5-$10^4$ (5-$10^5$) | 0.5-$10^4$ | $10^3$-$10^6$ [37, 39, 43] |

It can be seen that acoustic tweezers have a similar performance in some specifications. Firstly, they have a force range that is similar to AFM and are thus also able to probe biomolecular forces like receptor-ligand and DNA overstretching as well as stronger covalent bonds and cell adhesion [4, 6]. Additionally, the stiffness of acoustic tweezers is higher than magnetic tweezers. This is because the magnetic force field is almost constant on the micrometer scale [37]. Compared to optical tweezers the stiffness is similar. From the table also some downsides are apparent. One drawback is that controlled forces lower than a few piconewtons have not been achieved. Next to that, the displacement range as well as the spatial resolution are in the order of micrometers whereas the other techniques are able do manipulations with nanometer precision.

Apart from the technical specifications there are other aspects that should be considered to complete the comparison. These are discussed below.

**Biocompatibility** In comparison, acoustic tweezers have some features that makes them more biocompatible. As direct contact with the sample like in AFM is not needed, potentially damaging impact or surface

adsorption is avoided and heat conduction to the sample is reduced. Furthermore, acoustic tweezers employ acoustic power ($10^{-2}$-10 W/cm$^2$) and frequencies (1 kHz to 500 MHz) of approximately the same magnitude as those applied in ultrasonic imaging, a safe diagnostic technique that is applied widely. In contrast, the laser beam of an optical trap can on the other hand damage the biological samples through heating and photodamage [44, 45]. Electromagnetic tweezers can also be damaging when strong magnetic fields are needed. Large currents then heat up the coils which can also affect the sample [6].

However, as pointed out by Wiklund [46], this should not be taken as a guarantee that ultrasound is never harmful. The literature on acoustic manipulation regularly mentions biocompatibility as a strength of acoustics compared to other techniques and this has been shown to be true in terms of cell viability and proliferation [47]. It should however be pointed out that there is evidence of altered cell behaviour in some cases of cell analyses [48]. Additionally, heating and cavitation can be damaging to cells and biomolecules. Even though these effects are not always present or harmful they should be considered nonetheless.

**Versatility** As summarized by Zhang et al. [49] acoustic microfluidic devices have excellent versatility. First of all, they are able to manipulate objects sizing from 100 nm up to 10 mm. Even biological objects like cells, small organisms like C. elegans and exosomes can been handled [38]. Acoustic tweezer setups can be scaled up into macrofluidic applications. This enables it to be used in applications like tissue engineering, drug discovery and blood transfusions [38]. In contrast, magnetic tweezers are only able to handle sizes up to several tens of micrometers [38]. Next to that, there are no constraints on material properties, whereas optical and magnetic traps respectively need dielectric and magnetic particles.

Furthermore, many particles can be manipulated in parallel. This is conducive to get statistically significant results more quickly, which is relevant due to the heterogeneity in both static and dynamic properties across the cells and molecules in the sample. This is harder to achieve with optical traps and especially in AFM. There, direct contact is needed and it is difficult to attach the tip to the right molecule at the right spot [6]. Moreover, due to due to the large tip size, nonspecific binding or the interaction between the tip and the sample surface or surface contaminants make the interpretation of the results more complicated. Magnetic traps are an exception and have been used for high-throughput experiments with several hundreds of beads [50, 51].

Finally, acoustic traps allow both translational and rotational motion. This is not the case for magnetic tweezers, except for electromagnetic tweezers though they require complex feedback control. [5, 29].

**Setup** There is also a benefit to acoustic tweezers regarding the setup. Next to the chip itself, only a signal generator, an oscilloscope and an amplifier are needed. This is relatively common lab equipment and the setup is quite simple in comparison with optical tweezers. Those setups require a high-powered laser, high NA objectives and complex optics, which also drive up the costs [49].

## 1.2 Acoustic tweezers - an in-depth view

The first steps of research into acoustic traps were made in the 1930s by the investigation of the acoustic radiation force on spherical bodies [52] and the coagulation of emulsions [53]. In the 1990s the use of focused transducers and acoustic levitation of mammalian cells in liquid [54] were investigated. Later, miniaturization of piezoelectric transducers sparked new interest as it enabled the implementation of acoustic traps on-chip [37]. This chapter dives deeper into the existing literature on acoustic tweezers, including a brief overview of the physics that is involved.

### 1.2.1 Existing acoustic manipulation techniques

There are several different types of acoustic tweezers which can roughly be divided into three main categories: standing-wave, traveling-wave and acoustic-streaming tweezers. The first two techniques directly manipulate the particle through the acoustic radiation force, whereas acoustic-streaming tweezers use the fluid's drag force.

Standing-wave tweezers can create strong-gradient acoustic fields as they comprise the sum of multiple wave fields. These fields can be created with a single transducer and a reflector or with multiple transducers. Forces in both directions along the wave propagation direction exist. One downside is that only collective manipulation is possible, so particles can not be moved independently of each other.

Travelling waves devices only have one acoustic source and produce much weaker radiation forces. For stronger field gradients they rely on focusing of the wave front [55]. Due to scattering of the incident beam on the particle they push the particles in the wave propagation direction, which does not give them ability to trap particles [37]. The difference between standing and traveling waves can be seen in Figure 1.5a.

Acoustic streaming is the effect of an induced flow due to the absorption of acoustic energy [38] and is dominant for smaller particles [56]. This flow can then manipulate particles indirectly through the viscous drag. Applications of microfluidic streaming include pumping and mixing [35]. There are several methods to create streaming flows. A few of them are shown in Figure 1.5b. Drawbacks of these devices is their low spatial resolution and the fact that streaming is less well understood.

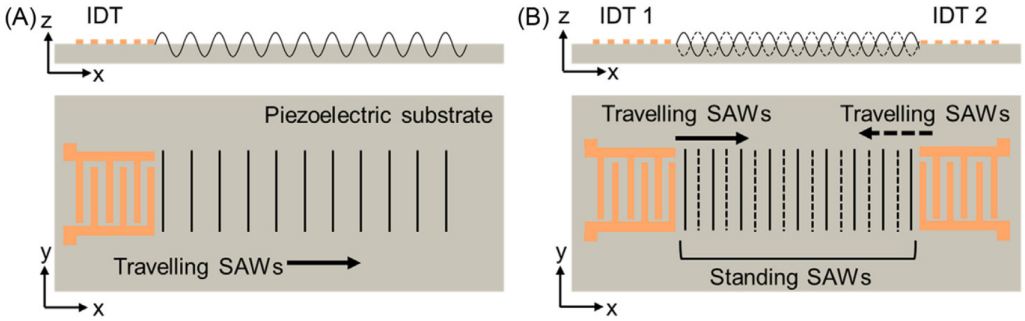


**(a)** Schematic showing the difference for traveling (A) and standing (B) waves, in this case for surface acoustic waves (SAW).

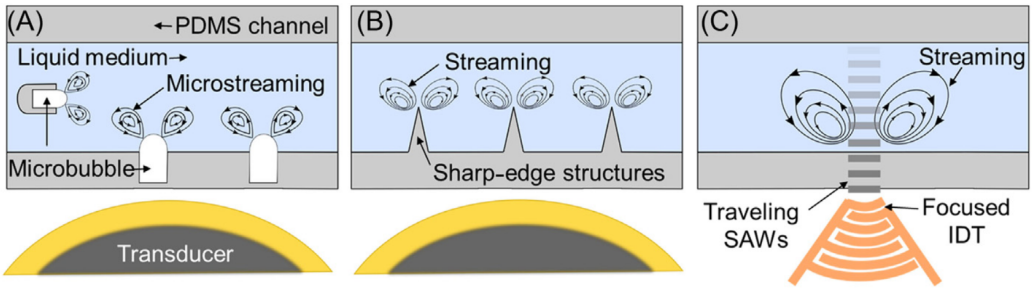


**(b)** Different types of acoustic streaming devices. A piezoelectric transducer can be used to create streaming vortices using microbubbles (A) or sharp edges (B). In (C) a focused traveling SAW creates streaming.

**Figure 1.5:** Schematics form Ozcelik et al. [35] showing the difference between traveling and standing surface acoustic waves (SAW), and acoustic streaming devices.

The focus of this report will be on standing-wave tweezers as they can attain strong-gradient fields more easily, are compact, and easy to implement in microfluidic devices [55]. There are two main types of tweezers that employ standing waves: bulk and surface acoustic wave tweezers, BAW and SAW, respectively. These are illustrated in Figure 1.6. Their working principle and applications are discussed below.

### Standing bulk acoustic wave (SBAW) devices

In bulk acoustic wave devices the standing wave field is created in the fluid medium. Piezoelectric ceramic transducers are used to generate thickness or lateral vibration modes which are coupled to the fluidic chamber. The standing wave can either be produced by a combination of a transducer and a reflector or by two opposing transducers. The former relies on the cavity resonant modes whereas the latter needs a calibration of the phases between the transducers to attain constructive interference. In both cases it is common to drive the transducer at its resonance frequency as this minimizes the needed power input. This transducer resonance depends on the piezoelectric material and its size [57], where smaller transducers can obtain higher frequencies. BAW devices typically operate below 10 MHz which corresponds to wavelengths of 150 µm and above [55].

### Standing surface acoustic wave (SSAW) devices

As their name suggests, surface acoustic waves travel along the surface of a medium as opposed to BAW that travel through the bulk. They were first discussed by Lord Rayleigh in the late nineteenth century [58]. In microfluidics, a SAW device comprises of a piezoelectric substrate on which periodic sets of metallic fingers called interdigital transducers (IDTs) are deposited. By applying an alternating electric field, strain is created in the substrate which generates a wave with a wavelength determined by the spacing between the IDTs [59]. The wave amplitude decreases rapidly with depth so the acoustic energy is concentrated in the surface, which minimizes the required input power. A portion of the energy is converted into sound when a fluid layer is introduced, which then creates the desired pressure distribution. Common piezoelectric materials are single-crystal bulk lithium niobate or a thin film of poly-crystalline zinc oxide. Similar to BAW devices, standing waves can be created by using an IDT and a reflector or two opposing IDTs [34]. Frequencies of acoustofluidic SAW devices from 10 MHz up to 1 GHz have been used, resulting in wavelengths below 100 µm.

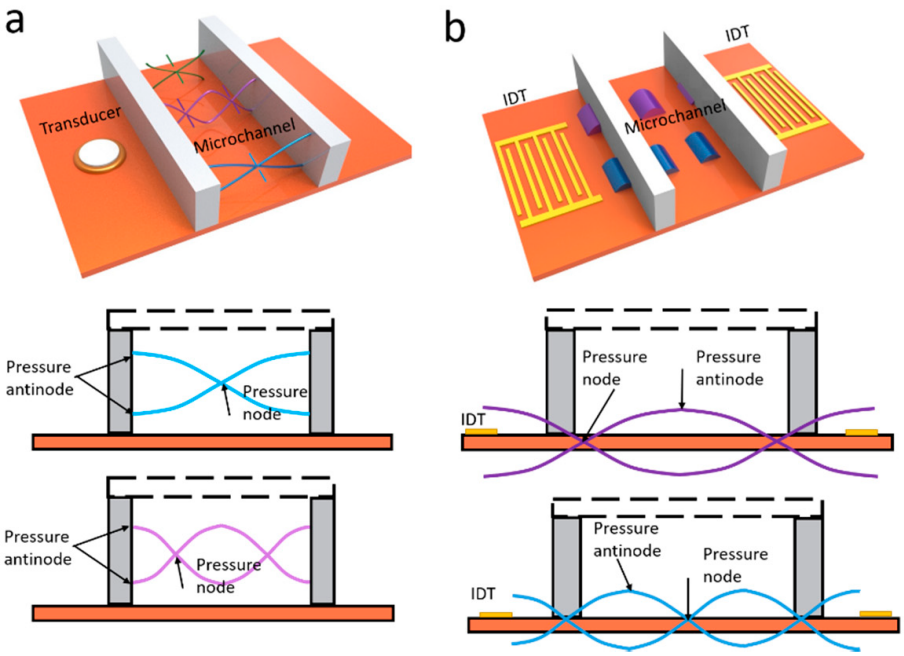


**Figure 1.6:** Illustration from Gao et al. [60] that shows the difference between BAW (a) and SAW (b), where the standing wave is created in the fluid and the substrate, respectively.

### Microfluidic applications of acoustics

Acoustics has found a myriad of applications in microfluidics: from mixing by acoustic streaming to droplet generation by vibrating micropillars, and from maneuvering model organisms like *Caenorhabditis Elegans* to propelling microswimmers. Acoustofluidics techniques can contribute in many areas of biomedical research: in drug discovery and delivery, in clinical diagnostics, immunoassays [55] and in understanding biological phenomena like disease mechanisms [57]. The main implementations of acoustic waves in microfluidic devices can be broadly grouped as continuous-flow and acoustic trapping platforms.

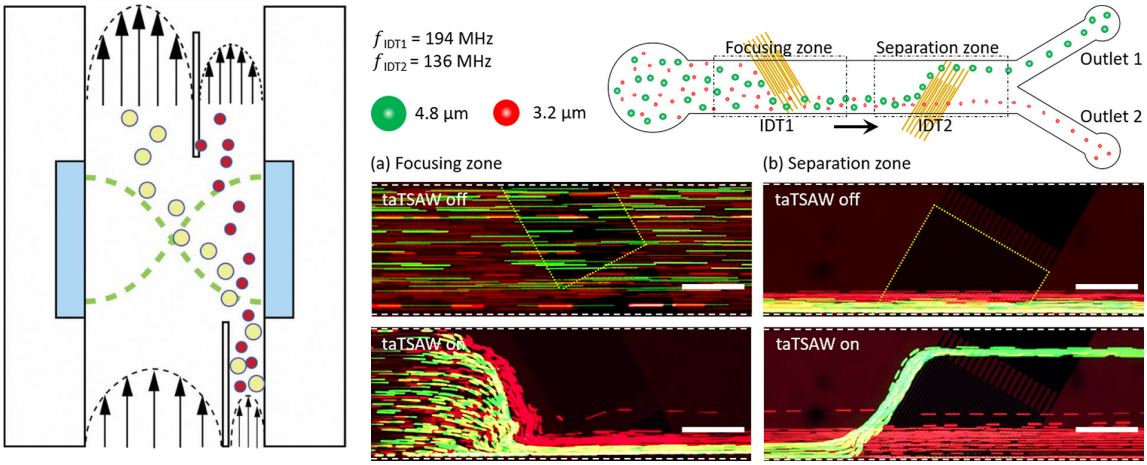


**Figure 1.7:** (a) Acoustic sorting in a BAW device, adapted from Lenshof et al. [47] and based on research by Johnson and Feke [61]. (b) Illustrations and images from Ahmed et al. [62] showing how traveling SAW can separate particles based on size, scale bar 250 µm

Continuous-flow implementations include the alignment, separation and sorting of particles in a fluid that is steadily flowing. One application is focusing particles in a flow cell using a standing wave. This can be used for high-throughput cell imaging [63] or, in the case of flow-cytometry, for spectral analysis. In the latter, acoustics provide a cheap and simple alternative to the often costly and bulky commercial variants [57]. Particle separation and sorting is another application of acoustics and is important in clinical studies, chemical analysis and biological research. Both BAW and SAW are used for this and have advantages of being non-contact, label-free and high efficiency. Separation can be done based on a difference in size, density and compressibility [47]. Their performance is similar to common techniques like fluorescence-activated cell sorting (FACE), which conventionally uses an electric field as external force and has a high throughput, but requires less complex and expensive equipment. Acoustic sorting has been used for separation of red and white blood cells, bacteria, cancer cells and viruses, which is important in disease diagnostics. An illustration of acoustic separation in a SAW device is shown in Figure 1.7a, which shows the separation of particle based on their size. As the larger red particles experience a larger force, they move faster toward the pressure node.

Next to continuous-flow applications, acoustic trapping is another application which entails the immobilisation and control of particles and cells [7], shown in Figure 1.8a. One example is cell patterning where cells are trapped into the pressure nodes or anti-nodes of the acoustic field, which makes it appealing for applications like tissue engineering. Gesellchen et al. [65] for example showed they were able to pattern Schwann cells to guide the direction of neurite outgrowth (Figure 1.8b). Furthermore, this mono-layer patterning can be extended into three dimensions, which then more closely resembles native conditions. This method is less time-consuming as standard methods like gyratory rotation and there is in addition no need for a scaffold [7]. Furthermore, patterning can also be used for cell washing or enriching, where the buffer fluid can be changed while the particles are trapped, and material assembly for fabricating complex composites by for example aligning fibers. [7, 55, 66].

## 1.2.2 Standing bulk acoustic wave (SBAW) devices

The scope of the remainder of this report is BAW devices. The main argument for this is the very low cost of producing prototype BAW devices. SAW devices generally attain higher particle manipulation precision

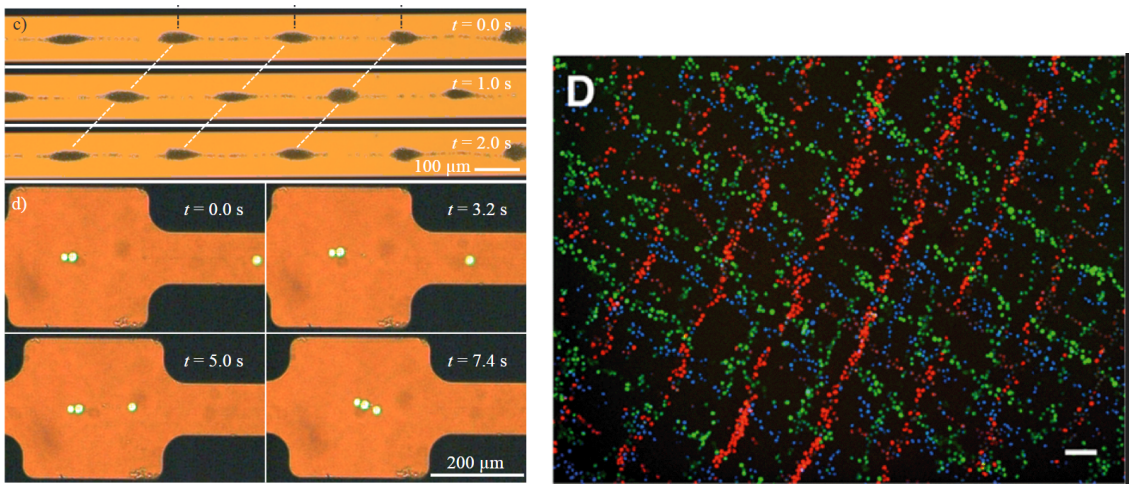


**(a)** **(b)**

**Figure 1.8:** Acoustic trapping examples. (a) BAW setup from Manneberg et al. [64] where particles can be aligned, transported and trapped. (b) Picture from Gesellchen et al. [65] of fluorescently labeled C2C12 cells that shows the direction of neurite outgrowth could be controlled, scale bar 100 µm

due to their higher frequencies, resulting in smaller wavelengths. However, this comes at the cost of higher manufacturing complexity: to fabricate the IDTs, photolithography and metal deposition is needed in addition to cleanroom facilities [57]. The most basic BAW devices can on the other hand be produced by hand with standard piezoelectric transducers and relatively simple bonding techniques.

### Working principle

The three dominant forces in acoustofluidic devices are the primary and secondary radiation force and the drag forces associated with acoustic streaming. In addition, the basic principle and formulas of piezoelectric transducers are given.

**Primary acoustic radiation force (PRF)** Particles immersed in a fluid (or gas) that is subjected to an ultrasound field experience a so-called acoustic radiation force (ARF). The following section follows the derivation given in the Acoustofluidics Tutorial series [67, 68]. As explained by Bruus [68], the derivation of the acoustic radiation force started with the analysis of incompressible particles in acoustic fields by King in 1934 [52], later extended to compressible particles by Yosioka and Kawasima [69], and summarized in 1962 by Gor'Kov [70]. The starting point is an expression for the thermodynamic equation of state of the pressure $p$ as a function of the density $\rho$, an equation for the density representing the kinematic continuity equation, and the Navier-Stokes equation.

$$p = p(\rho) \tag{1.1a}$$

$$\frac{\partial \rho}{\partial t} = -\nabla \cdot (\rho \boldsymbol{v}) \tag{1.1b}$$

$$\rho \frac{\partial \boldsymbol{v}}{\partial t} = -\nabla p - \rho(\boldsymbol{v} \cdot \nabla)\boldsymbol{v} + \eta \nabla^2 \boldsymbol{v} + \beta \eta \nabla(\nabla \cdot \boldsymbol{v}) \tag{1.1c}$$

Here, $\boldsymbol{v}$ is the velocity, $\eta$ the dynamic viscosity and $\beta$ the viscosity ratio, which is approximately 5/3 for water. All external fields like gravity are neglected, as well as heat transfer.

Although it is difficult to solve the set of equations (Equation (1.1)) analytically, perturbation theory can provide adequate approximate solutions. Thereafter, the radiation force on a spherical and compressible particle suspended in an inviscid fluid can be determined. It is furthermore assumed that the particle's radius $a$ is much smaller than the acoustic wavelength $\lambda$ so it acts like a weak point-scatterer, which enables the use of first order scattering theory. For somewhat larger particles with diameters of the same order as the wavelength, the forces will somewhat differ but numerical methods should still provide good estimates [71].

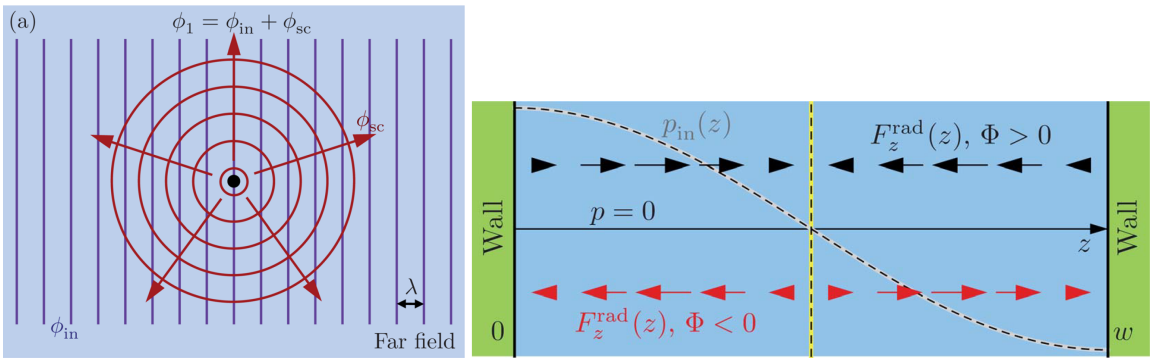


**(a)** **(b)**

**Figure 1.9:** Schematics from Bruus [68]. (a) The first-order wave $\phi_1$ is the sum of the incoming $\phi_{in}$ and the scattered field $\phi_{sc}$. (b) Depending on the sign oft the contrast factor $\Phi$ the radiation force is directed to the pressure node (black) or antinode (red).

When the incident wave reaches the particle, it scatters and the total field $\phi_1$ can be expressed as the sum of the incident $\phi_i$ and the scattered field $\phi_{sc}$ as shown in Figure 1.9a, where $\phi$ is the velocity potential, so $\boldsymbol{v_1} = \boldsymbol{\nabla}\phi_1$. The scattered field can be represented by a multipole expansion and in the far field this can be approximated by the first two terms (the mono- and dipole components), so $\phi_{sc} \approx \phi_{mp} + \phi_{dp}$ (Figure 1.9a). In short, by finding an expression for the scattered field, the acoustic radiation force $\boldsymbol{F}_{PRF}$ can be calculated, being the gradient of acoustic potential $U_{PRF}$:

$$\boldsymbol{F}_{PRF} = -\boldsymbol{\nabla} U_{PRF} \tag{1.2a}$$

$$U_{PRF} = \frac{4\pi}{3}a^3\left[f_1\frac{1}{2}\kappa_0\langle p_{in}^2\rangle - f_2\frac{3}{4}\rho_0\langle v_{in}^2\rangle\right] \tag{1.2b}$$

$$f_1(\tilde{\kappa}) = 1 - \tilde{\kappa}, \text{ with } \tilde{\kappa} = \frac{\kappa_p}{\kappa_0}, \tag{1.2c}$$

$$f_2(\tilde{\rho}) = \frac{2(\tilde{\rho}-1)}{2\tilde{\rho}+1}, \text{ with } \tilde{\rho} = \frac{\rho_p}{\rho_0}, \tag{1.2d}$$

where $p_{in}$ and $v_{in}$ are the pressure and velocity of the incident wave and $\kappa$ and $\rho$ the compressibility and density of the particle and the bulk fluid (subscripts p and 0), respectively.

When a standing wave field is created, the ARF can be calculated by substituting a sinusoidal pressure and velocity into Equation (1.2b). For a one-dimensional field in $z$-direction and after differentiation this gives:

$$\boldsymbol{F}_{PRF} = 4\pi\Phi(\tilde{\kappa},\tilde{\rho})ka^3E_{ac}\sin(2kz) \tag{1.3a}$$

$$E_{ac} = \frac{p_a^2}{4\rho_0 c_0^2} \tag{1.3b}$$

$$\Phi(\tilde{\kappa},\tilde{\rho}) = \frac{1}{3}\left[\frac{5\tilde{\rho}-2}{2\tilde{\rho}+1} - \tilde{\kappa}\right] \tag{1.3c}$$

where $\Phi(\tilde{\kappa},\tilde{\rho})$ is the acoustophoretic contrast factor, $E_{ac}$ the acoustic energy density, $k = 2\pi/\lambda$ the wave number and $p_a$ the pressure amplitude. Depending on the contrast factor, particles can be trapped in pressure nodes or anti-nodes as shown in Figure 1.9b or right in between [72].

For the derivation of the ARF, the fluid was assumed to be inviscous. Corrections have to be made for particles with a size comparable to the viscous boundary layer and when the density of the particle is very different from water.

**Secondary radiation force** An additional force arises when there are more particles present in the fluid. After the incident field reaches a particle, the scattered sound field will in turn influence other particles it encounters. The force associated with this interaction is called the secondary radiation force (SRF), also known as the Bjerknes or interaction force. It arises from the product of the scattered pressure and velocity fields of one particle with the scattered fields of another [73]. For wavelengths much larger than the particles and the distance $d$ between their centers ($a, d \ll \lambda$), the SRF can be expressed as [64]:

$$\boldsymbol{F}_{\mathrm{SRF}} = 4\pi a^6 \left( \frac{(\rho_\mathrm{p} - \rho_0)^2 (3\cos^2\theta - 1)}{6\rho_0 d^4} v^2(x) - \frac{\omega^2 \rho_0 (\kappa_\mathrm{p} - \kappa_0)^2}{9d^2} p^2(x) \right) \tag{1.4}$$

where $\omega$ is the angular frequency, $v(x)$ and $p(x)$ the velocity and the pressure in the position $x$ of the particle, and $\theta$ the angle between the centerline connecting the particles and the propagation direction. The SRF is by convention positive for a repulsive force and only becomes important when particles are close to each other. For particles that gather at pressure nodes and that are less dense than the fluid, the SRF causes clusters to form, as shown in Figure 1.10.

One caveat is that the expression above only relates to centre-to-centre forces. The interaction force can also have a component in the tangential direction, resulting in coupled rotational motions. Moreover, for non-identical objects, the interaction force on each object is non-reciprocal and differs both in magnitude and direction. Due to this complexity of interaction the agglomeration process is not simply a matter of attraction or repulsion, typically associated with electrostatic interaction. It becomes increasingly harder to predict the behaviour with more particles [73].

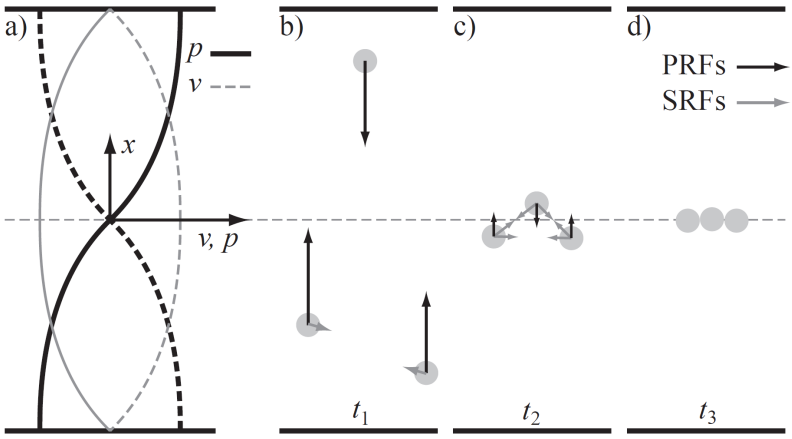


**Figure 1.10:** Schematic from Manneberg [64] showing the pressure field for a half wave (a). In (b-d) the predicted movement of the particles over time can be seen, resulting in a cluster in the pressure node.

**Acoustic impedance** A quantity that is often encountered in acoustofluidic devices is the acoustic impedance. When a pressure wave hits a surface, the acoustic impedance dictates how much the induced motion is impeded (Rienstra). In resonator devices, the reflection at the fluid chamber walls should be high in order to retain sufficient acoustic pressure. This is determined by the acoustic impedance which depends on the material properties. For a planar acoustic wave that moves from one material into another (denoted with 1 and 2, respectively) with normal incidence, the following expressions for the reflection and transmission can be derived:

$$R = \frac{Z_2 - Z_1}{Z_2 + Z_1} \tag{1.5a}$$

$$T = 1 - R \tag{1.5b}$$

where $Z_i = \rho_i c_i$ is the acoustic impedance, in which $\rho_i$ and $c_i$ respectively denote the density and speed of sound of material $i$. These equations follow from the continuity requirement of the pressure and the normal component of the fluid velocity.

It can be observed that a large difference between the acoustic impedance of the materials gives a large reflection. Materials like silicon and glass are therefore suitable whereas polymers give lower reflection and

also have a higher attenuation. On the other hand, in absolute sense, the impedance difference between water and glass or silicon is still not large. As a result, motion in the whole system is induced and the fluid resonances are influenced by all the components [74]. It has been shown that polymer devices were also capable of acoustophoresis by employing whole-system resonances. There, rather than depending on high acoustic contrast between the fluid chamber and the solid walls, the surrounding air provided a sufficient boundary [75].

**Acoustic streaming** The absorption of an acoustic wave which gives rise to a steady fluid flow is known as acoustic streaming. From the acoustic wave, oscillations in velocity and pressure arise which cause the particles to vibrate. In a fluid without losses, this movement would be zero on average. When there are losses, as is the case in real fluids, the viscous attenuation causes particles to slightly shift position each cycle. Over time these collective non-zero net displacements give rise to streaming flows. There are two common ways by which this occurs, called Eckart streaming, or 'quartz wind', and boundary-layer-driven streaming. Eckart streamings is driven by the attenuation of acoustic waves in the bulk of the fluid, which on average results in a net force in the direction of wave propagation, schematically shown in Figure 1.11a. The second type occurs due to the friction between the acoustically excited fluid and a solid boundary. Outside the viscous boundary (or Stokes) layer, the fluid can oscillate irrotationally but inside it starts recirculating due to the no-slip condition of the wall. This inner streaming then drives the flow pattern in the bulk. This is called inner boundary layer streaming, or 'Schlichting streaming'. Consequently, also a steady flow in the bulk of the fluid is created [76], which is known as outer boundary layer streaming or 'Rayleigh streaming'. Figure 1.11b shows these inner and outer flow fields.

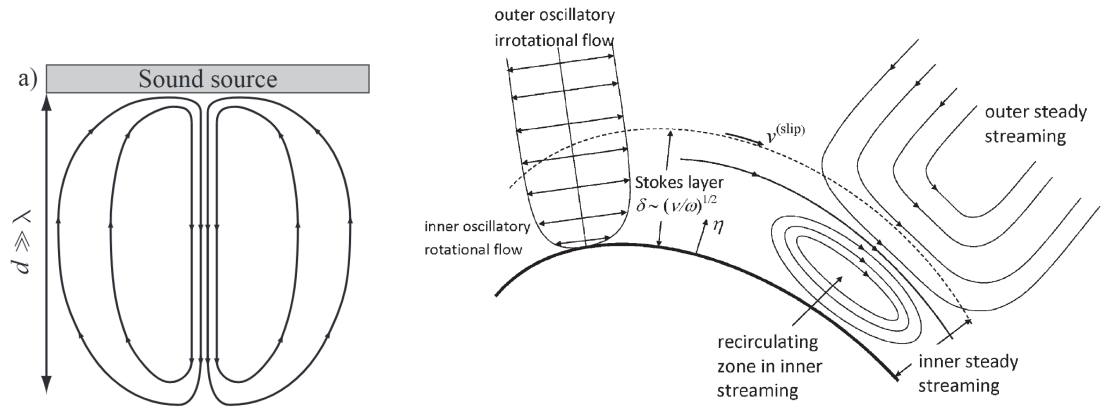


**Figure 1.11:** Schematics showing two types of streaming. (a) A typical profile of Eckart streaming which is driven by the absorption of acoustic energy in the bulk fluid, from Manneberg [64]. (b) Illustration of boundary layer streaming from Sadhal [76]. The black line is the solid boundary and the dashed line indicates the boundary of the Stokes layer.

Streaming influences the particles through the drag force. As Reynolds numbers are typically small in microfluidics, the Stokes' expression for the drag force can be used for a spherical particle [77]:

$$\mathbf{F}_\mathrm{d} = -6\pi\eta a(\mathbf{v} - \mathbf{v}_\mathrm{p}) \tag{1.6}$$

in which $\eta$ is the dynamic viscosity, $a$ is the particle's radius, and $\mathbf{v}$ and $\mathbf{v}_\mathrm{p}$ the velocity of the fluid and the particle, respectively. This streaming force approximately grows with decreasing particle size and starts to dominate over the radiation force for particles with a radius smaller than 1 µm. The use of larger particles is beneficial as streaming is less understood and less controlled [56].

**Piezoelectric transducers** The generation of sound waves relies on the piezoelectric effect, where an electrical voltage causes mechanical motion and vice-versa. The piezoelectric effect arises due to an asymmetry in the crystal structure. By imposing a mechanical stress, the lattice deforms and subsequently a net electric dipole moment is formed, as shown in Figure 1.12a for a quartz crystal. By alternating the voltage using a signal generator, periodic expansion and contraction can be obtained. For a bulk acoustic piezoelectric

transducer, thickness and shear modes can be excited (Figure 1.12b), depending on the structure material and the relative orientation of the electrodes: expansion and contraction occurs when the electric field is aligned with the direction of polarization and shear arises when these are oriented orthogonally.

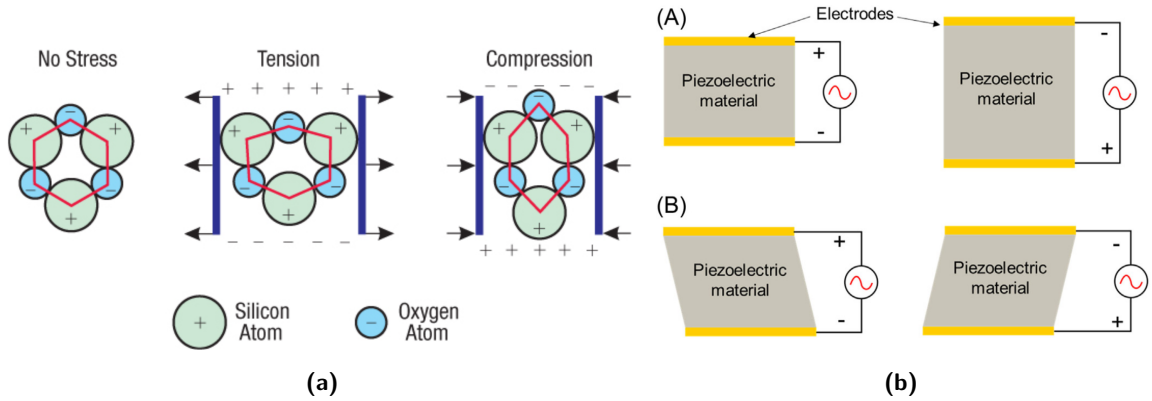


**Figure 1.12:** (a) Simplified depiction of a quartz lattice from Gupta et al. [78]. The deformation of the lattice deforms under a mechanical load results in a net electric dipole moment. (b) Illustration from Ozcelik et al. [35] showing how both thickness (A) and shear (B) modes can be excited.

The constitutive equations when linear piezoelectric theory and a linear elastic relation is assumed are:

$$\gamma = s\sigma + dE \tag{1.7a}$$

$$D = d\sigma + \varepsilon E \tag{1.7b}$$

Table 1.2 below gives an explanation of the symbols. All the symbols are tensors and the symbol convention by Dual and Möller [79] is followed.

**Table 1.2:** Summary of symbols for piezoelectric constitutive equations, adapted from Dual and Möller [79].

| Symbol | Name | Unit |
|---|---|---|
| $\gamma$ | Mechanical strain | - |
| $D$ | Electric displacement | $\mathrm{C\,m^{-2}}$ |
| $\sigma$ | Mechanical stress | $\mathrm{N\,m^{-2}}$ |
| $E$ | Electric field | $\mathrm{N\,C^{-1}}$ |
| **Material properties** | | |
| $s$ | Mechanical compliance | $\mathrm{m^2\,N^{-1}}$ |
| $d$ | Piezoelectric charge constant | $\mathrm{C\,N^{-1}}$ |
| $\varepsilon$ | Permittivity at constant mechanical stress | $\mathrm{C^2\,m^{-2}\,N^{-1}}$ |

Although many materials show some piezoelectric response, in acoustofluidic applications ceramics like lead zirconate titanate (PZT) are often used due to their high piezoelectric material constants [79]. For a strong response, the transducer should be driven at its resonance, which is decided by its dimensions. Transducers with narrow resonance peaks (high $Q$-factors) are best suited for this. When a more flexible, broadband excitation is desired, the $Q$-factor can be adjusted, for example by adding damping with a backing layer.

### Device configurations

To obtain a potential field in a BAW device multiple strategies exist, for instance by applying an array of transducers or a hologram [34]. Regarding standing BAW devices, it is common that the transducers or pairs of transducers are implemented such that each transducer (pair) excites a mode in one dimension. The design layouts can broadly be grouped in two types: parallel and non-parallel actuation. This refers to the direction

of the piezo actuation with respect to the intended direction of the standing wave field. The transducers can either be oriented such that the excitation direction aligns with the standing wave field (parallel), or it could be in a different direction (non-parallel). For convenience these two configurations will be referred to as parallel and non-parallel, respectively. This similar to so-called layered and transversal resonators in one-dimensional setups, shown in Figure 1.13. It should however be noted that transversal resonators are a special case of a non-parallel layout where the directions are perpendicular.

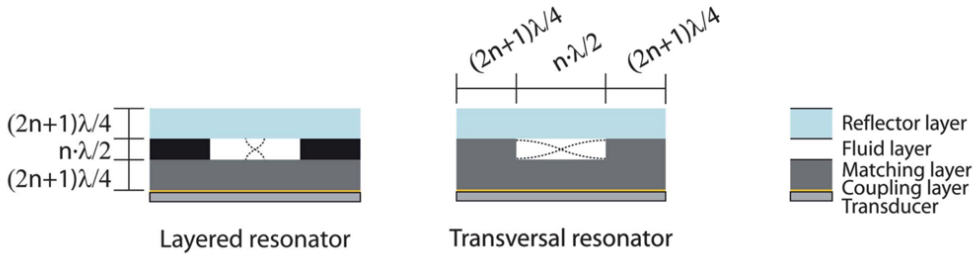


**Figure 1.13:** Two types of resonators where the standing wave and the direction of excitation is either parallel or non-parallel for layered and transversal resonators, respectively. The schematic is adapted from Lenshof et al. [80].

For parallel layouts, the standing wave arises from the reflections between the transducer and a reflector layer. Additionally, a pair of opposing transducers can also generate a standing wave. In that case no resonance conditions are required. A benefit of this is that the force field is less sensitive to temperature changes [66]. Parallel layouts require careful tuning of the thicknesses of the different layers to attain a high Q-value for the system.

For a non-parallel layout, the standing wave field is created by reflections between the channel walls. An example is shown in Figure 1.14c where the transducers are mounted on wedges. The choice of layer thicknesses is not as delicate because it is the system resonance that is important. Another method is to excite the chamber in multiple directions using a single piezoelectric transducer, as is shown by Oberti et al. [81]. The electrode can divided into multiple segments as shown in Figure 1.14a such that the different parts can be activated separately, which excite different modes in the piezo plate (Figure 1.14b). A benefit is that this makes it easier to miniaturize the device further.

Overall, for setups that rely on resonances, the location of the piezo and the way it is excited strongly influences the strength of the pressure field. Qiu et al. [82] showed that placing the piezo on the side of the chip can increase the acoustic energy density by a factor of four. Next to that, Tahmasebipour et al. [83] demonstrated that the position of the piezo with respect to the chip and the chamber strongly influences the acoustic radiation force.

### Materials

**Microfluidic chip** In the design of acoustic resonators the material choice is important as it, for a large part, determines the strength of the field in the fluidic chamber. For non-parallel layouts, materials with high acoustic impedance such as glass, silicon or metal are generally recommended to maximize the reflections between the channel walls. In addition, materials with low acoustic losses are better to minimize power consumption and heat loss [80]. Glass is often chosen owing to its transparency, which is needed for visualizing the sample, and its low damping. It is important to mention that the material choice depends on which resonance is excited, the one in the fluid or of the whole system. Moiseyenko and Bruus [75] showed that, in spite of their higher damping, softer materials like PMMA could also be used when the whole system is excited. The quality of the acoustophoresis was similar to the conventional system with hard materials.

The use of a parallel layout allows for a wider choice of materials. Also polymers could for example be used, both as an adhesive to bond the layers together, as well as for the bulk of the chip. The idea is that losses in these layers are acceptable as long as it enhances the energy density in the fluid chamber. Some examples are Owens et al. [85] and Hou et al. [86] that both use an acrylic frame.

**Piezoelectric transducer** For piezoelectric transducers there are two types of material that are often used: ceramics and single crystals. Ceramics have a polycrystalline structure and are attractive for their high cou-

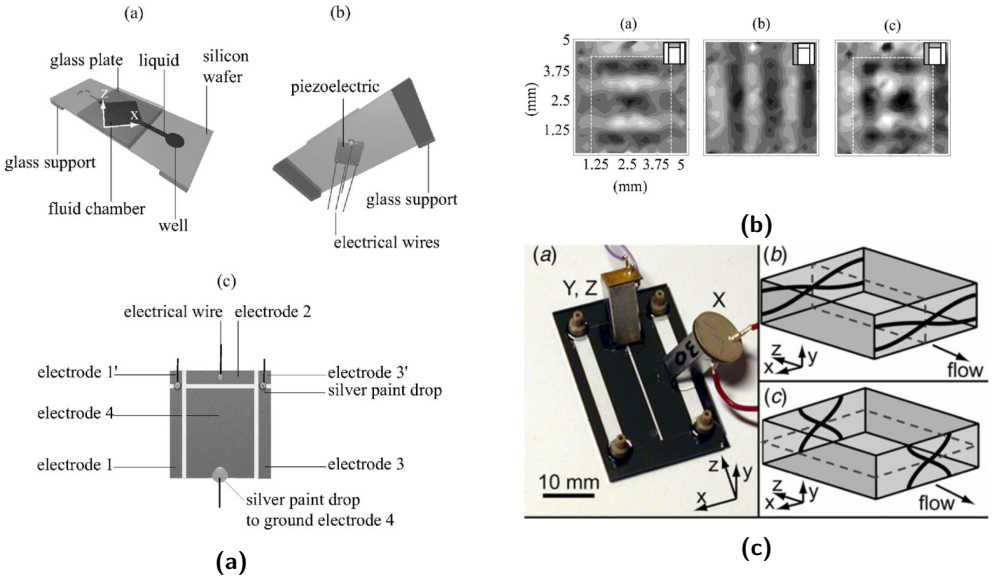


**Figure 1.14:** (a) Setup where a single piezo plate with sectioned electrodes is used to create a 2D potential field, from Oberti et al. [81]. (b) Picture from Oberti et al. [81] showing the displacement field of the piezo plate when different strips of the piezo are excited. (c) Setup from Manneberg et al. [84] that uses transducers mounted on wedges. Each transducer excites one of the two modes.

pling and low dielectric loss. Single crystals on the other hand has a continuous crystal lattice. As a result, their characteristics strongly depend on the direction in which it is cut.

Lead zirconate titanate (PZT) transducers are a widely used group of ceramics in BAW devices [8, 84–87]. They have a high piezoelectric coefficient ($d_{33} \sim 600\,\mathrm{pC\,N^{-1}}$) and electromechanical coupling coefficient ($k_t \sim 0.5$), which means they can efficiently convert electrical energy into acoustic energy. In addition, they generate relatively little heat owing to their low dielectric and mechanical losses. PZT piezoelectric material exist in so-called 'soft' and 'hard' variants. Softer piezoelectric materials are easier to polarize and generate higher pressures [88]. Hard materials have a high stability and can endure high electrical and mechanical stress. They have lower dielectric losses which gives less heat production compared to soft materials.

Common single crystal piezoelectric materials include quartz and lithium niobate ($LiNbO_3$). They are better suited for high-frequency ($10\,\mathrm{MHz} - 10\,\mathrm{GHz}$) applications compared to ceramics [34, 89]. These are more often used in SAW devices because of their large electromechanical coupling.

There are many piezoelectric materials and each of them has its strengths and weaknesses. From the BAW literature it is clear that both PZT and lithium niobate both are suitable candidates. Sitters et al. [8] showed that lithium niobate achieved higher forces. In addition, PZT is toxic due to its lead content.

## 1.3 Acoustic Force Spectroscopy (AFS)

Acoustic force spectroscopy (AFS) aims to obtain information on the forces acting on a sample using acoustics. The acoustic radiation force is utilized to control the position of the objects and create tension on the sample. To estimate the exerted forces, optical measurements are done using a microscope, which thus requires using a transparent wall for at least one side of the fluidic chamber. Larger samples like cells can be directly manipulated while for smaller samples like molecules, microbeads are used.

Sitters et al. [8] were able to perform force measurements on individual molecules of double-stranded DNA (dsDNA). They created a one-dimensional force field in the fluid chamber using a thin piezo plate made of PZ26. The DNA was at one end attached to the glass wall and at the other to a 4.5 µm polystyrene microsphere. Their setup is shown in Figure 1.15a. Forces up to 120 pN were achieved, which would be strong enough to overstretch DNA or unfold proteins, shown in Figure 1.15b. In addition to quantifying the tension in dsDNA, the effect of binding RecA proteins on the DNA and the rupture-force distribution of antigen-antibody bonds was shown.

In a later paper the setup and design method was improved [90]. To allow for bright-field microscopy, a transparent lithium niobate piezo crystal was used, enhancing the tracking accuracy. Furthermore a tool to

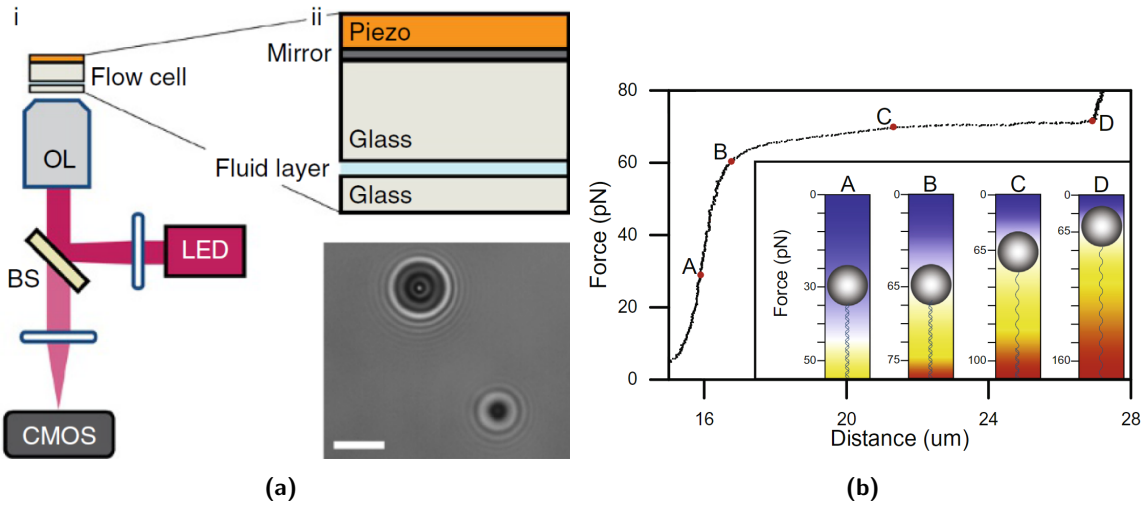


**Figure 1.15:** Setup used by Sitters et al. [8] showing layered resonator and the imaging system. Also an image of a 4.5 µm polystyrene and a 1.5 µm silica microbeads can be seen, scale bar 5 µm. (b) A force curve from Kamsma et al. [90] showing the profile of overstretching lambda DNA strand. For each section the force profile in the fluid chamber is depicted.

optimize the layer thicknesses, and an experimental force validation method were developed. Forces up to 350 pN on a 4.5 µm were reached using this optimization. Next to a force-clamp mode, where the force is kept constant, Figure 1.15b shows the use of a distance clamp. In that case the position of the beads can be controlled thanks to a strong force gradient, which is better for investigating multiple rupture events on the same sample.

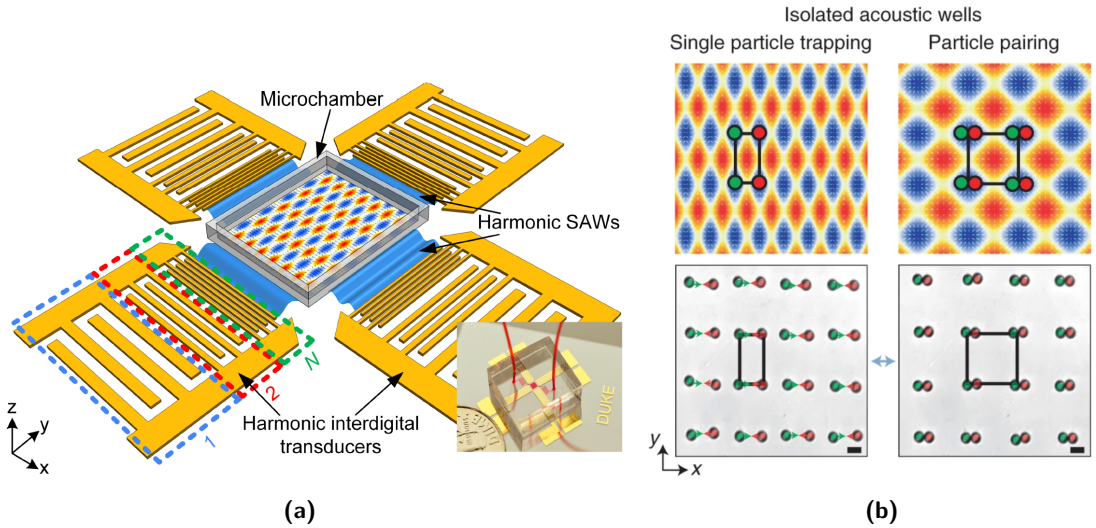


**Figure 1.16:** Figures from Yang et al. [39]. (a) Illustration of the setup comprising two pairs of chirped IDTs. (b) Simulations (top) and images (bottom) that show the dynamic force field, allowing for repeatable pairing of 9.51 µm polystyrene microbeads, scale bar 10 µm.

More recently, Yang et al. [39] designed a microfluidic platform capable of performing AFS using standing SAW. Two orthogonal pairs of IDTs created a force field in which a grid-like pattern of particles could be formed (Figure 1.16a). This allowed for more control over individual particles in comparison to the one-dimensional force fields in the BAW setups discussed above. Next to trapping particles, they were able to reconfigure the lattice of acoustic wells, thereby changing their positions. This was achieved with a method called time-effective Fourier synthesis. This time-divided multifrequency method will be discussed further in Section 2.2.2. The assembly and reversible formation of colloidal crystals was shown together with rotational

control over the formations. Furthermore, the distance between single colloids in a grid could be controlled, enabling reversible pairing and separation for more than 100 pairs simultaneously, shown in Figure 1.16b. Finally, they applied this manipulation to individual cells and were able to quantify the cell-to-cell adhesion and its lifetimes with a similar throughput.

### 1.3.1 Force measurement methods

To estimate the force on the trapped particle, several methods are used. Below, the most widely applied approaches are summarized.

**Equipartition method** As an acoustic trap can be considered to be a harmonic potential well, the trapped particle behaves as a harmonic oscillator around an equilibrium. In thermal equilibrium, the equipartition theorem then states that each degree of freedom contributes $\frac{1}{2}k_BT$ to the average energy. This can be used to relate the the mean squared displacement $\langle x^2 \rangle$ to the trap stiffness $k$ through the thermal energy according to:

$$\frac{1}{2}k\langle x^2 \rangle = \frac{1}{2}k_BT \tag{1.8}$$

where $k_B$ is the Boltzmann constant and $T$ the absolute temperature. The position data could be acquired using for example a centroid tracking algorithm. It is important that the position detection is sufficiently fast as the stiffness will otherwise be overestimated. A benefit of this method is that the viscous drag coefficient does not have to be known [91].

**Power spectrum method** In the second method a power spectrum of the displacement is used, which can be obtained by Fourier transforming the position data. This can again be obtained using a tracking algorithm on the image data. Then a Lorentzian is fitted to the power spectrum:

$$S_{\mathrm{xx}}(f) = \frac{D/(2\pi^2)}{f_c^2 + f^2} = \frac{k_BT}{2\gamma\pi^2(f_\mathrm{c}^2 + f^2)} \tag{1.9}$$

where $f$ is the frequency, $f_\mathrm{c}$ the corner frequency ($f_\mathrm{c} = k/(2\pi\gamma)$), and $\gamma$ the effective viscous drag coefficient. For the microsphere's diffusion coefficient $D$, Stokes-Einsteins's relation has been used ($D = k_\mathrm{B}T/\gamma$) [92]. This fit results in a corner frequency $f_\mathrm{c}$ that directly relates to the trap stiffness. Unlike the equipartition method, this method requires the viscous drag coefficient to be known [91]. For spherical particles with a known diameter the drag coefficient is available though a correction should be made when the particle is near a chamber wall. Then the Stokes drag force grows due to the additional hydrodynamic interaction from the surface. A correction using Faxén's law can be made to calculate the effective drag coefficient [8, 39].

**Kinetics method** When a particle accelerates over a certain distance, for example when it separates from another particle as in the cell-adhesion experiments done by Yang et al. [39], analysing the kinetics can provide a force estimation. Newton's second equation is used for this, relating the net force acting on the particle to its motion. For an analysis in the horizontal plane, only the acoustic radiation force $\mathbf{F}_\mathrm{r}$ and the drag force $\mathbf{F}_\mathrm{d}$ have to be considered:

$$m\mathbf{a} = \rho\frac{4\pi(d/2)^3}{3}\mathbf{a} = \mathbf{F}_\mathrm{r} + \mathbf{F}_\mathrm{d} \tag{1.10}$$

where $m$, $\mathbf{a}$ and $d$ are the particle's mass, acceleration and diameter, respectively. As shown, the mass can be calculated from its known density $\rho$ and diameter $d$. After the velocity ($\mathbf{v}$) data has been gathered from particle position tracking, the acoustic radiation force can be determined:

$$\mathbf{F}_\mathrm{r} = \rho\frac{4\pi(d/2)^3}{3}\frac{d\mathbf{v}}{dt} + 6\pi\gamma(d/2)\mathbf{v} \tag{1.11}$$

# Chapter 2

# Research Proposal

Having discussed the working principle of bulk acoustics and the application of acoustics in force spectroscopy, this chapter will give an overview of the knowledge gap and the research questions.

## 2.1 Problem statement

The method of performing AFS on the BAW platforms by Sitters and Kamsma et al. [8, 90] explained above has proven to be effective but there are some difficulties and limitations. Firstly, as there is only control over the force in one direction, the DNA has to be attached to the surface on one side. This tethering involves cleaning the surface in several steps, followed by cycles of flushing and incubating. Even though most of the time consists of waiting, the preparation takes at least 1.5 h [93]. In addition, Sitters et al. showed that for one of their experiments, the fraction of correctly tethered microspheres was only 8%. All other particles were identified as either surface-attached or doubly tethered and could not be used [8]. This gives an indication that working close to the surface and having little control over the particles can still give problems regarding throughput. Secondly, in their experiment the microbeads were viewed in the same direction as the applied force, which largely blocks the visibility of the sample. When probing DNA mechanics or DNA metabolic reactions like transcription and replication, visualization is valuable as it uncovers the diverse protein-DNA interactions and their movement. One method that achieves this is the so-called DNA curtain, a DNA flow-stretch assay where hundreds of DNA strands are aligned and stretched using buffer flow [94, 95]. With this technique, real time imaging reveals the diverse protein-DNA interactions.

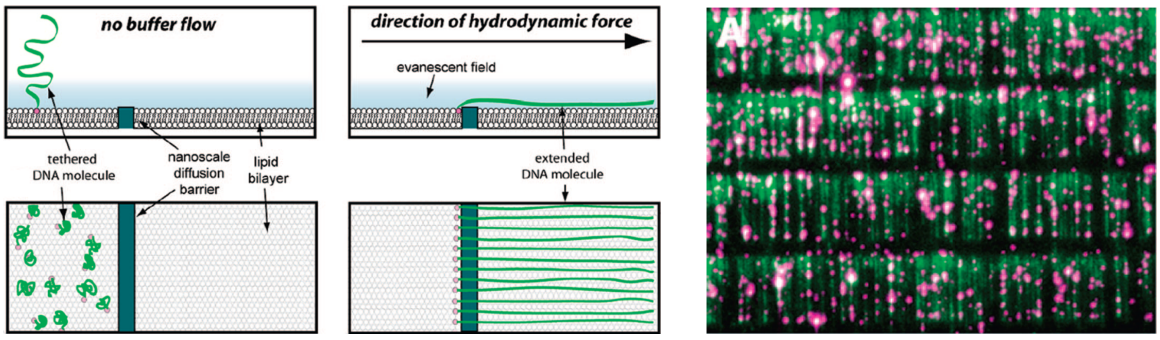


**Figure 2.1:** **(a)** Schematic from Fazio et al. [95], showing how the DNA is stretched across a lipid bilayer using a buffer flow. **(b)** Image revealing fluorescently tagged proteins (magenta) bound to the DNA (green) in the curtain, revealing their binding position distribution, from [95].

The acoustic array configuration used by Yang et al. could be used to overcome these limitations. The DNA could for example be connected to two beads on both ends. By then changing the distance between the particles as in Figure 1.16b, force measurements could be done on the DNA itself or on other samples by using the DNA as so-called linkers or handles. The difference between the intended configuration and the one used by Sitters et al. [8] is shown in Figure 2.2a. This configuration also has the potential for multiplexed

experimentation (Figure 2.2b).

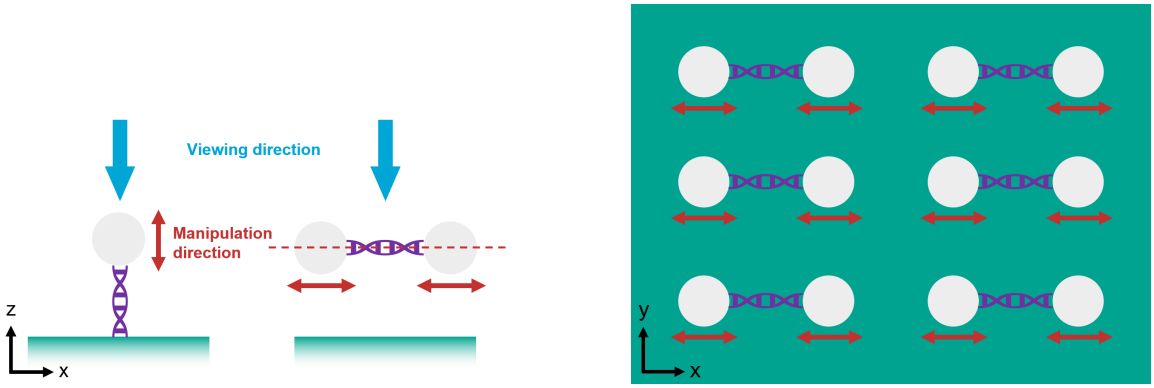


(a) (b)

**Figure 2.2:** (a) Schematic showing the difference between the configuration used in the setup of Sitters and Kamsma et al. [8, 90] (left) and the proposed layout for this research project (right), which is similar to the bead configuration of Yang et al. [39]. (b) Layout of the grid that shows how the intended configuration allows for doing parallel experiments.

It would be attractive to implement a similar method in a BAW platform. As discussed earlier, BAW devices are generally cheaper than SAW devices as the fabrication is less intensive. This approach has several potential advantages. It would first of all shorten the preparation as the time-consuming steps of surface treatment can be left out. Additionally, it might increase the throughput as the fraction of usable beads is probably larger. Presumably, when the beads can be arranged in a grid owing to the greater control of their positions, they are less likely to connect incorrectly. At the same time, there is no need to bring them close to a surface, thereby again lowering the risk of faulty attachments. The final benefit is that the sample could be visualized, extending its functionality and opening up the use in studies like those performed with DNA curtains.

## 2.2 Knowledge gap

Performing AFS with the ability to visualize for example the DNA, entails several requirements for the design setup. Below three aspects and their gaps in relation to the design goal are discussed.

### 2.2.1 Bead isolation

The problem with most BAW patterning setups is that particles cluster together in the potential wells, which obstruct force measurements. As the additional forces between the clustered particles are unknown, they prevent quantifying the force of interest: the one acting on the sample. The first reason agglomeration occurs is that the secondary radiation force causes an attraction between the particles. Another reason relates to the size of the particles compared to the wavelength. The review by Liu et al. [96] shows that most of the BAW patterning setups employ frequencies of only a few MHz, corresponding to wavelengths of a few hundred microns. Since the particles are typically much smaller than that, this means that multiple particles fit in one potential well, as shown in Figure 2.3. A low initial sample concentration would help prevent this though at the cost of a low occupation of the wells.

Over the last decade, the problem of achieving isolated, or so-called one-cell per well (OCPW), patterning has gained increased attention. In a notable paper by Collins et al. [71] it was empirically shown that isolated trapping can be attained within a relatively narrow range of diameter-to-wavelength ratio's ($\xi = d/\lambda$). For polystyrene particles this range was $3.2 \geq \lambda/d \geq 3.6$ . Their results are plotted in Figure 2.4a.

This result was further studied by Habibi et al. [97] with an investigation of the acoustic forces. In a one-dimensional model they found that the PRF not only depends on material and size properties of the particle but also on the particle's resonances, as it is an elastic sphere. These resonances depend on its Young's modulus and Poisson ratio and show up as peaks in the force curve in Figure 2.4c. Furthermore, several regimes of forces were identified that caused trapping in either the node or the anti-node. These regions depend on the

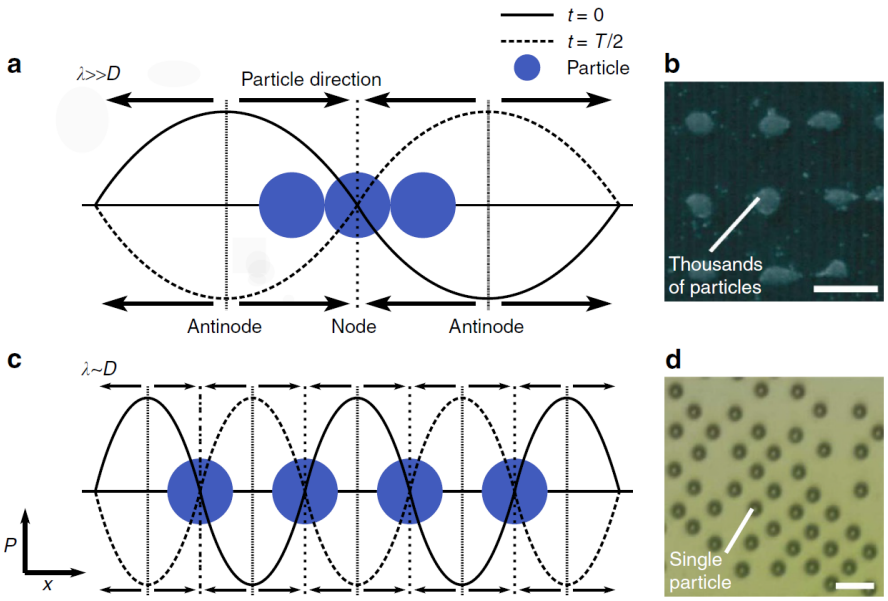


**Figure 2.3:** Illustration from Collins et al. [71] showing that the size of the particle with respect to the wavelength is important for isolated patterning, scale bar 300 µm.

eigenfrequencies of the particle. The SRF also shows an additional dependence on size due to the particle resonances. Figure 2.4b shows how the attractive force between two particles in a one-dimensional model has a strong peak and later switches sign, becoming repulsive. Later, Silva et al. [72] created a theoretical model to predict particle patterns and found that particles can also be trapped in midpoints, right in between two nodes. In addition, they achieved OCPW patterning with larger so-called Mie particles ($\xi = 0.32$), though not consistently and only in a 2D force field so the particles sedimented on the bottom of the chamber. Their results are shown in Figure 2.5. Recently, Yang et al. were able to trap individual colloids and cells in a 2D grid with a reconfigurable lattice constant.

Until now, all consistent OCPW patterning has been achieved with SAW platforms. As there is no reason to assume this is not possible in BAW devices, it is worth further investigating its adoption there. This would open up the way for more functional AFS. Furthermore, it could be used in tissue engineering, which is especially attractive for BAW devices as larger volumes can be handled [72].

### 2.2.2 Dynamic acoustic fields

To perform the force measurements, dynamic control over the acoustic field is needed. After the beads have been isolated in the potential wells, the next step is to apply equal but opposite forces on pairs of particles. This means the acoustic field has to be adjusted in such a way that there is a relative change in distance between the potential wells. Until now the majority of in-plane dynamic manipulators are achieved using SAW devices [66].

Existing methods of dynamic manipulation for BAW devices can be subdivided based on the type of operation: resonant and non-resonant. Resonance based devices are limited to the resonance frequencies of the fluid chamber or the whole device, whereas non-resonant operation is not always constrained in its operating frequencies. For in-plane manipulators, where the transducers are situated around a plane, the type of control could be labelled as simultaneous multifrequency excitation (ME) or time-divided ME. The distinction lies in the actuation of multiple frequencies at the same time or in succession, respectively. These labels are relevant for both resonant and non-resonant devices. In addition, for non-resonant devices, phase modulation can be applied. An overview of BAW with dynamic fields is given in Table 2.1.

Simultaneous multifrequency excitation works by sending a signal containing multiple frequencies to the actuator. The force field results from the superposition of the contribution of each mode and is determined by their amplitude and phase [100]. This has been used in SAW platforms [105] but is harder to achieve using BAW due to the difference in electrical impedance of the transducer at different frequencies. It could however enable to shape the force field to achieve higher trap stiffnesses [106].

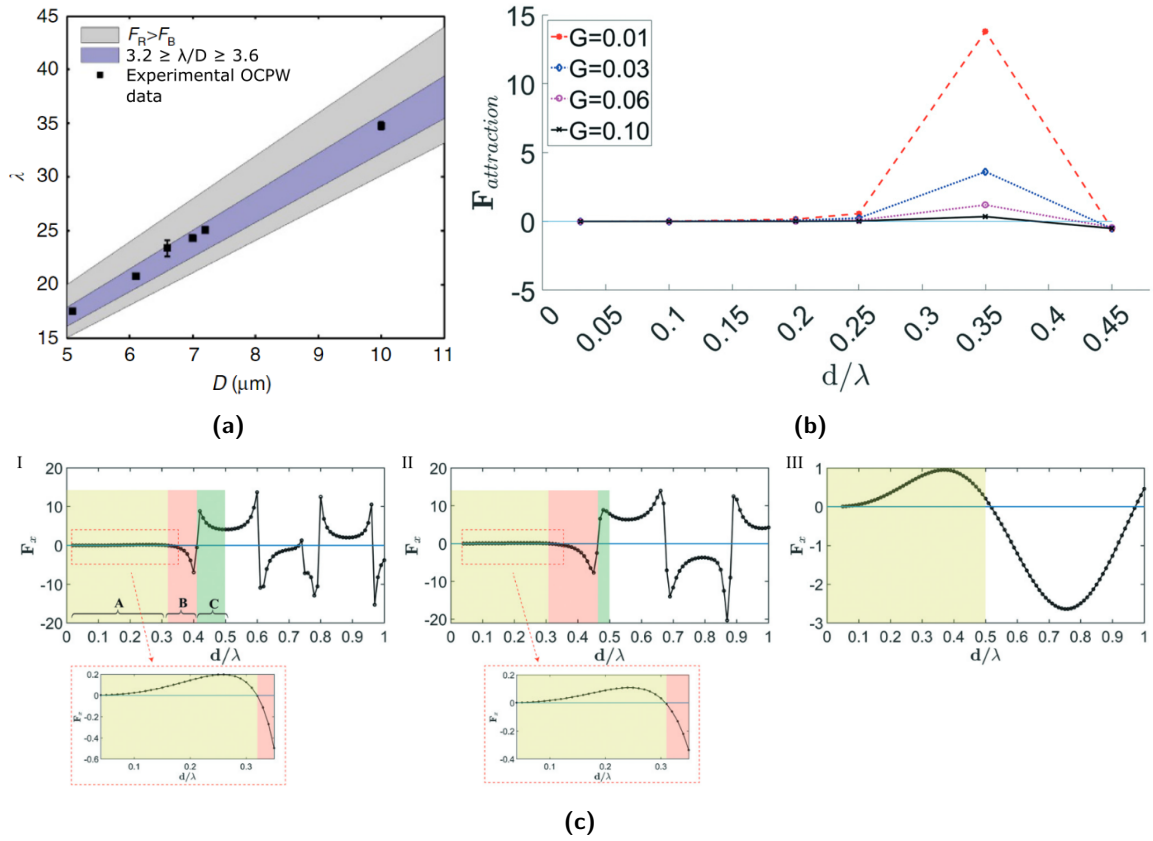


**Figure 2.4:** **(a)** Graph from Collins et al. [71] showing the experimentally tested bead sizes which resulted in an isolated trapping pattern. **(b)** Secondary radiation force plot from Habibi et al. [97] for different gap sizes $G$. **(c)** Profiles of the ARF versus normalized size for spherical PMMA (I), polystyrene (II) and silica (III) particles. The regions A and C corresponds to a positive ARF, pushing the particles to the pressure node, and in region B the particle is pushed to the pressure anti-node. Taken from Habibi et al. [97].

Time-divided multifrequency excitation on the other hand relies on rapidly pulsing or switching between frequencies. Smooth manipulation can be obtained when the response time of the particle is relatively large compared to the time the piezo is actuated. The resulting force field is then a time weighted sum of constituent standing wave fields. Glynne-Jones et al. [98] achieved a continuous shift of the nodal position by switching between the half- and quarter-wave mode (Figure 2.6b). Cox et al. [107] identified several impulse regimes of this method and showed that localized manipulation was possible. This could be used to not only pattern particles but also clear away undesired particles. The technique has shown to be useful in both particle separation, shown in Figure 2.6a, and transportation [104].

What is still missing is the ability to control the interparticle distance of particles in a 2D grid using BAW. Patterning in a grid is desirable as more particles can be observed at the same time compared to a trapping pattern in only one dimension. Moving particles relative to each other has been shown to work for particle separation but those often only make use of a 1D force field [108]. 2D patterning and manipulation is more often done in SAW devices. Slanted-finger [109, 110] or chirped [39, 111] IDTs are then used to generate a range of frequencies, which is needed to change the distance between potential wells. In addition, 2D BAW patterning setups from literature often do not apply a pressure field in the vertical z-direction, which is needed to levitate the beads [72, 81, 85, 86, 103]. In SAW devices the surface waves also generate a pressure gradient in the vertical direction [112, 113] which automatically enables levitating the beads. It is worth investigating the application of a 3D force field in BAW devices to bridge this functional gap.

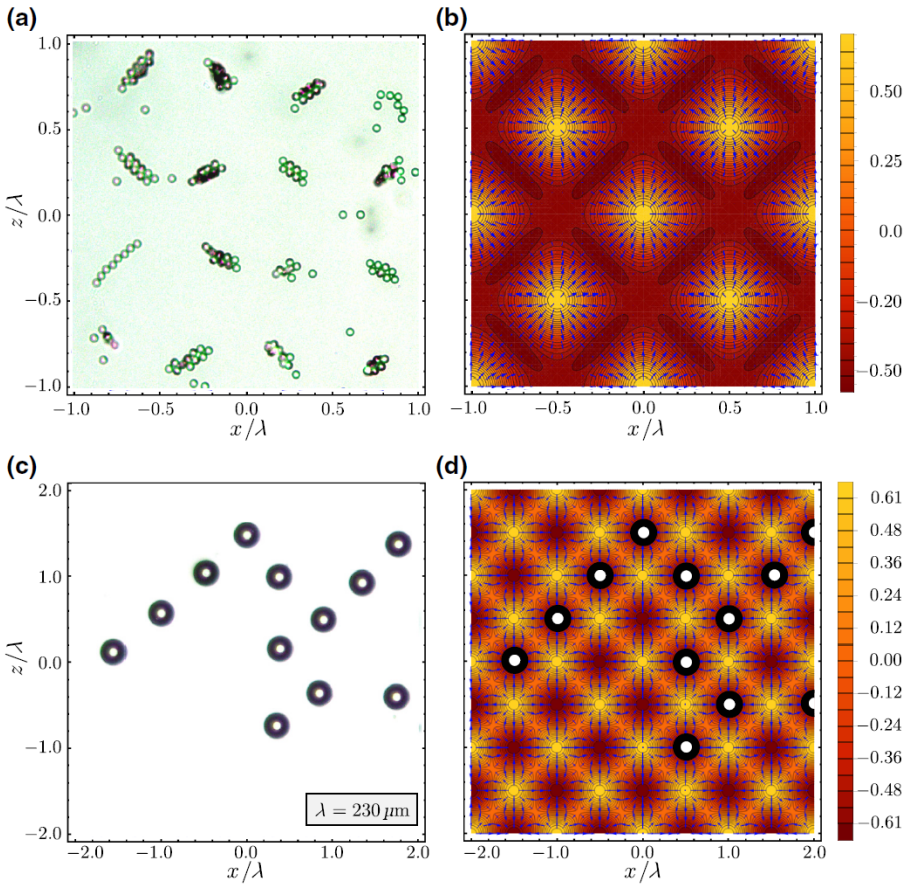


**Figure 2.5:** Images from Silva et al. [72] showing the trapping patterns and the acoustic energy landscape of 10 µm (a,b) and 75 µm (c,d) polystyrene particles. The smaller particles are trapped in midpoints in a diamond shape and the Mie particles reside in the pressure nodes.

**Table 2.1:** Overview of BAW devices capable of producing dynamic acoustic fields. The asterisk (*) denotes that only simulation results were obtained. Abbreviations: PS is polystyrene; PE is polyethylene; ME is multifrequency excitation

| **Authors** | **Control** | **Resonator** | **Operating principle** | **Frequency (in MHz)** | **Particle (⌀, in µm)** |
|---|---|---|---|---|---|
| Skotis et al., 2015 [39] | 1D | No | phase shift | - | PS (6-10) |
| Glynne-Jones et al., 2010 [98] | 1D | Yes | time-divided ME | 1.880-4.396 | PS (10) |
| Shaglwf et al., 2019 [99] | 2D | Yes | time-divided ME | 2.382-2.814 | PS(10) |
| Hou et al., 2022* [100] | 2D | No | simultaneous ME | 0.48-4.933 | - (50) |
| Jeger-Madiot et al., 2022 [43] | 1D | Yes | time-divided ME (frequency sweep) | 1-3 | PS (15) |
| Kandemir et al., 2021 [101] | 1D | No | phase shift (dual-frequency) & time-divided ME (frequency sweep) | 1.8-2.5 | PE (70 & 100) |
| Courtney et al., 2012 [102] | 2D | No | phase-shift | 5 | PS (10) |
| Hou et al., 2020 [86] | 2D | No | phase shift | 2 | PS (30) |
| Owens et al., 2016 [85] | 2D | Yes | time-divided ME | 3.064 | PS (1.5 & 10.8) |
| Tian et al., 2016 [103] | 2D | No | time-divided ME | 4.99-6.78 | micro-droplets (50-100) |
| Manneberg et al., 2009 [104] | 1D | Yes | time-divided ME (frequency sweep) | 6.9 & 2.6 | - |

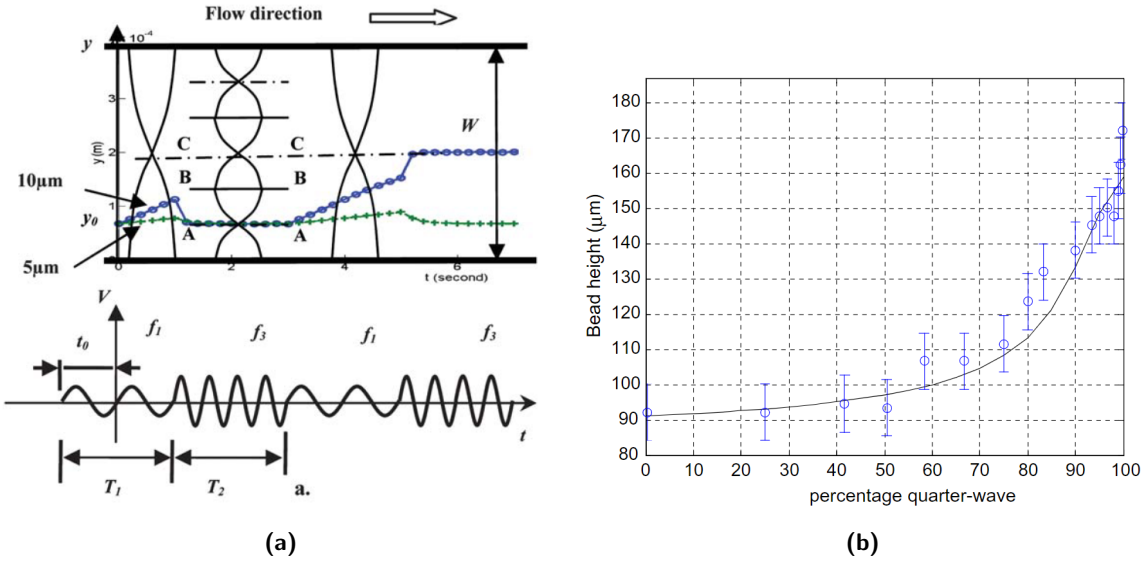


**(a)** **(b)**

**Figure 2.6:** (a) Schematic from Liu et al. [108] that shows how particles can be sorted based on size by switching between frequencies as the larger particle experiences a larger force. (b) Experimental results by Glynne-Jones et al. [98] of particle agglomeration at different heights. This is achieved by changing the ratio of time the quarter- and half-wave mode are activated.

## 2.3 Research questions

The goal of the project was to trap micron-sized beads using ultrasound waves for DNA stretching and protein unfolding experiments. The scope was narrowed down to BAW devices with commercially available piezoelectric transducers. This device should be able to isolate and trap a large amount of particles and at the same time do the experiment in a multiplexed manner for a higher statistical significance of the results in single-molecule analyses. Having given an overview of the existing literature and its current gaps, a research question could be formulated:

> *How can bulk acoustic wave devices be used for performing high-throughput interparticle force experiments?*

This question was divided into two subquestions that could be investigated independently:

1. *How can a bulk acoustic wave device consistently arrange particles in pattern where each potential well holds one particle?*
2. *How can the interparticle distance of the microbeads in the 2D pattern be controlled in a bulk acoustic wave device?*

How the research was conducted is described in Chapter 3. First, the scope is narrowed down further and the requirements on the setup are stated.

## 2.4 Design requirements

The following section discusses the requirements and boundary conditions on the design. It also gives an overview of possible strategies that could be adopted given these restrictions.

**Functional requirements** To map the design space of the setup it was useful to first formulate a set of functional requirements. These indicated what the experimental setup should at least be able to perform.

1. The setup should be able to perform at least 100 identical force-extension DNA experiments in parallel.
2. The setup should be able to visualize both the beads and the DNA using an inverted digital microscope.
3. The trap should be able to apply a force of 110 pN parallel to the imaging plane.

The number of parallel force experiments in the first requirement was chosen based on the performance of the setup of Sitters and Yang et al. [8, 39]. They could perform roughly 150 and more than 100 experiments in parallel, respectively. It should be seen as an approximate lower limit for a proof of concept of scalability below which it would not prove the capability for high-throughput experiments and might not be worth pursuing. The force stated in the third requirement was based on the maximal force on torsionally constrained DNA before it starts yielding [114].

**Boundary conditions** The available means to fabricate and operate the cell were limited. These limitations are captured by the boundary conditions:

1. The trap should use a piezoelectric transducer as the source of forces acting on the beads.
2. The device should not be harmful to the samples.
3. In addition to standard lab tools and equipment it should be possible to fabricate the trap with the means available:
    - Nano-/femtosecond laser cutter
    - Adhesives
    - 3D printing
4. Imaging should be possible with a Nikon Eclipse T*i*2 inverted microscope.

**Functions and strategies** From the functional requirements and the boundary conditions, a list of functions was distilled. An overview of these functions and the corresponding strategies the setup could adopt, can be found in Table 2.2. The focus was on deciding which strategies were best suited for the first three functions. Concerning the other functions, the most simple strategies would initially be applied: the liquid would be trapped in a cavity and inserted through a pipette, and the beads would be imaged directly without the use of for example an optical prism.

**Table 2.2:** Overview of all functions the setup should be able to perform and the possible strategies that could be adopted. For function 4-6 the most simple strategies that will be tried initially are marked bold.

| **Functions** | **Strategies** |
|---|---|
| 1. Fix the position of the levitating beads | Through the acoustic radiation force generated by standing waves<br>• Parallel (layered) resonator<br>• Non-parallel (transversal) resonator |
| 2. Manipulate the position of the beads | Alter the standing wave field:<br>• Time-divided multifrequency excitation<br>• Simultaneous multifrequency excitation<br>• Move transducer and cell w.r.t. each other |
| 3. Prevent interaction between beads that would disturb tweezing functionality and single-molecule and -cell analysis | Constrain bead trapping to one cell per well (OCPW) by choosing the right bead properties. Subsequently achieve good occupation of the wells by:<br>• Using travelling waves to sieve beads<br>• By altering the standing wave field |
| 4. Trap volume of liquid | **By walls on all sides**<br>By walls on all sides except for the top<br>By surface tension (e.g. a drop on a plate) |
| 5. Insert and remove liquid | **Through a pipette**<br>Using a microfluidic pump |
| 6. Image both the DNA and the beads | **Directly**<br>Through an optical prism to change the imaging direction |

# Chapter 3

# Methodology

This chapter explains how the research was performed and consists of several parts. First several designs were explored and compared by testing several fabrication methods. Then, the best design was simulated and optimized. In addition, the fabrication and characterization methods are described as well as the employed bead manipulation and force measurement technique. Lastly, the tracking algorithm that was used will be explained.

## 3.1 Device design

### 3.1.1 Device layout

A transversal resonator layout was chosen for the acoustofluidic device. The benefit of this layout is that the acoustic resonances are less dependent on carefully tuned layer thicknesses needed for configurations where the transducers are placed in parallel with the intended field. Rather, the resonances of the system as a whole are more important. As the chip will have to be mostly made by hand, fabrication errors are unavoidable so a transversal type of resonator for the in-plane trapping was a safer choice. The vertical pressure field, needed to suspend the beads against gravity, would be created by a piezoelectric disk directly under the chamber, thereby forming a layered resonator.

The dimensions of the chip would follow from the boundary conditions needed for creating strong resonances. Assuming acoustically infinitely hard materials enables finding the resonance frequencies analytically. The normal velocity at the fluid chamber walls is then zero, which corresponds to the normal pressure gradient also being zero. For a rectangular cavity with opposite corners at $(0,0,0)$ and $(l,w,h)$ this results in the following pressure distribution assuming linear acoustics:

$$p_1(x,y,z) = p_\mathrm{a}\cos(k_x x)\cos(k_y y)\cos(k_z z) \tag{3.1}$$

where $p_\mathrm{a}$ denotes the pressure amplitude, $k_i = \pi n_i/d_i$ the wave number in which $n_i = 0,1,2...$, and $d_i$ one of the chamber dimension $(l,w,h)$. From this, the resonance frequencies $f_{n_x,n_y,n_z} = \omega_{n_x,n_y,n_z}/(2\pi)$ can be formulated as:

$$f_{n_x,n_y,n_z} = \frac{c_\mathrm{wa}}{2}\sqrt{\frac{n_x^2}{l^2}+\frac{n_y^2}{w^2}+\frac{n_z^2}{h^2}} \tag{3.2}$$

The height of the fluid chamber $h$ was chosen based on the rules of thumb compiled by Hawkes and Gröschl et al. [115, 116]. They respectively devised and modelled a 1D model based on a multilayer transfer matrix model for a layered resonator and formulated several conditions for strong pressure fields in the fluid layer that can be used as a general guideline. From their model, a reflector layer thickness of $\lambda/4$ together with a total acoustic path length (including the piezo) that equals a multiple of $\lambda/2$ gives the highest pressures. The exact layout and its dimensions were part of the research process and depended on which fabrication approaches were successful.

### 3.1.2 Materials

To minimize costs and to keep the device as simple as possible, the design scope was limited to the use of standard lab material as much as possible. This allowed to make quick iterations in the prototype. The

properties of glass such as its transparency, chemical inertness, thermal stability, biocompatibility, and its non-porous nature, make it a suitable material for many microfluidic applications [117, 118]. Moreover, the acoustic impedance ratio with water $(\rho_{gl}c_{gl})/(\rho_{wa}c_{wa}) = 9.7$ provides a hard acoustic boundary. Glass slides and cover slips were chosen as they are widely available. In addition, the cover slips are available in matching dimensions and in several thicknesses, ranging from 0.1 mm to 0.25 mm, allowing to optimize the standing wave field. For these reasons, the basis for the fabricated devices were chosen to be glass microscopic slides and cover slips.

The choice of the piezoelectric transducers was narrowed down to small disks 10 mm in diameter with a thickness of 0.2 mm made by Physik Instrumente (PI) GmbH & Co [119]. They have a high resonance frequency of around 10 MHz which would be needed to form sufficiently small in-plane traps for the beads to reside in. The paper by Kamsma et al. [90] shows that the piezo thickness is an important predictor of the field strength. Two types of piezoelectric transducers were ordered, made of a soft (PIC255) material that would give larger displacements and a hard (PIC181) material suitable for higher power applications giving off less heat.

## 3.2 Measurement setup

A schematic overview of the measurement setup is given in Figure 3.1 below.

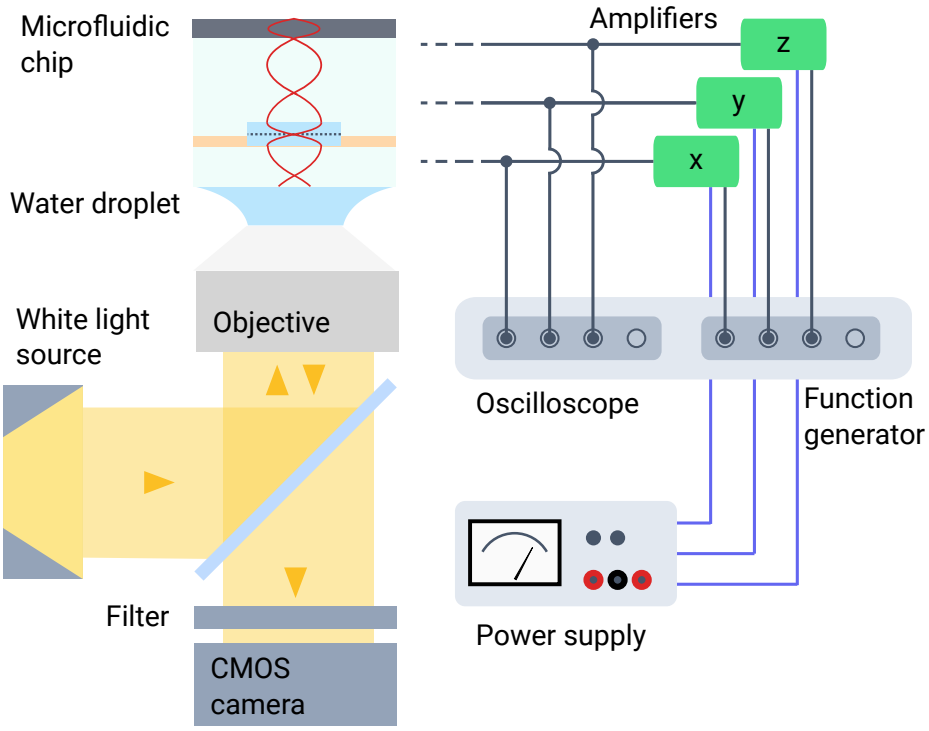


**Figure 3.1:** Schematic showing the measurement setup that was used. The left side contains the inverted microscope configuration of the Nikon Eclipse T*i*2. On the right, the electrical setup to power the piezoelectric transducers is depicted.

A Nikon Eclipse T*i*2 inverted microscope was used with brightfield light settings. This microscope can be operated in reflected, or episcopic (EPI), illumination which enables viewing and illuminating the beads from the same direction. This was required as the opaque piezo prevents light from passing through the chamber. The camera attached to the microscope (Prime BSI Express, Teledyne Photometrics) had a resolution of 2096x2096 pixels. The maximal image acquisition rate for this camera was 50 frames per second (FPS). A water immersed objective with a magnification of 60x and a standard 10x magnification lens were used in the experiments, providing a spatial imaging resolution of 0.072 µm and 0.44 µm per pixel, respectively. The microscope was equipped with a motorized stage which had a step size of 0.1 µm in-plane and 0.05 µm in the vertical direction.

In the electrical part of the setup to drive the transducers, the Moku:Pro by Liquid Instruments served

both as an oscilloscope and function generator, which could be controlled through their Moku software. The signals to drive the transducers were sent through three separate current feedback amplifiers (Analog Devices ADA4870). These were powered by a 40 V power supply. In factory default settings these amplified the signal by 4.5. Together with the +14 dB output gain settings on the Moku, a peak-to-peak voltage of 40 V could be attained. The slew rate of 2500 V $\mu s^{-1}$ was sufficient for the maximal needed frequency of around 20 MHz.

### 3.2.1 Microbeads

The interaction force plays an important role in patterning capabilities and depends both on the properties of the particles and the fluid [73]. Therefore the choice of beads and their size needed consideration. Polystyrene beads seemed like a good starting point as they are often used in patterning applications [39, 71, 72]. They have similar acoustic properties as cells and have therefore been used for calibration of cell patterning devices [72]. In addition, polystyrene has a similar density as water, which would make levitation easier. For the choice on the diameter an overview with successful patterning in literature was made (Table 3.1). Here $d$ is the particle diameter and $\lambda$ the wavelength of the field.

**Table 3.1:** Overview of the normalized beads sizes used in literature to obtain OCPW trapping.

| Authors | Size | Notes |
|---|---|---|
| Yang et al., 2022 [39] | $d/\lambda = 0.11$ | For the fundamental frequency of 40 MHz |
| Collins et al., 2015 [71] | $0.28 \leq d/\lambda \leq 0.31$ | Theoretical prediction (when $F_{PRF} > F_{SRF}$): $0.25 \leq d/\lambda \leq 0.33$ |
| Silva et al., 2019 [72] | $0.1 \leq d/\lambda \leq 0.4$ | Only experimentally verified for $d/\lambda = 0.32$, though the OCPW pattern was not achieved consistently. |

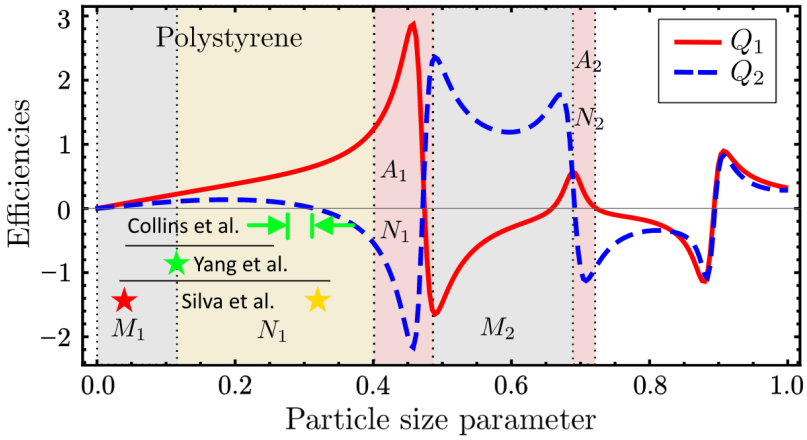


**Figure 3.2:** Plot of the efficiencies and the trapping region from Silva et al. [72] with indications of other OCPW attempts in literature (green means successful OCPW; yellow means partly successful OCWP; red means unsuccessful OCPW). Labels $N_i$, $M_i$ and $A_i$ refer to nodes, midpoints and antinodes, respectively. The efficiencies $Q_1$ and $Q_2$ relate to the components of the ARF.

The work on OCPW is limited and only Collins and Silva et al. [71, 72] explicitly present a range of suitable diameters. The theoretical range given Collins et al. [71] is based on the relative strength of the primary and secondary radiation forces and the available space in each well: the particle should not be too large ($d/\lambda \leq 0.33$) such that the SRF dominates, nor too small ($d/\lambda \geq 0.25$) which would allow more particles to fit in one potential well, as the distance between the wells can be $0.5\lambda$. Silva et al. [72] on the other hand state a lower limit of 0.10 as particles would otherwise gather around midpoints and cluster together. When $d/\lambda > 0.40$ the effect of the SRF grows, which would disturb the OCPW pattern. The SRF is limited to 15% for $d/\lambda < 0.40$. Their lower limit is close to the diameter used by Yang et al. [39], who made no comment on problems with multiple particles in one well. An overview of the particle sizes used and their effectiveness is shown in Figure 3.2. In this figure the efficiencies relate to the ARF. What is important to note

are the trapping regions and the peaks that indicate particle resonances. All in all, a particle size in the range of $0.15 \leq d/\lambda \leq 0.30$ seemed the best choice: more than one particle could be trapped in a pressure node but the influence of the secondary radiation force would be limited. The experiments were performed with 15 µm polystyrene micro particles (Sigma-Aldrich), imposing a wavelength range of 50 µm$\leq \lambda \leq$100 µm. The beads were diluted with Milli-Q by a ratio of 1:20.

## 3.3 Finite element analysis

For a one-dimensional model, it is possible to capture the system in a set of several equations. However, for systems beyond 1D, analytical methods no longer suffice and numerical simulations are needed. Simulations were carried out to estimate the performance of the devices to trap the beads. Finite element method (FEM) studies in COMSOL Multiphysics 6.1 were performed for this.

The aim of this FEM study was to find out the differences in performance between the feasible design. Three device layouts were compared to find out which one was best. The layouts differed in the method used to bond the microscope slide to the cover slip, which seals the microfluidic chamber. In the first configuration, the channel is cut into the the tape layer. The second configuration is similar but here the channel also extends into the microscope slide. The idea behind this approach is that even though the channel is deeper, more acoustic energy can enter the chamber as the glass surface area surrounding the chamber is larger. In the third configuration UV glue is used. This is applied between cavities in the cover slip rather than in between the cover slip and the slide to lower the risk of clogging the channel with the glue.

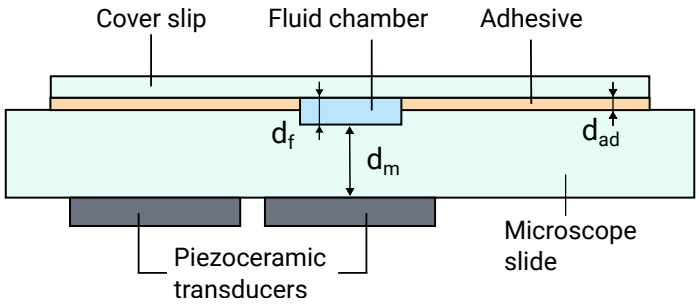


**Figure 3.3:** Schematic showing the general layout of the 2D model used in the finite element analysis. The dimensions highlighted in the figure and the adhesive material are the parameters that were changed between the models.

To reduce the computation time, a simplified 2D model was used. The general layout is shown in Figure 3.3. Note that the glue and aluminium layers to respectively connect the transducer and create electrical contact are not present in the model. In addition, the layer thicknesses are similar to the true values but the model was scaled down in width by around a factor of 2.5 to around 10 mm. Even though these simplifications reduce the resemblance to the real life chip, a performance comparison should still give insight into the trapping efficacy of each layout.

Damping was included per domain. For the solid parts an isotropic loss factor was used [74]. To model the acoustofluidic losses in the bulk of the fluid and at the walls, only a viscous boundary layer loss factor was included. Although there are other acoustofluidic losses like thermal losses and viscous losses in the bulk fluid, Hahn and Dual [120] showed that this is the predominant source of dissipation. However, this depends on the mode shape and device geometry. As the geometry and frequencies are similar in the presented setup, this was also assumed to be the case here. All simulations were run on a laptop with 8 GB of RAM.

An overview of the material parameters used in the models in shown in Table 3.2. The dilatational modulus was used rather than the Young's modulus as the wavelength of the longitudinal wave was smaller than the transverse dimensions. A complete overview of the dimensions, transducer parameters and other model settings can be found in Section 4.7.

**Mesh convergence** To obtain a sufficiently accurate solution within a reasonable time, a mesh convergence study was performed prior to the simulations. A convergence parameter $C(g)$ was calculated over a range of mesh sizes as a function of the number of elements per wavelength in each domain. The convergence

**Table 3.2:** Overview of the material properties used in the simulations. All parameters are retrieved from the COMSOL material library unless otherwise specified. The longitudinal speed of sound $c$ was calculated as $c = \sqrt{\frac{D}{\rho}}$, where $D$ is the dilatational modulus.

| Material property | Symbol | Unit | Soda lime glass | Borosillicate glass | NOA 61 | Kapton tape |
|---|---|---|---|---|---|---|
| Density | $\rho$ | kg/m$^3$ | 2500 | 2510 | 1290 | 1420 |
| Poisson's ratio | $\nu$ | - | 0.23 | 0.208 | 0.34 | 0.34 |
| Young's modulus | $E$ | GPa | $73 \cdot 10^9$ | $72.9 \cdot 10^9$ | $1.1 \cdot 10^9$ | $2.5 \cdot 10^9$ |
| Speed of sound | $c$ | m/s | 5818 | 5710 | 1146 | 1646 |
| Isotropic loss factor | $\eta$ | - | $1 \cdot 10^{-4}$ [121] | $1 \cdot 10^{-4}$ [121] | 0.04 [122] | 0.02 [123] |

parameter gives an indication of how different the result of a certain mesh size is when compared to the result with the finest simulated mesh. This parameter is defined as follows:

$$C(g) = \sqrt{\frac{\int_\Omega |g - g_{\text{ref}}|^2 dS}{\int_\Omega |g_{\text{ref}}|^2 dS}} \tag{3.3}$$

where $g$ is a field variable and $g_{\text{ref}}$ the reference calculated with the finest mesh and is used to compare the values of $g$ to for decreasing mesh sizes. For each number of elements per wavelength, the mesh sizes differ in each domain due to the different sound velocities. The pressure $p$ in the fluid domain and total displacement $\sqrt{\mathbf{u} \cdot \mathbf{u}}$ and velocity $\sqrt{\mathbf{v} \cdot \mathbf{v}}$ in the solid parts were used as field variables. The result is shown in Figure 3.4a.

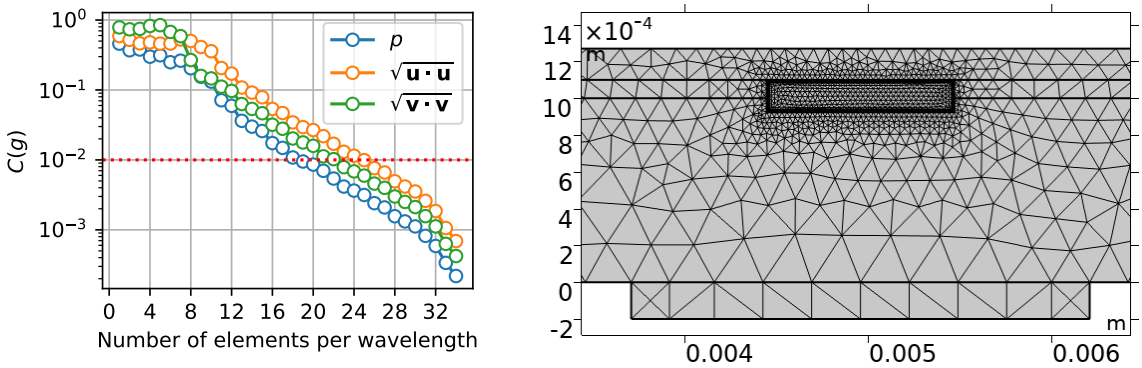


**(a)** **(b)**

**Figure 3.4:** (a) Results of the mesh convergence study. At 25 elements per wavelength, the error $C(g)$ reduced to 0.01 with respect to the finest mesh. (b) View of the meshed model of configuration 2 with predominantly triangular elements (apart from the boundary layer elements, which are rectangular). The number of elements per wavelength was reduced to 1 to better visualize the mesh structure.

It can be observed that all measures decrease exponentially. About 25 elements per wavelength seemed a reasonable choice, resulting in a relative convergence of $C(g) = 0.01$ and around $8 \cdot 10^5$ elements, though this number would differ for the other configurations. This number of elements per wavelength was used for all other simulations as well. For each layout, the acoustic field in the fluidic chamber was evaluated in both the vertical and horizontal direction. This was done by extracting the acoustic pressure profile along several lines crossing the chamber. This pressure gradient appears in the expression (Equation (1.3a)) for the radiation force and was therefore used as an indicator for the magnitude of this force.

## 3.4 Fabrication and validation

**Laser cutting** For creating the microfluidic channels in the glass slide. laser microfabrication was chosen. This method is especially well suited for prototyping as micrometer sized features can be realized within

reasonable times (typically one or two hours) [124]. In addition, compared to other methods like etching, the whole process involves fewer steps as no masks or postprocessing steps are required other than cleaning [125]. A nano- or femtosecond laser cutter were available, of which the femtosecond laser was preferred as it gives less cracked and cleaner edges. This is shown in Figure 3.5.

A femtosecond laser cutter can remove material by firing very short laser pulses that last only a few hundred femtoseconds. The high energy density at the pulse focus allows the machine to cut not only opaque but also transparent materials. This happens because the high peak intensities cause a non-linear absorption process called multiphoton absorption [118, 125]. The pulse energy can therefore be delivered in a highly localized way such that material removal is limited to the pulse focus. Thanks to this precise energy delivery there is only a small heat affected zone so the surrounding material remains mostly unaffected. A high spatial resolution and accuracy can thus be obtained.

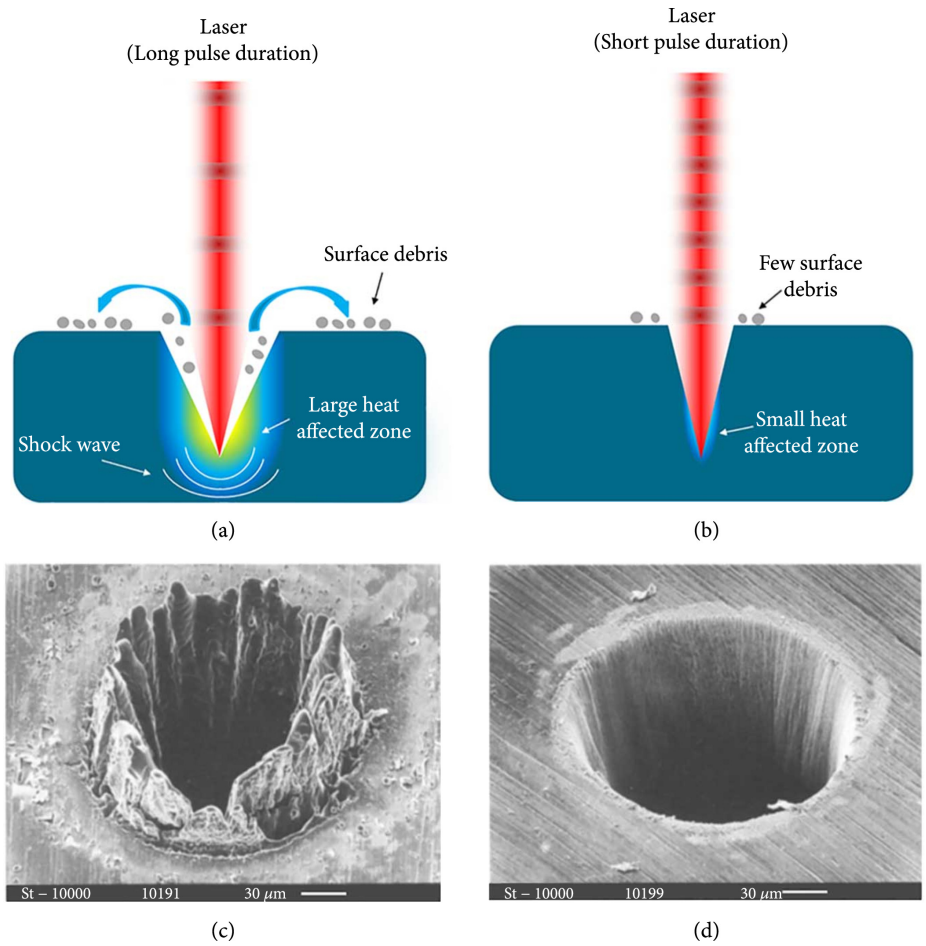


**Figure 3.5:** Schematic from Lin et al. [126] showing a comparison between a nanosecond (a,c) and femtosecond (b,d) lasercutter. The bottom two figures show Scanning electron microscope (SEM) images depicting laser-ablated perforations created on a 100 µm thick steel sheet. In comparison, the femtosecond laser enables a cleaner cut owing to the shorter pulse duration.

The microfluidic channels were made with a LASEA femtosecond laser cutter. The laser cutting settings were determined by a combination of the Taguchi optimization performed by Tsan [40] and trial and error. An overview of the laser cutting settings is given in Section 4.7. These were mainly based on the requirement for sufficiently smooth surfaces in order to reduce the amount of scattering to obtain good reflections. The ultrasonic wave is not much affected upon reflecting if the scale of the surface irregularities is about two orders of magnitude smaller than its wavelength. As the applied frequencies (1-10 MHz) have wavelengths of a few hundred microns, this requires a roughness of at most a few microns [73, 127].

**Bonding** To bond the layers together, including the piezoelectric transducers, cyanoacrylate adhesive was found to be suitable. This has also been used regularly in literature [8, 85, 90, 103]. Air cavities in the

glue layers should be avoided as they act as strong reflectors and diminish the power delivered to the fluid chamber. After the glue had dried, leakages could be checked with food-coloured water. Next to glue, also the use of tape was explored. This is easier to handle and there is no risk of clogging the channel.

**Characterization** Modelling the system only had a limited use due to its complex nature. The intricate interactions between the fluid and the surrounding chip material, including the piezoelectric transducer, made its performance hard to predict. In addition, discrepancies in material properties and dimensions could also have a large influence. As the performance depended on the excitation of the right frequencies, it was valuable to find these frequencies beforehand. It would have been possible to approximately find the resonance frequencies experimentally by assessing the movement of the beads but this is both time-consuming and has limited precision. Therefore, after fabrication, validating the device was essential. First, the dimensions and surface roughness were validated using an optical microscope (Keyence Digital Microscope VHX-6000). After that, the frequency response of the system was analyzed. There were several methods that could be used.

A common method to characterize the dynamic behaviour of the system is to determine the electrical impedance over a frequency range. The impedance $Z$ captures the difficulty with which a current can flow through an element. When a device is driven at its series resonance frequency, the impedance shows a minimum and the device turns electrical energy into mechanical energy most efficiently. As shown by Dual et al. [128] this method is especially well-suited to analyze the dynamic response of the piezoelectric element. When the same analysis is performed on the complete device, the peaks are less pronounced and harder to distinguish due to additional structural resonance modes. It should also be noted that this method requires a strong electromechanical coupling between the piezo and the microfluidic chip. The impedance profile was determined using the Frequency Response Analyzer (FRA) on the Moku:Pro. The measured power (in dB m) could be rewritten to the input voltage after which the impedance of the device under test follows from Ohm's law. The complete calculation is provided Section 4.7.

The impedance characteristic could also be modelled, using so-called equivalent circuit models. Given that the piezoelectric effect sits at the intersection between the electrical and mechanical domain, it is essential to adequately represent this interaction for accurate system modeling. This electromechanical behaviour can be captured in an equivalent electrical circuit. In such a model, the piezoelectric material is divided into an electrical and an acoustic part using an ideal transformer, which relates the mechanical quantities into electrical equivalents [129]. This was first introduced by Mason [130] for a one-dimensional model. Later, Krimholtz provided a simplification which is now known as the KLM (Krimholtz-Leedom-Matthae) model [131]. In Figure 3.6 a schematic of this model for thickness mode of vibration is shown.

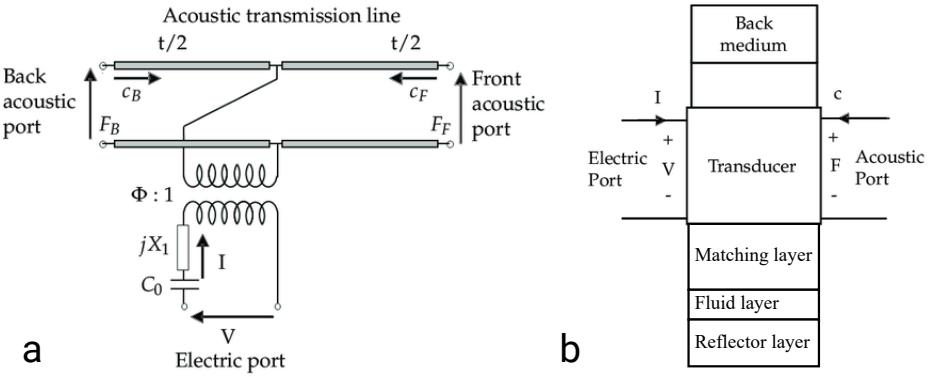


**Figure 3.6:** Schematic adopted from Kar and Wallrabe [132]. In the left figure (a), the KLM model of the transducer is given. The right model shows the KLM model of the transducer connected to a back medium on one port and to the matching layer on the other port.

In the left schematic, the KLM model with one electric port and two acoustic ports is given. The electric port consists of a clamped capacitance $C_0$ and a reactive impedance $jX_1$. The wave propagation on the mechanical side is represented as a lossy acoustic transmission line of length $t$ (corresponding to the piezo thickness) with the mechanical ports on both ends of the line. $F$ and $c$ are the forces and velocities at the front (subscript F) and back (subscript B) faces of the transducer Both parts are connected through a transformer

where $\phi$ is the ratio between the electric voltage and mechanical force. This model was used to calculated the frequency dependent impedance and the vertical resonance frequencies of the fluidic cell.

The MATLAB script provided by Kamsma et al. [90] was used for this. In this script, first the impedance of port 2 which is the impedance seen by the piezo is determined. This is done by calculating the mechanical impedance of each layer. The details of this method are given by [133]. Then, the impedance of the transducer is calculated over a range of frequencies using additional relations found in Sherrit et al. [129]. Finally, the force at generated force of the piezo together with impedance of each layer enable to calculate the pressure profile in each layer.

## 3.5 Bead manipulation

To control the position of the beads, mode switching was used. Even though the node positions in the chamber were fixed, switching between two modes enabled to also cover the space in between the mode's equilibria for acoustic trapping. To generate this alternating pressure field, a Moku:Pro signal generator by Liquid Instruments was used. With this device it was possible to generate a square wave which was then used as the input for the frequency modulation that could be set to switch between two acoustic modes at an identical peak-to-peak voltage. By adjusting the ratio of the high and low periods of this square wave, the mix of these modes could be controlled. For a low modulation frequency the beads would just alternate between the two nodal position. By increasing this frequency, however, the beads have increasingly less time to move to their new equilibrium, before the mode switches again. At a sufficiently short switching time, the beads converge to one position. The overall effect can be perceived as a result of a single, time-averaged force profile, which can be described by the following expression:

$$F_{i,j} = \frac{T_i}{T_s} F_i + \frac{T_s - T_i}{T_s} F_j \tag{3.4}$$

where $F_{i,j}$ is the resulting force profile, $T_i$ the time mode $i$ is actuated, $T_s$ the switching period and $F_i$ and $F_j$ the force profiles of mode $i$ and $j$, respectively. An example of the resulting force profile is shown in Figure 3.7a for the case of equal force profile amplitudes. The relative equilibrium positions highlighted here are plotted in Figure 3.7b. It is clear that the position changes slowly at first but then drops down to its final equilibrium in the half wave node after a certain percentage is reached.

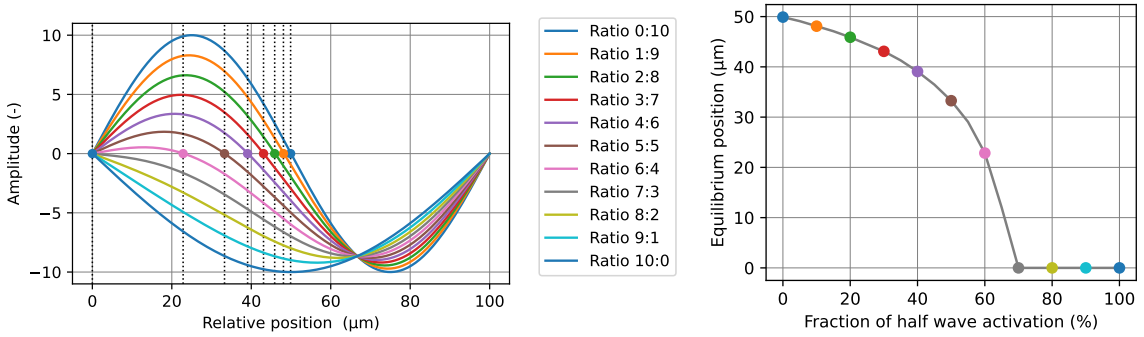


**(a)** **(b)**

**Figure 3.7: (a)** Time-averaged force profile when mode switching is applied with a half wave and a full wave mode for different activation ratio's (half-wave: full-wave). The equilibrium positions are marked with dots and black lines. **(b)** Resulting equilibria positions for a range of half wave activation ratios.

## 3.6 Force measurements

There exist several methods to make an estimation on the trapping force. Some allow to determine the force directly, for example by analyzing the kinetics when the particle is in motion. Other methods use position measurements and first require the trap stiffness to be calculated. These include the equipartition, power spectrum and drag force methods. Furthermore, the drag force methods are based on introducing a fluid flow

along the particle. The trap stiffness then follows from the known viscous drag coefficient of the particle and the fluid's flow velocity. The other methods are less time-consuming as they do not require applying an artificial fluid flow. The equipartition and power spectrum method are both suitable but require accurate bead tracking. This is also true for the kinetics method where the acceleration needs to be determined, which requires a high FPS camera to obtain a smooth acceleration curve. As the available camera only had a 50 FPS acquisition rate, this method was not suitable. A more rudimentary yet effective method involves monitoring the path of beads as they move towards the pressure nodes. The stiffness can then be inferred from the predicted force profile. This method was used in the experiments below.

## 3.7 Bead tracking

Measuring the stiffness of the potential wells in which the beads reside requires accurately tracking the position of the beads. For the observations only conventional microscope setups were available which only allows optical access through a single objective. To obtain three-dimensional particle tracking with a single camera, first the coordinates of the beads in the image have to be estimated. After localizing the beads, their positions have to be linked together frame-by-frame throughout the video into separate trajectories [134].

To localize the beads on the image plane, there are many methods available like cross-correlation [135], sum of absolute differences, quadrant-interpolation [90], radial symmetry center methods [136], center-of-mass fitting and Gaussian fitting [137, 138]. More recently, a method termed the radial variance transform (RVT) was introduced by Kashkanova et al. [139]. As this method is also suited for larger particles and shows good performance in comparison to the other methods, this method was chosen for the localization. The RVT algorithm makes use of the radial symmetry of a particle image, which results in two observations. The first observation is that pixels at a fixed radial distance from the center roughly have the same values. Secondly, the means of theses values differ across the radial distance. The center of a particle can therefore be distinguished as the location with a low mean of variance (MoV) and a high variance of means (VoM) over the range of radial distances. In Figure 3.8 the general algorithm is illustrated. After high-pass filtering the image, the $r$-means ($M_r$) and $r$-variance ($V_r$) are calculated for each pixel $(i, j)$. A basic and normalized RVT can then be calculated from the VoM and MoV. Figure 3.8*b* shows that the RVT algorithm also works on an image with multiple beads.

The RVT algorithm performs $O(N^2 r_{\max}^2)$ operations for a single image, where $N$ is the size of the image and $r_{\max}$ the maximal considered radius for each pixel. Ideally, many beads are tracked simultaneously so the image size should be large. However, as each measurement also lasts at least several seconds, analyzing a video at a sufficient FPS rate can take a long time. To speed up the process, the TrackPy Python package could be used.

TrackPy operates by identifying and tracking distinct features or particles across a series of images. One of the benefits, compared to other tracking methods, is its ability to efficiently link these features into coherent trajectories over time. In addition, it is flexible and can be easily integrated with the Python ecosystem which is well-suited for scientific analyses. It performs well on tracking blob-like features but during initial testing with a 60x magnification lens it did not find the center of the particle and had significant errors. This magnification would be needed if force spectroscopy with smaller samples would be performed.

One solution was to combine both the RVT method and the TrackPy package together. That way, a more precise localization could be achieved while also having the benefit of easily linking this localization into trajectories. The computation could be sped up by only calculating the RVT around the beads that were coarsely localized by TrackPy and discarding most of the background. The flow diagram is shown in Figure 3.9.

To estimate the precision and accuracy of the adopted method, it was tested on a set of images with known bead locations. For this, the beads were first immobilized in a 0.5wt% low melting agarose solution. Then 9 images were taken by moving the motion stage such that the bead moved within the field of view in a 3x3 grid. That way, the relative distances were known and could be checked with the algorithm. In addition, for each in-plane location, the z-stage was swept over a 40 µm range to also check the influence of the defocusing. This was performed with both the 10x and 60x magnification objective lens. The acquired estimate for the precision is shown in Figure 3.10.

It can be seen that the 60x magnification objective performed worse than the 10x objective. This could be due to the larger change in illumination angle for the former. The image in the bottom right of Figure 3.9 shows this effect.

To obtain an estimate for the accuracy, the relative shift of the beads with respect to each other was

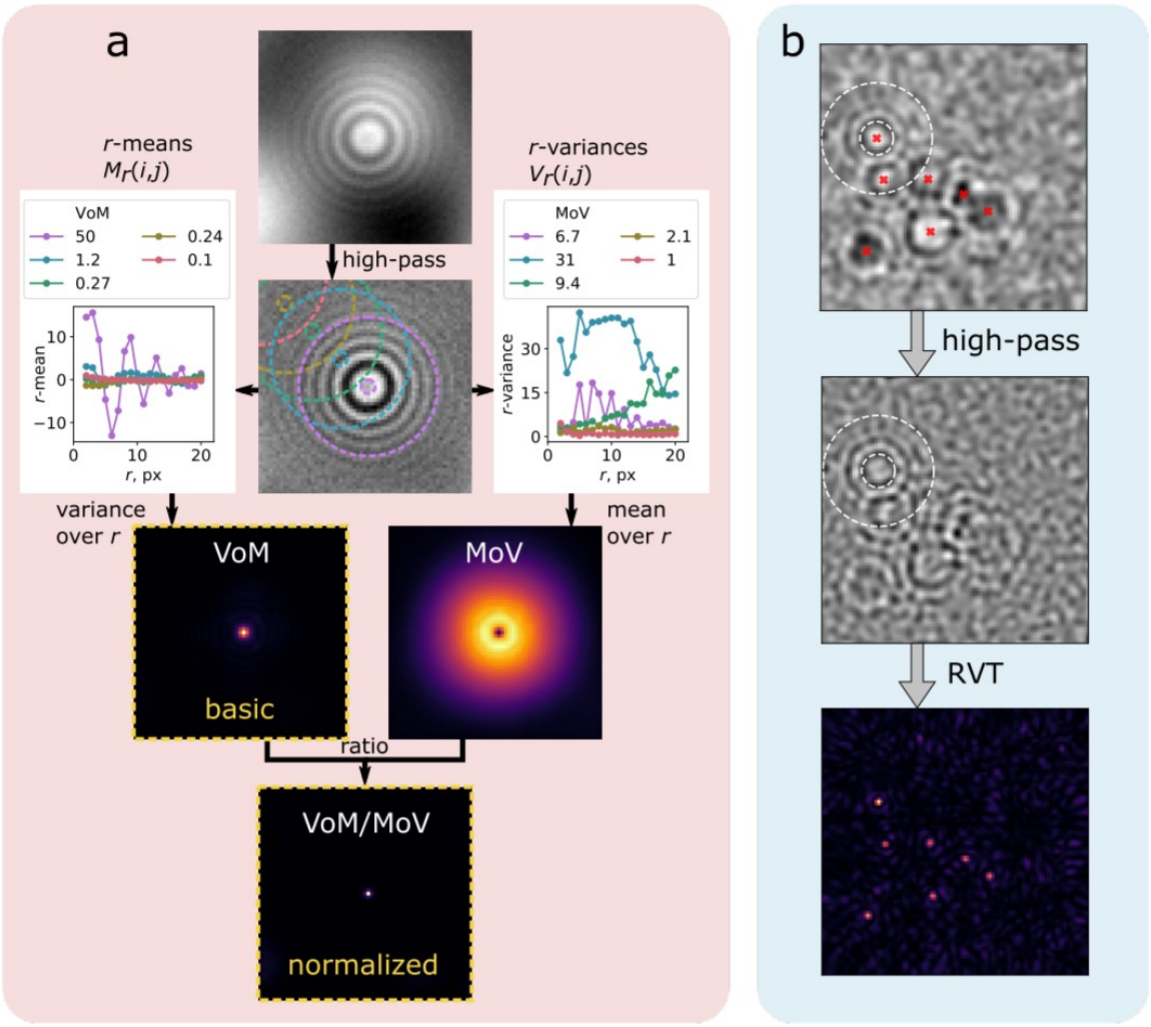


**Figure 3.8:** (a) Schematic showing the steps involved in the RVT algorithm to localize the beads in-plane. First, the image is high-pass filtered to ... large-scale noise. Then both the $r$-means ($M_r$) and $r$-variance ($V_r$) are calculated for each pixel $(i, j)$. A basic or normalized RVT can then be extracted from the variance of means (VoM) and mean of variances (MoV). (b) The RVT performed on a synthetic image with challenging levels of noise and overlap. The true locations of the point-spread functions are indicated by the red crosses.

used. The shift of the beads in the field of view could be compared with the expected shift of the motor stage. Accounting for the error of the motor stage (0.5 µm) and from the scale bar conversion (0.7 µm), the remaining error had to come from the tracking accuracy. For the 60x magnification this was 1.90 µm and for the 10x magnification 3.4 µm

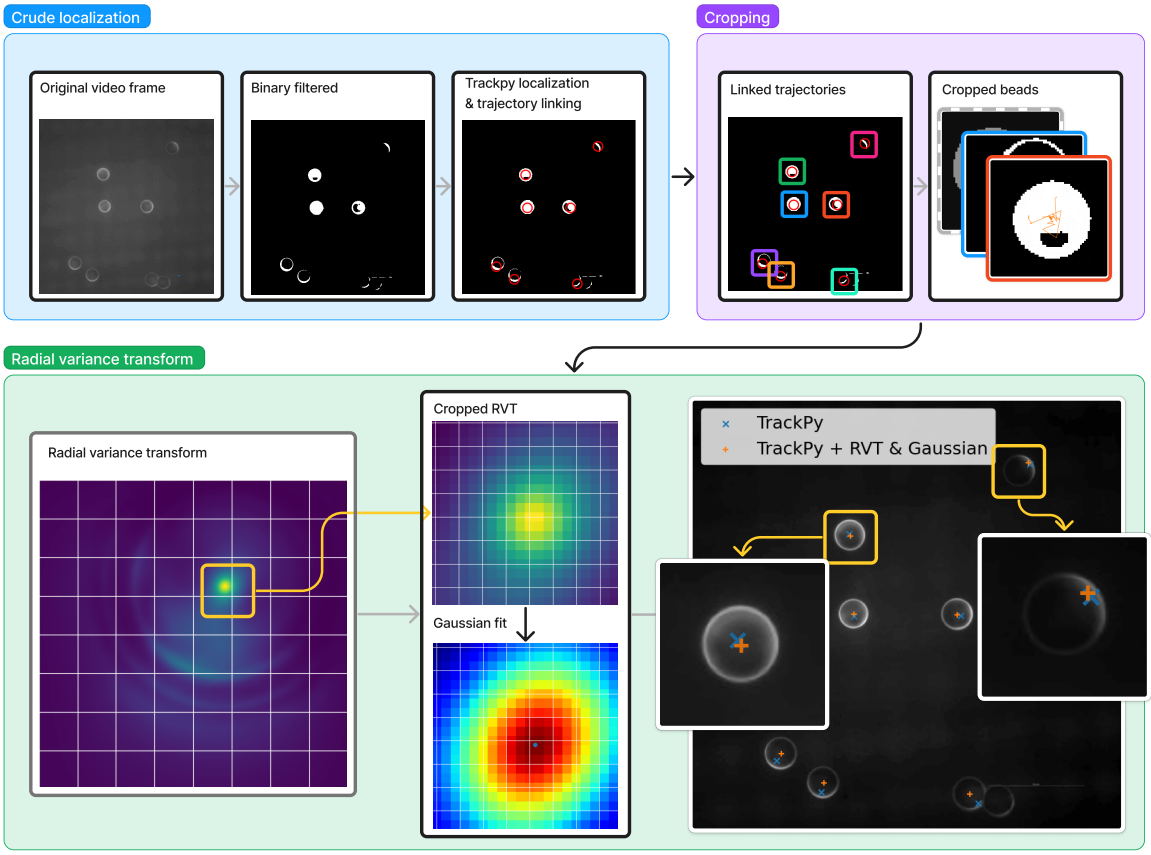


**Figure 3.9:** Flow diagram showing the process of bead tracking in 2D. First image was filtered to improve bead detection. Then, the beads positions were approximated by Trackpy. By cropping the beads images, the computation time of the RVT algorithm was reduced. A 2D Gaussian was fitted to the area around the brightest pixel. In the bottom-right image, it can be seen that the algorithm worked quite well for well-illuminated beads but also had a deviation when the signal-to-noise ratio was low.

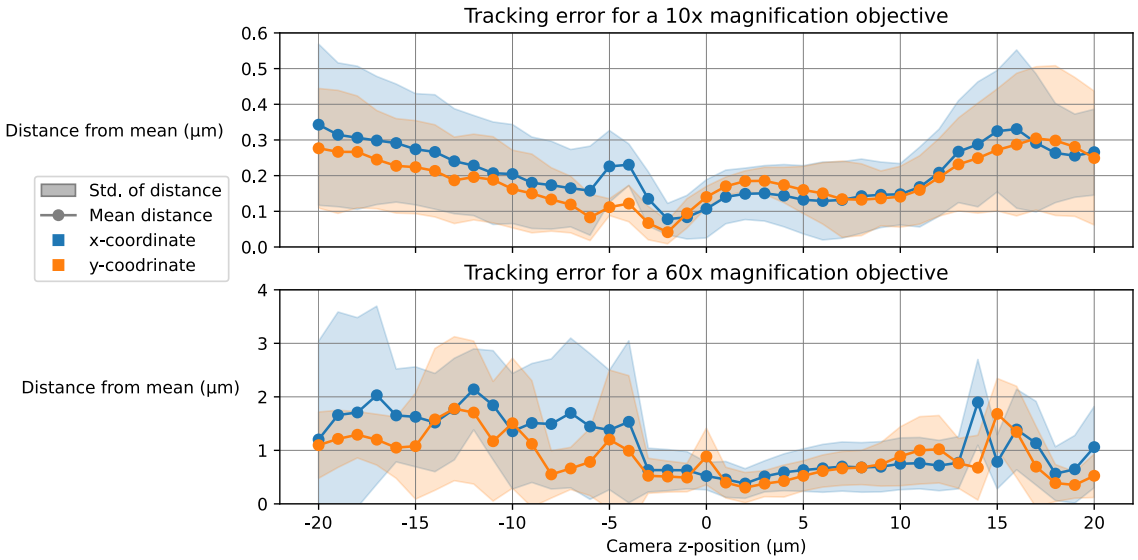


**Figure 3.10:** Precision of the RVT algorithm for a range of z-values. These represent the average of the 9 in-plane locations that were used. The beads were in focus at a z-position of 0 µm

# Chapter 4

# Results

This chapters presents the results that were obtained. First, the design process of the device is covered, followed by several finite elements studies. Then, an overview of the fabrication process of the microfluidic device is given. Finally, the results from the chip operation are discussed.

## 4.1 Device design

The first step in the prototype design was to decide what layout should be used. From the proposed materials and the fabrication methods, it became clear that this layout would approximately look like the one shown in Figure 3.3. Here, the fluid chamber is created by a cut through the adhesive layer and into the glass slide. The cover slip then seals the chamber and provides optical access. On the bottom, the piezoelectric transducers are mounted. The central piezo forms the layered resonator, providing the pressure gradient needed for levitating the beads. The piezo on the left is responsible for giving rise to an in-plane pressure field in which the bead manipulation will take place. With this design layout, most of the overall configuration had been determined. However, a large part of the realization of an effective resonator comes down to choosing the right dimensions.

In order to find a feasible range of dimensions, different types of bonding were first tested. The primary bottleneck in the fabrication process was achieving a bond that was both strong and ensured a leak-tight seal of the chamber. By testing different bonding approaches it was found that three configurations were possible. The details of each method are discussed later on and an overview of multiple other methods that were tested can be found in Section 4.7. The 2D layout of the configurations were roughly equal. Only the adhesive material and thickness, and the fluid layer height differed. The first configuration is bonded by double-sided optical tape and the height of the fluid layer equals the thickness of this tape. The second configuration is similar but now the fluid layer also extends into the glass slide. In the third configuration, two adhesives are used: Norland Optical Adhesive (NOA) 61 UV glue and double-sided tape. The tape represents a sealing gasket to prevent leakage and the UV glue provides the bond through two cavities in the cover slip. Also in this configuration a cut in the slide is made. These three configurations were modelled and simulated in a finite element study to gain insight into the differences in performance for both z- and in-plane-trapping. Their layouts are shown in Figure 4.1. Below, the process of finding these dimensions is described for the vertical and in-plane directions.

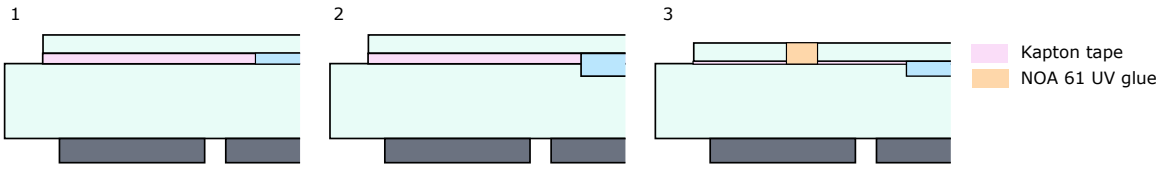


**Figure 4.1:** Schematic layouts of the configurations that were simulated. Only half of the device is shown for convenience.

**Dimensions in the vertical direction** In the vertical direction, the system behaves like a layered resonator. Consequently, the adhesive material and thickness significantly influence the quality of the acoustic

field in the fluidic chamber [8]. For that reason, the device would have to be modelled and optimized in order to obtain a suitable height of the fluid chamber $d_\mathrm{f}$, the adhesive layer $d_\mathrm{ad}$ and the matching layer $d_\mathrm{m}$. These dimensions were labelled in Figure 3.3.

For each layout, the fluid layer thickness was chosen using the rules of thumb stated earlier in Chapter 3. As not all rules can be satisfied simultaneously, the thicknesses of each device were chosen such that the differences between the devices was minimal to keep the comparison fair. In the left schematic of Figure 4.2 an example wave profile is illustrated. The results of this manual optimization based on the reflector layer condition are summarized in Table 4.1. It should be noted that for the first model, this condition could not be met together with a half-wave in the fluid layer as the tape thickness prescribed the fluid chamber height.

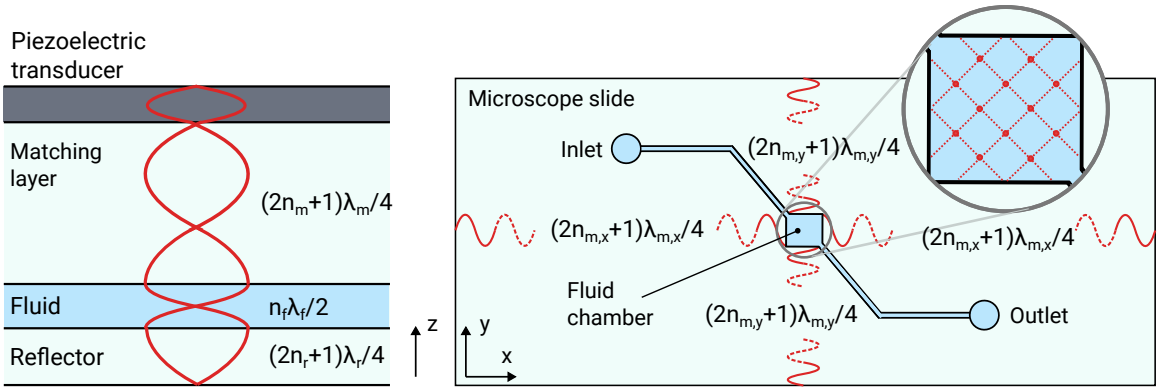


**Figure 4.2:** Schematic of the pressure field in the vertical (left) and in-plane (right) direction. The pressure field is visualized in red. Also the design requirements concerning the number of wavelengths are added. In the cut-out of the fluid chamber, the pressure nodes are added as red dots.

**Table 4.1:** Summary of the results of manually optimizing the layer thicknesses. The leading constraint was the quarter-wave reflector condition.

| **Configuration** | **1** | **2** | **3** |
|---|---|---|---|
| Adhesive material | Kapton | Kapton | Kapton & NOA61 |
| *Layer thicknesses*: | | | |
| $d_\mathrm{ad}$ (µm) | 100 | 100 | 25 |
| $d_\mathrm{f}$ (µm) | 100 | 177 | 88 |
| $d_\mathrm{m}$ (µm) | 1000 | 923 | 937 |
| *Number of wavelengths*: | | | |
| Fluid layer | 1 | 2 | 1 |
| Reflector layer | 0.22 | 0.25 | 0.25 |
| Matching layer | 1.27 | 1.33 | 1.35 |
| Total | 2.13 | 2.96 | 2.48 |

**Dimensions in the in-plane direction** The chamber length and width were selected based on the analytical expressions for the resonances when hard acoustic boundaries are assumed. This is graphically shown in the right schematic of Figure 4.2. Furthermore, the frequency of sound waves in both directions should not be a multiple of each other or of the one in the vertical direction. This is to prevent cross-talk between the modes, meaning that in addition to the desired mode, another mode would be excited, which would disrupt the field. Small variations in the chamber's widths are enough to decouple the resonances, though larger differences increase the robustness [64]. Additionally, the plane should be able to accommodate enough beads to demonstrate that multiplexing is feasible. The dimensions were therefore chosen such that at least 10 beads could be trapped in both directions. From Section 3.2.1 it became clear that for polystyrene beads, this gives a range in wavelengths of $50\,\mu\mathrm{m} \leq \lambda \leq 100\,\mu\mathrm{m}$.

Subsequently, finding a set of dimensions to use in the finite element simulations consisted of two steps. First, the frequency of the vertical trapping should be determined using the KLM equivalent circuit model

implemented in MATLAB by Kamsma et al. [90]. The reason for this is that the predicted half- or full-wave frequency could still deviate by a few hundred kHz from the frequencies of this more accurate model, which could result in cross-talk between the vertical and in-plane mode. After that, the width of the chamber was determined by the transversal resonator condition stated before. The constraints could be summarized as:

1. The width of the chamber should be similar to the width of the real design (around 1 mm)
2. The chamber width and in-plane frequency should be the same for each configuration.
3. The in-plane frequency should not be a multiple of any of the vertical modes.
4. The width of the device should adhere to the condition that $(2n_{\mathrm{m},y}+1)/4$ waves should exist on each side of the chamber.

This resulted in a chamber width of 1.023 mm, an in-plane frequency of 10.148 MHz, and a total slide width of 9.91 mm.

## 4.2 Finite element simulations

The simulation results for the vertical direction are shown in Figure 4.4 This result was obtained by analyzing the field at five positions evenly distributed along the chamber width in order to also take the homogeneity of the field into account. The pressure gradient at these locations is shown in Figure 4.3b. The frequency resolution was 5 kHz. It can be observed that the strongest pressure gradient occurs in the center of the chamber and decreases closer to both walls. A typical pressure profile and its gradient for the half-wave mode in the first configuration is shown in Figure 4.3a. As expected, a pressure node forms in the center and there the pressure gradient has its maximum (marked in green, $\overline{(\nabla_z p)}_p$). The average gradient peaks were combined for each configuration and shown in Figure 4.4.

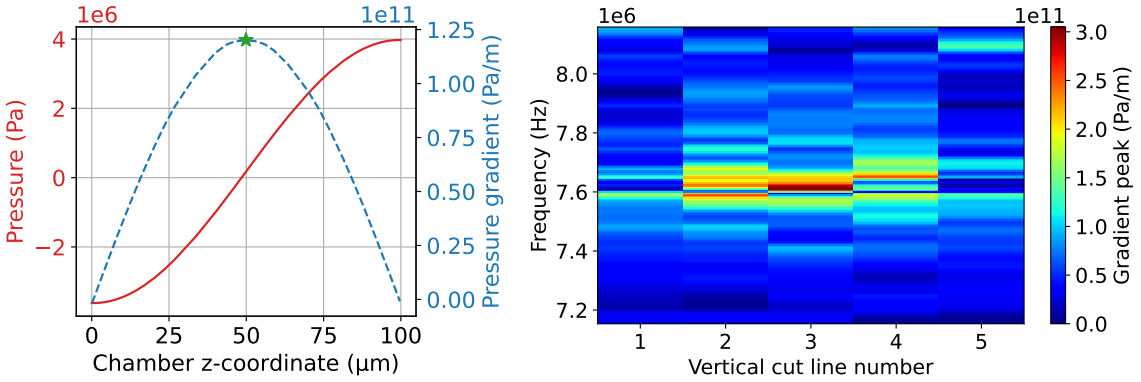


**Figure 4.3:** **(a)** Plot of one of the pressure profiles in the vertical direction. The peak of the gradient was used as a measure of the field quality. **(b)** 2D plot showing the distribution of the gradient peaks along five vertical 'cuts' over the chamber width.

There are several aspects about this plot that stand out. Firstly, the field in the third configuration had the highest gradient peak. This is in line with the results from the parameter sweep performed by Kamsma et al. [90], which indicates that a thinner fluid layer is beneficial. However, one would then also expect the maximum in configuration 2 to be lower than configuration 1, which was not the case. In addition to the difference in height of the gradient peak, also the variation in the gradient peaks over the frequency was larger in the third configuration.

For the in-plane, or horizontal, field the evaluation was done in a similar fashion. Again a sample of the pressure field was taken along specific lines, this time horizontally. As the goal was to also levitate the particles, the in-plane pressure field was probed at the height at which this levitation was meant to take place. For the first and third configuration this meant evaluating the field halfway the chamber height and for the second configuration, this was done at one and three quarters of the height. Typical pressure profiles

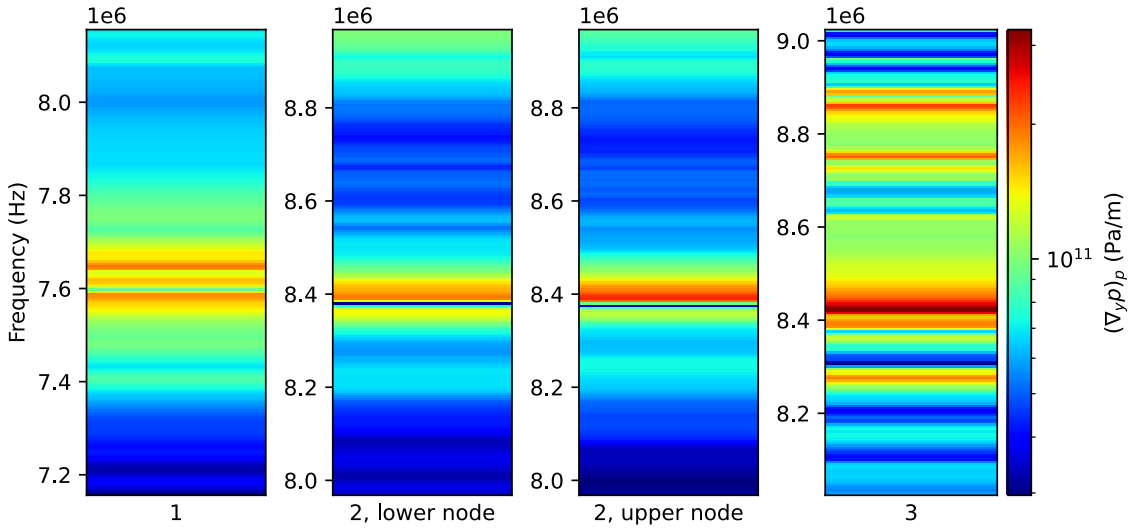


**Figure 4.4:** Results of the FEM simulation in the vertical direction for each configuration. Each plot represents the average gradient peak along the chamber width. Configuration 2 facilitates a full-wave mode and therefore has two nodes.

are shown in Figure 4.5 for configuration 2 and 3. The evaluation measures are also shown in this plot: the mean of the gradient peaks (black line, $\overline{(\nabla_y p)}_p$) and their spread divided by the gradient peaks' mean ($\sigma((\nabla_y p)_p)$ / $\overline{(\nabla_y p)}_p$). These two measures accounted for the fact that both a strong and a homogeneous field were desired. In Figure 4.6 the results of this analysis is shown.

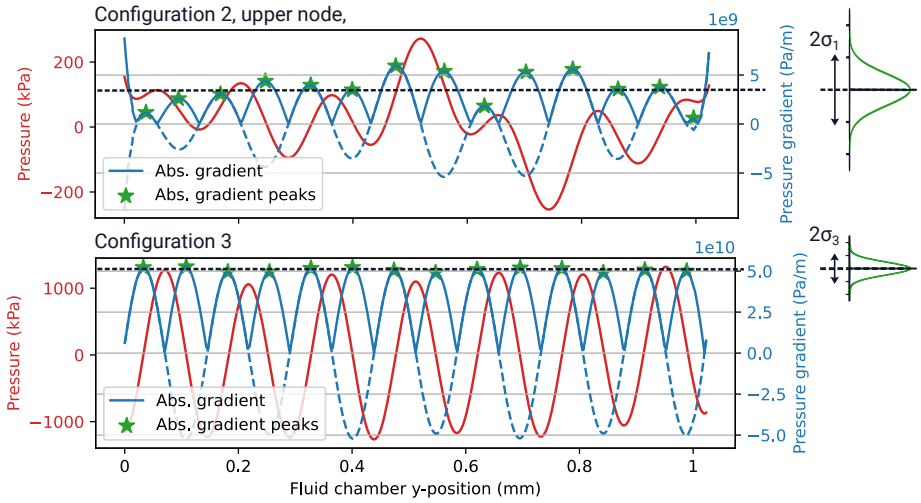


**Figure 4.5:** Pressure and pressure gradient profiles for the upper node in configuration 2 (top) and the half-wave node in configuration 3 (bottom). The mean of the gradient peaks and their spread are added. These two measures were taken as evaluation criteria of each configuration over the frequency range.

Again, configuration 3 performed better than the other two, both in terms of field strength (Figure 4.6a) and uniformity (Figure 4.6b). The plot for the standard deviation of the gradient peaks shows that the pressure field of configuration 3 was most homogeneous. What is striking is that the second configuration had the least uniform field.

From this analysis, it was apparent that a thin adhesive layer was important in creating a high quality, strong pressure field in the horizontal plane. Thus, it was valuable to look for methods to minimized this thickness while keeping a leak-tight seal and a strong bond. The fabrication method that was found is described in the following section.

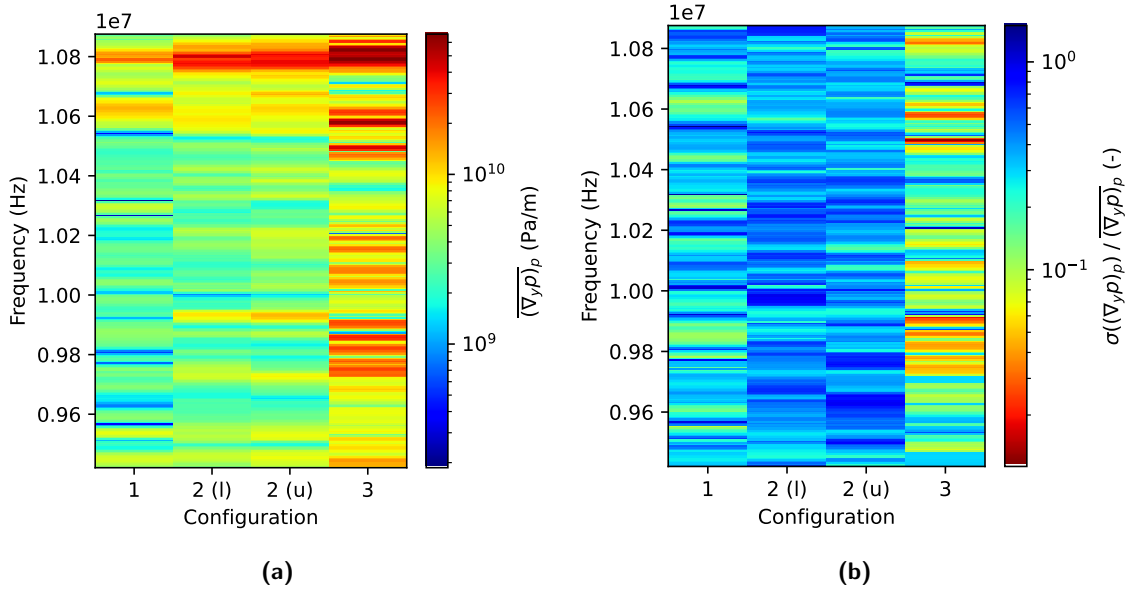


**Figure 4.6:** Results of the FEM simulation in the horizontal direction for each configuration around a frequency of 10.148 MHz. This frequency enabled the formation of a pressure field with 7 nodes. In the second configuration, the pressure field was evaluated at the lower (l) and upper node (u) separately. **(a)** The average height of the gradient peak over the 14 peaks. **(b)** The inverse of the standard deviation of these pressure peaks, divided by their mean. The inverse is shown to keep the same order of coloring where red indicates a better performance.

## 4.3 Fabrication

This section covers the fabrication and subsequent characterization process of the microfluidic chip with configuration 3. The fabrication for configuration 1 and 2 are explained in Section 4.7. The chamber dimensions were determined based on the design rules stated in Section 4.1. The height of the chamber should be 88 µm, forming a half-wavelength layered resonator. the horizontal dimensions were chosen such that each direction could support a 10 wavelength mode. Together with the requirement of $0.15 \leq d/\lambda \leq 0.30$, the length (in x) was chosen at 0.985 mm (for an operating frequency of 15.055 MHz) and the width (in y) at 0.879 mm (for an operating frequency of 16.863 MHz). These dimensions were such that minimal cross-talk would occur.

A flow diagram for of the laser cutting and bonding process for configuration 3 is shown in Figure 4.7. The two methods are presented (path a and b) differ in the way the gasket was implemented. For the sealing gasket that provides the leak-tight bond, cling film was used. With a thickness of about 13 µm it enabled a larger ratio of glass in the chamber walls. Parafilm also proved to be effective but its thickness was almost twice as large.

The first method (a) started with covering a microscope slide with the sealing film. The microscope slide should then be heated shortly to make the film stick to the surface. Then, the channel could be cut into the slide using the femtosecond laser cutter (2a). Additional cuts were made into the film to later allow the adhesive to make contact with the slide (4a,b). Then, several cuts were in the cover slip were added: an input and output for inserting the fluid and cavities to later apply the glue in (3a). After sonicating and cleaning the cover slip to remove any debris from laser cutting, the cover slip could be bonded with the microscope slide (5a,b). This was done by placing the stack on a hot plate for about ten minutes while applying an even force (roughly 3 N), for example by placing a beaker filled with water on top. Lastly, a strong adhesive like cyanoacrylate glue was applied in the cover slip cavities to anchor the connection with the microscope slide (6 and 7 a,b).

The second method (b in the figure) is almost identical to the first method. The difference is that the laser cutting the slide is done before adding the sealing film, which allows it to be cleaned more thoroughly by sonication. After applying and subsequently heating the film, the channel is then also covered but this can be removed by laser cutting the perimeter of the channel. A downside of this approach is that it is more challenging to have good alignment of both cuts, which is not applicable in the first method. All subsequent results were obtained with a chip fabricated using the first method.

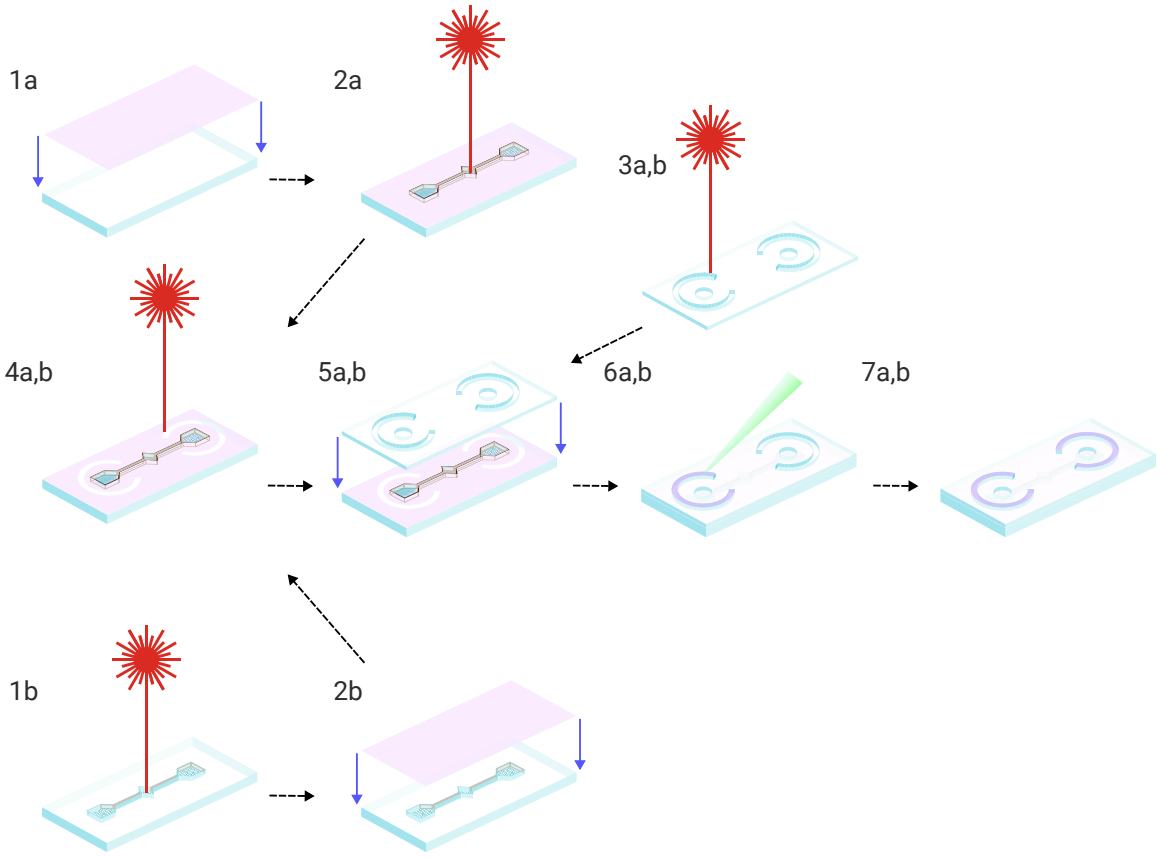


**Figure 4.7:** Diagram showing the fabrication processes of the acoustofluidic device. The sealing film is colored pink. After laser cutting steps 1e and 3d,e, the parts were cleaned in an ultrasonic bath for 10 minutes in water. Also before the film (1d, 2e) and the cover slip (5d,e) were added, the parts were ultrasonically cleaned, first in acetone and then in isopropyl alcohol (IPA), both for 5 minutes. Then they were dried using a regular nitrogen gun. These cleaning steps are omitted in the figure.

After bonding the cover slip to the slide, the piezoelectric transducer could be mounted. This was done by first gluing a piece of aluminum foil to the microscope slide using UV or cyanoacrylate glue to create a shared electrical ground. Then, the piezo disks were glued to this aluminum foil using silver conductive paste. Cyanoacrylate glue was added around the edges to strengthen the bond. A more elaborate guide can be found in Section 4.7. The 2D layout of the device is shown in Figure 4.8. An overview of the used materials is given in Table 4.3 in Section 4.7.

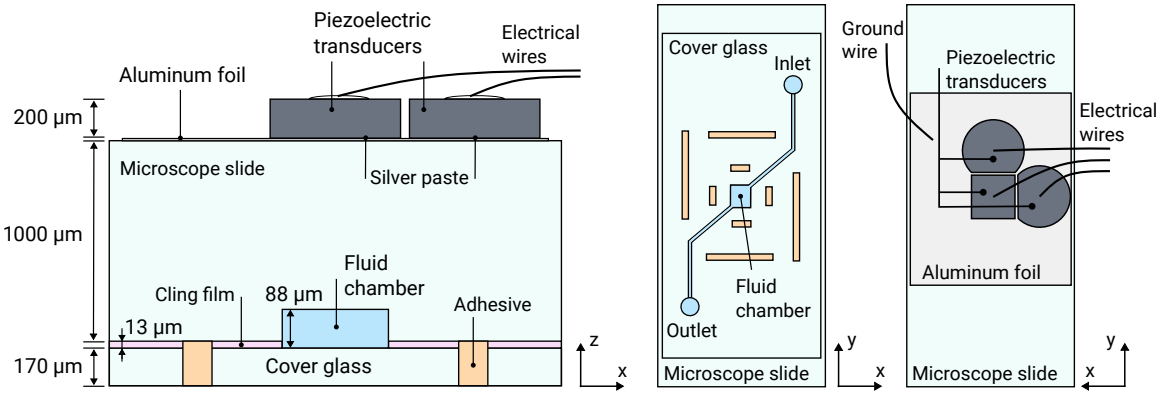


**Figure 4.8:** Schematic showing a cropped 2D layout (left) and the top and bottom of the chip.

### 4.3.1 Characterization

After fabrication, the dimensions, surface roughness and the frequency response of the chip were validated.

**Dimensions** A digital microscope (Keyence Digital Microscope VHX-6000) was used to determine the chamber dimensions and the surface roughness. In Figure 4.9a a top view of the fluidic chamber is given. The length and width were close to the desired values of 985 µm and 879 µm, respectively. This photo was taken prior to bonding the cover slip. The lines angled at 45 degrees around the fluid chamber are from the cling film. Figure 4.9b shows the chamber after the cover slip was bonded. It can be seen that the film adheres smoothly to the chamber's contours and the irregularities along the left and bottom wall were minor. In the top right, the edge of a small bubble is present. These bubbles were present over the whole surface and likely would have a negative effect as they form scattering boundaries. A 3D constructed image showing the height profile of one of the walls with the attached cling film is shown in Figure 4.10a. The average depth at the four walls was $96 \pm 1$ µm, exceeding the the goal of 88 µm.

For the surface roughness, the root mean square (RMS) height ($S_q$) was used. The roughness of the chamber floor and walls were 1.03 µm and 0.89 µm, respectively. This is close to the recommended roughness upper limit so scattering could be an issue. The expression for the RMS height roughness measure is explained in Section 4.7.

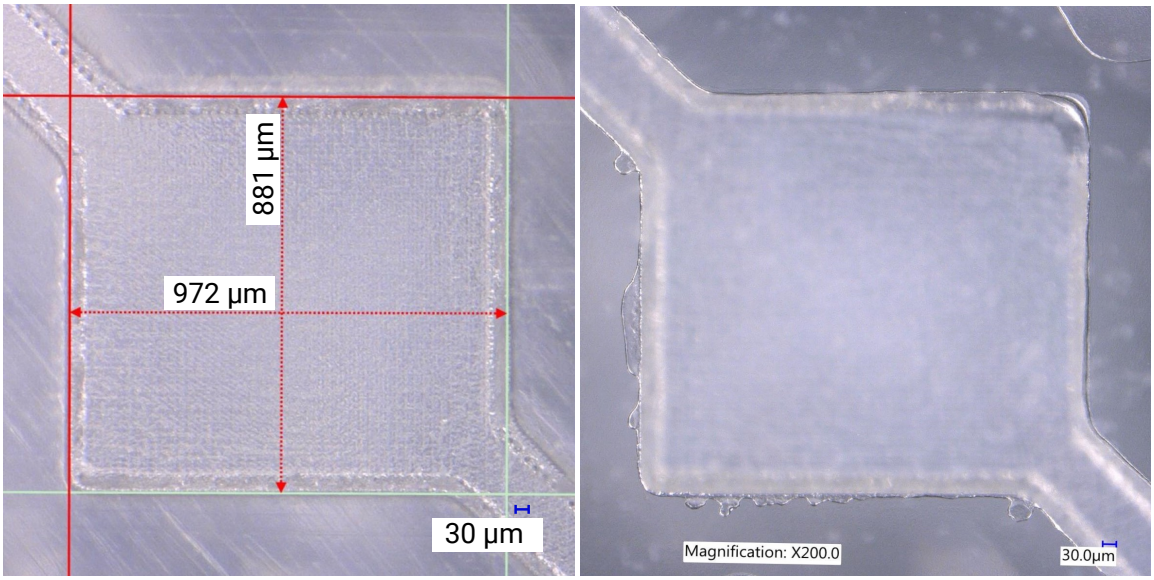


**(a)** **(b)**

**Figure 4.9: (a)** Top view of the chamber prior to bonding. The x- and y-dimensions are added using the Keyence software. **(b)** The same top view after bonding. The cling film provides a good seal, especially along the top and right edge.

**Frequency response** The frequency response of the device was acquired for three different media: air, ethanol and milli-Q. In these measurements the piezo directly underneath the chamber was actuated.

The results are shown in top the figure in Figure 4.11. Up to 6 MHz there is a strong decrease in impedance, which can be explained by the capacitive nature of the piezoelectric disk. Next to that, it is clear that the difference between the plots is quite minimal but that the fluid chamber filled with ethanol or milli-Q gives a slightly higher impedance compared to the air filled chamber for frequencies up to 8 MHz and slightly lower above that.

In the bottom figure of Figure 4.11 the experimental FRA result of the chamber filled with milli-Q is shown together with the theoretical predictions from the KLM model, with and without a 10 µm glue layer (NOA61) for the piezo connection. The overall shape of both curves is quite different, in part because the KLM model did not take the bonding layer into account. The resonance peak of the piezo at 10 MHz is however visible for all three curves. What stands out is the effect of including the glue layer of the piezo. This

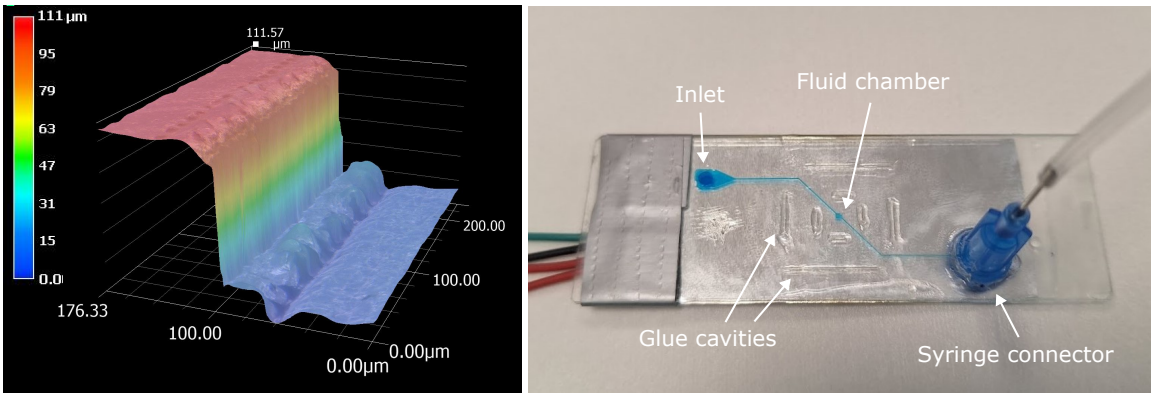


**(a)** **(b)**

**Figure 4.10:** **(a)** 3D view showing a wall profile of the chamber. The cling film is already attached in this image. The image was constructed with the depth profile function in the Keyence microscope software. **(b)** Photo of the fabricated device. Food coloring was used to highlight the channel. The blue syringe connector was added together with a silicone tube and a 1 mL syringe to be able to control the flow.

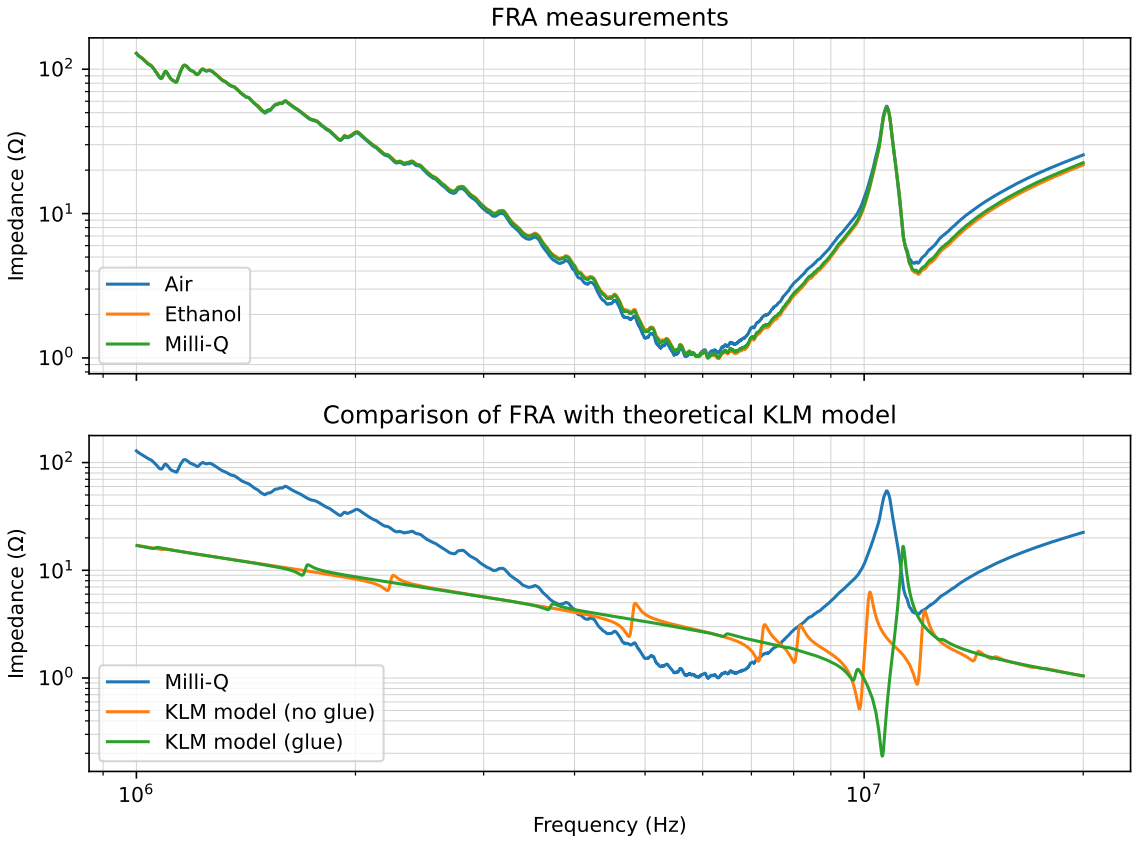


**Figure 4.11:** Frequency response analysis (FRA) results showing the measured impedance of the piezo over a frequency range. The top figure shows the effect of filling the fluid chamber with different media. The bottom figure shows the comparison between the experimental result of a milli-Q-filled chamber with the theoretically predicted impedance using the KLM model from Kamsma et al. [90].

significantly diminishes the resonance peaks seen in the yellow curve, in which the peak pairs at 7.21 MHz and 8.07 MHz correspond to half-wave resonances.

## 4.4 Bead patterning

Unfortunately, trapping the beads in the central chamber was not successful. When the system was actuated at one of the in-plane modes, the beads barely moved and did not end up in one of the pressure nodes, even when operating at a maximal peak-to-peak voltage of 40 V.

Even though patterning was not possible in the central chamber, it was successful to trap the beads in one of the input channels. The width of these channels were about 214 µm, which was about one fourth of the chamber width, so this increased the energy density. The beads could be trapped in lines in parallel with the channel and it was possible to switch between the full wave and half wave mode, where the wavelengths were equal or double the channel thickness, respectively. The employed frequencies were 6.93 MHz and 3.46 MHz, corresponding to wavelengths of 428 µm and 214 µm. This is shown in Figure 4.12

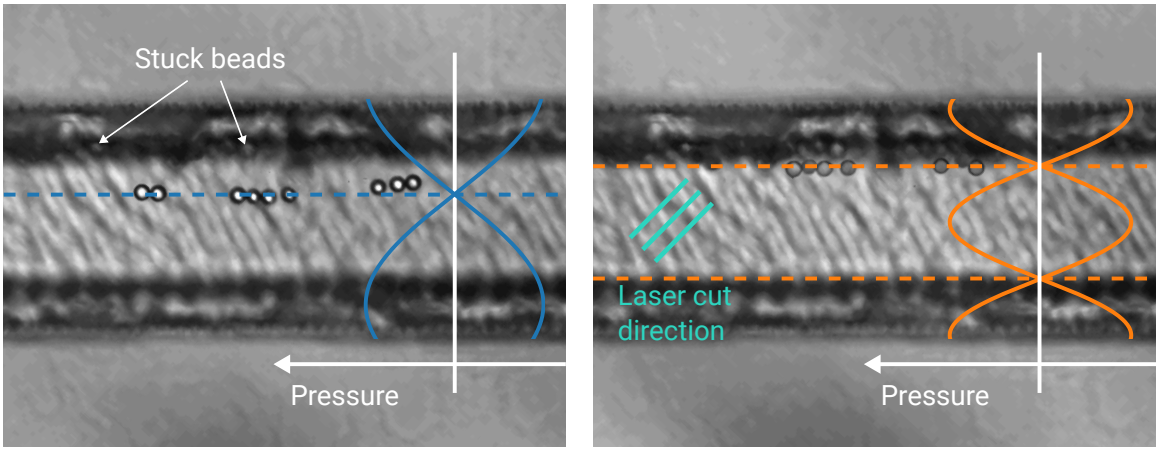


**Figure 4.12:** Microscope images showing that the particles gather in lines for the half-wave (left) and the full-wave (right) modes of the channel. In addition, the laser cut direction is highlighted. The appearance of the beads in the left and right photo differs due to a different out-of-plane position with respect to the focal plane.

The beads were clearly trapped in a line with some small deviations. Note however that the beads were slightly shifted for both modes. This indicates that the pressure nodes were not perfectly centered such that the anti-nodes did not coincide with the fluid boundary. Regarding the lines across the channel's bottom surface, they could not have come from the direction of laser cutting as shown in the figure. The two darker bands appear as the channel was deeper there, just like the trenches that were present in Figure 4.10a. Furthermore, many beads got stuck at the channel wall. Two examples are highlighted in the figure.

## 4.5 Force estimation

To estimate the strength of the horizontal trapping force in the channel, the trajectories of individual beads were analyzed. As the Reynolds number was small ($< 0.001$), viscous forces dominated over the particle's inertia. In addition, viscous drag from acoustic streaming was neglected as the polystyrene particles were much bigger than the critical diameter of 1 µm below which the Stokes drag is dominated by streaming [140]. In the sections below, the trajectories of the beads were analyzed for a half-wave and full-wave mode. The stiffnesses were obtained from fitting the trajectories to those from the equations of motions. This was fist done for the acoustic radiation force and later for a simplified, linear force.

The trajectory that was analyzed is shown in Figure 4.13. Here, the frequency was switched between a full and a half wave mode. The duration of each mode was set long enough to allow the beads to fully settle. On the left side (in blue) the particle moved from the pressure node of the full wave mode to the pressure node of the half wave mode. Shortly after, the particle moved back up under the force exerted by the full wave mode (in orange). A time axis has been included to show the relative duration of each trajectory. It is clear that the first trajectory was much faster than the second.

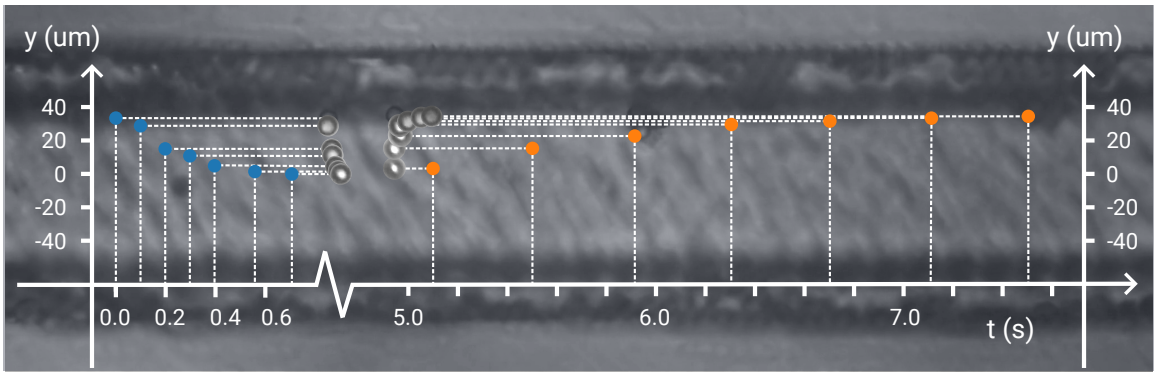


**Figure 4.13:** Overlay of the particle positions over time, showing the difference in particle speeds for a half-wave mode (blue) and a full-wave mode (orange).

### 4.5.1 Original sinusoidal force profile

First the trajectory was fitted based on the knowledge that the force profile of the ARF should be sinusoidal. For a particle suspended near a flat surface, a correction to the Stokes' drag force should be included to account for the altered interaction between the particle and the fluid near the surface. The corrected Stokes drag force then becomes:

$$\mathbf{F}_d' = -6\pi\eta a(\mathbf{v} - \mathbf{v}_\mathrm{p})\chi \tag{4.1}$$

which is the same expression as Equation (1.6) but multiplied by Faxén's correction factor $\chi$. As the particle was approximately suspended at half the channel height and the channel was about 95 µm deep, a correction factor of 1.18 was used [141]. Making up the force balance for the Stokes drag force and the primary radiation force formulated in Section 1.2 gave the following differential equation:

$$6\pi\eta a\chi\frac{\mathrm{d}y}{\mathrm{d}t} = 4\pi\Phi(\tilde{\kappa},\tilde{\rho})ka^3E_\mathrm{ac}\sin(2k_y y) \tag{4.2}$$

Barnkob et al. [142] provide the analytical expression for the solution:

$$y(t) = y_s + \frac{1}{k_y}\arctan\left(\tan\left[k_y y(0)\right]\exp\left[\frac{4\Phi}{9\eta\chi}(k_y a)^2 E_\mathrm{ac} t\right]\right) \tag{4.3}$$

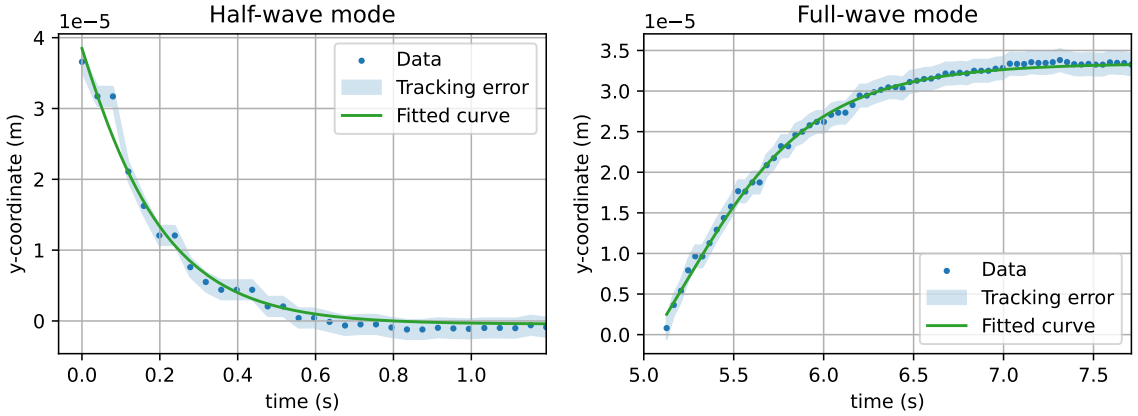


**Figure 4.14:** Trajectory of the beads under the force of a half-wave (left) and full-wave (mode). Both profiles are fitted with the solution from the equation of motion. The tracking error followed from the tracking calibration measurement.

The fitting parameters were the acoustic energy $E_\mathrm{ac}$, an artificial offset $y_s$ and the starting position $y(0)$. The first trajectory was driven by the half-wave mode For the first trajectory the fit gave an acoustic energy of $(4.01 \pm 0.19)$ J/m$^3$. Fitting the second trajectory resulted in an acoustic energy of $(0.391 \pm 0.034)$ J/m$^3$.

From the force profile, the stiffness could be calculated using:

$$F(y) = \frac{4}{3} k_y \pi a^3 \Phi E_{\mathrm{ac}} \sin(2k_y y) \tag{4.4}$$

$$k = \frac{\mathrm{d}F}{\mathrm{d}y} = \frac{8}{3} k_y^2 \pi a^3 \Phi E_{\mathrm{ac}} \cos(2k_y y) \tag{4.5}$$

This resulted in a half-wave stiffness of $(1.003 \pm 0.055)$ pN µm$^{-1}$ and a full-wave stiffness of $(0.375 \pm 0.043)$ pN µm$^{-1}$.

### 4.5.2 Simplified linear force profile

The trajectory could also be analyzed by simplifying the equation of motion to a force balance with a linear acoustic radiation force. The following equation of motion was used, where the inertia was again neglected:

$$-\gamma \frac{\mathrm{d}y}{\mathrm{d}t} - k_i y(t) = k_i y_{\mathrm{f}} \tag{4.6}$$

In this equation, $y$ is the position of the particle (in m), $\gamma$ the viscous drag coefficient (in kg s$^{-1}$) and $k_i$ is the trap stiffness of mode $i$ (in N m$^{-1}$). The equation was written such that the bead's end position $y_{\mathrm{f}}$ also appeared, which would be convenient for fitting the trajectory later on. Solving this differential equation gave the following expression for the position, in which the time constant $\tau$ could be defined as $\gamma/k_i$:

$$y(t) = y_{\mathrm{f}} + (y_0 - y_{\mathrm{f}}) e^{-\frac{t}{\tau}} \tag{4.7}$$

Figure 4.15 shows the result of fitting these paths with the expression found in Equation (4.7). The obtained time constants were $196 \pm 9$ ms and $558 \pm 7$ ms The tracking accuracy is added as the shaded area. Both trajectories fitted well to a path predicted by the assumed linear force, especially in the right plot where the bead moved much slower. The flat parts in the left figure come from video acquisition lag such that some frames were duplicates.

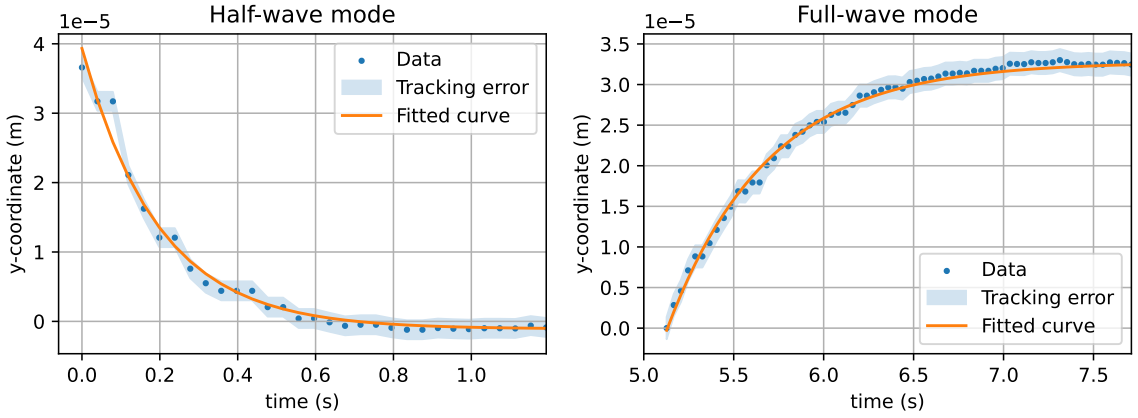


**Figure 4.15:** Particle trajectories as a result of switching from a half-wave mode to a full-wave mode (left) and vice versa (right). The trajectories were fitted to the solution of a simplified, linear equation of motion in Equation (4.7).

With the time constant, the linear stiffness could be determined assuming that the drag force coefficient $\gamma$ was known. The following expression was then used to calculate the stiffness.

$$k_i = \frac{\gamma}{\tau} = \frac{6\pi\eta a \chi}{\tau} \tag{4.8}$$

which gave a stiffness of $(0.853 \pm 0.097)$ pN µm$^{-1}$ and $(0.299 \pm 0.031)$ pN µm$^{-1}$ for the half wave and full wave mode respectively. These uncertainties comprise the fitting error for $\gamma$, an uncertainty on the radius of ±0.2 µm (as specified by the manufacturer) and the spread in the dynamic viscosity due to a ±10 °C temperature error of ±0.1 mPa s.

## 4.6 Bead manipulation

In this section, the results of mode-switching are presented. Mode-switching took place between the half wave and full wave mode as these modes did not share pressure nodes, causing all the beads to move when the frequency was switched. First, it was established that a switching frequency of 100 Hz was suitable. This frequency was high enough such that the beads no longer appeared to oscillate and low enough that the standing wave still had sufficient time to reach its final amplitude, which was in the order of tens of microseconds [8]. Over a range of time ratios, the particle locations were tracked. Then, only the $y$-position (as defined in Figure 4.13) that were within a window of 100 µm along the channel were saved. The reason for this was that the pressure field was not homogeneous along the channel. A periodicity could be observed which was likely to come from a transversal resonance. The result is shown in Figure 4.16.

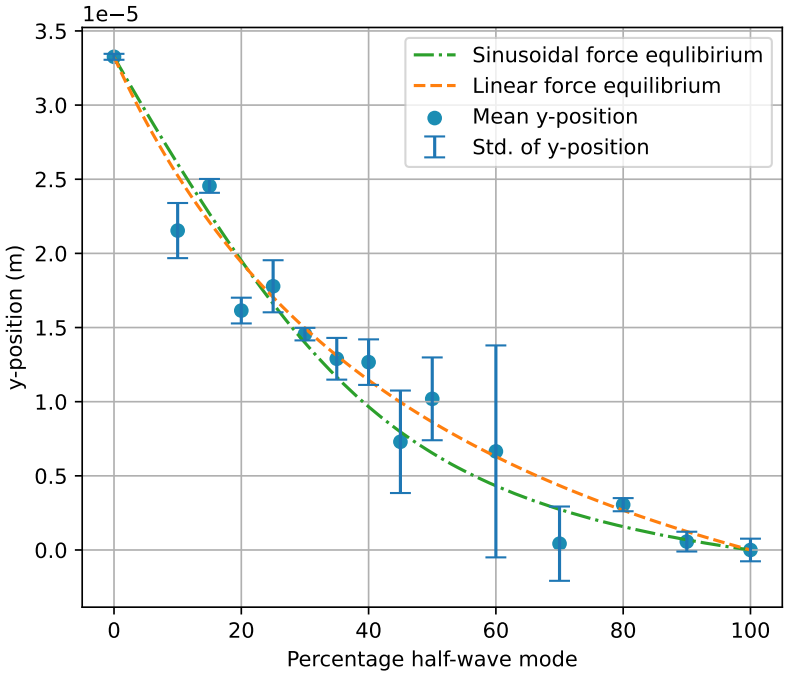


**Figure 4.16:** Result of mode-switching between a full wave and half wave mode. The green line represents the predicted equilibrium when the forces of both modes are assumed to be sinusoidal, as expected from the acoustic radiation force. The orange line represents the same but then for a force profile that is linear.

It is clear that the bead moved toward the half-wave pressure nodes as the ratio of the activation of that mode increased. The large uncertainties for some positions were the result of beads that relatively moved more along the channel. In the plot, also the prediction of the equilibrium positions from a linear and more realistic sinusoidal profile is added. How these curves were obtained is depicted in Figure 4.17.

The left two figures show the combined force for a range of mode ratios. In the right two figures, the equilibrium positions were added as dots. These were the locations where the force was zero and the stiffness was positive. The half-wave mode (ratio 100:0) had an equilibrium in 0 m and the full-wave mode profile (ratio 0:100) was shifted such its equilibrium coincided with the observed shift from the experiment. It is clear that this shift is smaller than half a wavelength, which one would expect in the ideal case when the anti-nodes are located at the walls. The right two figures display the equilibrium position with respect to the mode-switch ratios. Notably, the two graphs are very similar.

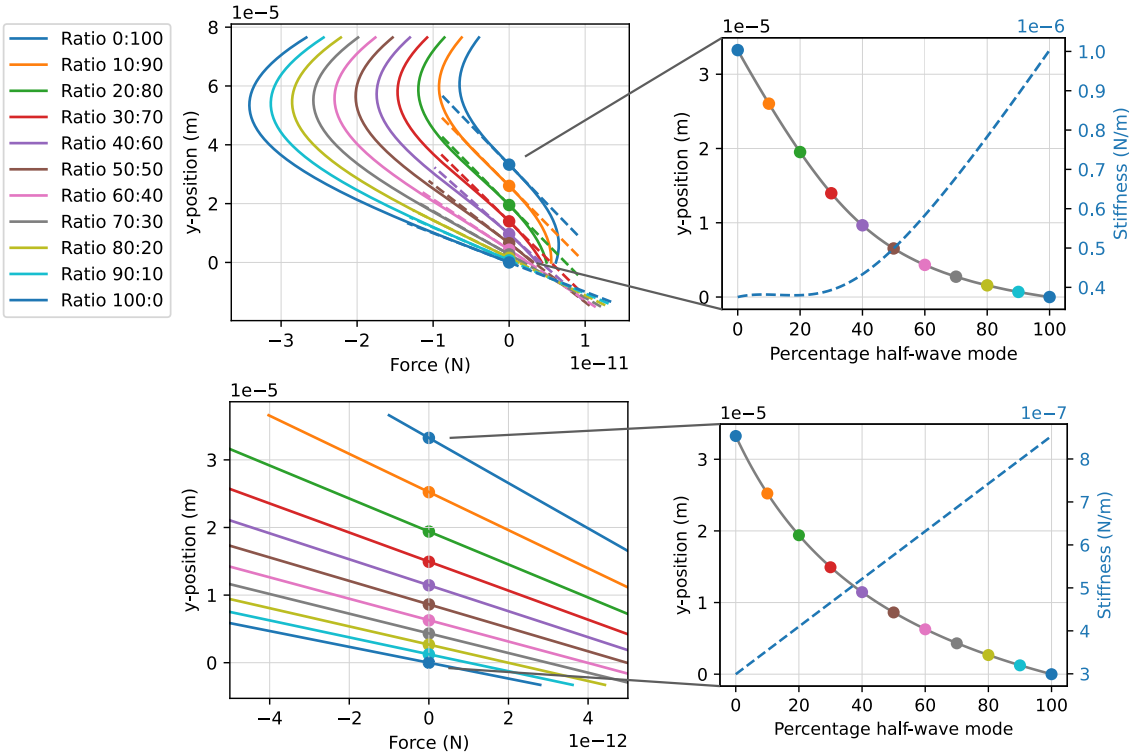


**Figure 4.17:** Figures showing the equilibrium positions for the particle when sinusoidal force profiles are assumed (top) and when the forces are assumed linear (bottom).

# Discussion

In Chapter 4 we showed that it was possible to fabricate a device capable of trapping and manipulating beads mostly from standard lab gear. Finite element studies revealed the critical role of thin adhesive layers in generating strong pressure fields. The fabrication process was described, proving that a simple bond using cling film and cyanoacrylate glue was achievable. Although bead trapping in the central chamber was unsuccessful, effective trapping and manipulation was realized in one of its input channels, demonstrating its potential in manipulating micro-scale particles. Below the results are interpreted and discussed further.

**FEM** From the finite element analysis it became clear that a thin adhesive layer is beneficial for attaining a strong pressure field in the vertical and in-plane direction. The results of the vertical field showed that the third configuration achieved higher pressures though the variation over the frequency range was also higher. The lower chamber height could be reason for the higher pressure as Kamsma et al. [90] showed in their KLM parameter sweep. Their analysis also showed that this decrease is not monotonic, which could explain why the difference between configuration 1 and 2 is quite small even though the chamber height of the latter is much larger. It is likely that the thinner adhesive also played a role here. As the damping of these adhesive materials are higher than the surrounding glass, a thicker adhesive layer will also result in more energy loss. This could also explain the larger variation in the gradient peaks as a lower damping gives rise to more pronounced resonances.

Also for the in-plane field simulation configuration 3 performed better than the other two, both in terms of field strength and uniformity. A likely explanation for the stronger field is that only for this configuration, the chamber wall surface mostly exists of glass, whereas for the other two this is Kapton tape. The acoustic impedance mismatch between the water and the glass is higher than for the water and tape, resulting in a reflection coefficient of about 0.81 for a water-glass boundary and 0.22 for water-tape. The plot for the standard deviation of the gradient peaks shows that configuration 3 still performs best. What is striking is that the second configuration showed more in-homogeneity than the other two. It is plausible that the transition of the wall material from glass to tape approximately halfway the chamber height played a role here. Analyzing the overall distribution of the pressure field provided some insight.

Figure 4.18 shows one of the strongest and most homogeneous pressure fields that were obtained for configuration 2 and 3, in which he adhesive layer is highlighted in orange. Apart from the chamber height, the main difference is that for configuration 2, the transition from tape to glass is about halfway the chamber height. It is likely that this causes the pressure field to be distorted at both walls, much more than in configuration 3. As a result, the nodal line is split and shows a bend in each corner of the fluid chamber.

It should be noted that the FEM analysis were only used to make a comparison between the device layouts. As the results were not validated experimentally, the absolute values of the simulated pressure fields should be ignored.

**Fabrication** Fabricating the device was much harder than expected and it took several iterations before we obtained a working device.

Laser cutting proved to be a quick way to form the fluid channel as this did not cost more than two hours in total for one device. There were however also a few downsides to this technique. First of all, it was difficult to obtain the desired channel depth, as is apparent from the depth discrepancy of the device. One likely cause is the initial calibration of the laser. The focal point was set to the top of the glass surface but due to the transparency, a marker was needed to find this surface. Moreover, calibrating the height was done manually by looking at how sharp the image appeared. Next to the deviation in channel depth, the 3D image in Figure 4.10a also shows that there is a trench of about 10 µm right next to the wall. The reason this appears is not entirely clear but it is likely the cause of one of the laser parameters. This is discussed further in Section 4.7.

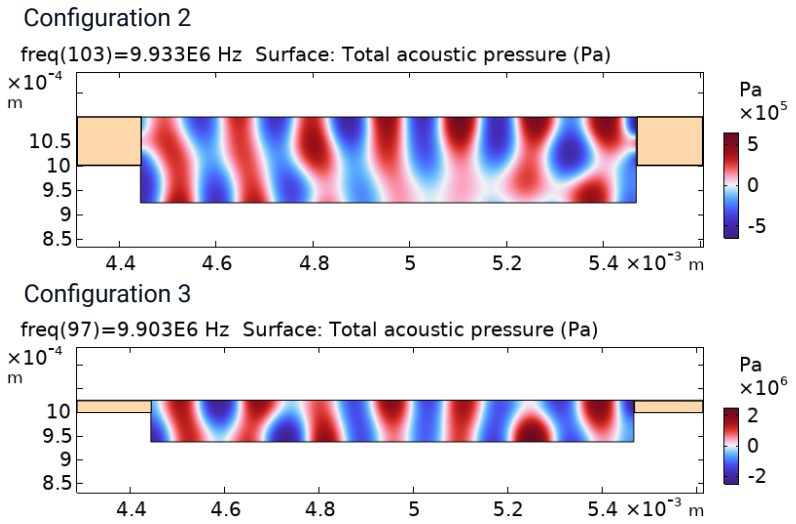


**Figure 4.18:** Qualitative comparison of one of the best pressure fields for configuration 2 (top) and configuration 3 (bottom). The adhesive layer is marked in orange. It can be seen that the field strength in configuration 2 is much lower.

**Bead patterning** There might be several reasons why trapping the beads in-plane was only possible in the thinner channel and not in the main chamber. As the standing wave would be created by creating reflections between the channel walls, the properties of these walls could be one of the issues. Key to the formation of effective 'acoustic mirrors' are two properties: the reflection coefficient and the surface roughness. The reflection coefficient, especially at the glass-water interface, is less likely to be a major factor as it is already rather high, approximately 0.8. The surface roughness governs the amount of scattering and should be as low as possible. The RMS roughness of the bottom surface and walls, measured at around 1 micron, is in the order of the maximum recommended roughness [127]. In contrast, Evander et al. [143], utilized a glass microchannel 375 microns wide, which seems to have a significantly higher surface roughness than our chip (based on Fig. 4b). Furthermore, their channel, produced through wet-etching, had wall profiles tilted at about 45 degrees. This implies that the surface roughness and also the general wall topography are unlikely to be the sole reasons for the lack of acoustic pressures.

Another factor that is known to be important in BAW devices is the type of bonding. Both the bond of the cover slip and the piezoelectric disk need to be considered. The former mainly affects the transversal trapping performance of the chip. This is because it is known that for transversal resonators, the resonance of the chip as a whole is important and that a bonding material with high losses attenuates this resonance [144]. In our device, the bonding layer consisted of polyethylene cling film. Even though the thickness was low (around 13 µm), it was probably an important factor in reducing the device's resonances. The bonding of the piezo is the second key part of the device. This bond consisted of two layers: a UV glue (acrylic) bond between the aluminum foil and the slide, and the cyanoacrylate bond with the piezo. Even though these adhesives are relatively hard, the glue has a detrimental effect on layered resonator devices and should be as thin as possible [127, 145]. In addition, heating of the device during operation weakens the bond [79] but also when the device was still relatively cool, in-plane trapping was not possible so this was probably no issue.

A third impeding factor might be the size of the fluid chamber. In literature, transversal resonators commonly have fluid channels of a few hundred microns [142, 146, 147], whereas our fluidic chamber was about 1 mm in both directions. This means that the acoustic energy that enters the chamber is shared by a larger area which decreases the energy density. This in turn reduces the acoustic radiation force.

The fact that beads often stuck to the surface and to other beads was an additional problem. No additives like Tween20 [142] or casein [90] were used which caused the beads to become stuck to the channel walls. They were also difficult to wash out. On the other hand, this accumulation also occurred in the channel so it is unlikely to be a critical factor.

**FRA** From Figure 4.11 it is clear that the difference in frequency response for different media was minimal. Up until 6 MHz there were clear resonance peaks visible. The goal was however to identify the fluid resonance by analyzing the response of different media, but this difference was minimal. One reason that the results

were so similar could be that the area of the fluid chamber was quite small compared to the surface area of the piezo. The surface ratio was only 1 to 58. This means that only fraction of the energy from the piezo entered the chambers and even less got coupled back and affected the measurement, resulting in low coupling. Setups in literature commonly have wider flow channels that stretch over the entire surface [8], which increases the coupling. Additionally, as trapping in the vertical directed was quite difficult (the majority of the beads did not move) the fluid resonances were already rather weak.

The comparison with the KLM model shows that the adhesive layer has a significant effect on attenuating the resonance peaks. In the measured impedance, however, a series of resonance peaks appeared up to 6 MHz. These are therefore probably the result of stronger, structural resonances from the device and the piezo.

**Force estimation** By fitting the trajectories using the knowledge of equation of motion, it was possible to extract the acoustic energy.

Overall, fitting using the more realistic, sinusoidal ARF in Equation (4.3) required careful tuning of parameters using the knowledge on the starting positions that could be determined. Unlike Barnkob et al. [142] that were able to fit both the wave number and the acoustic energy, this resulted in a large spread in the parameters for the half-wave mode trajectory. The number of data points for each trajectory played a role here as the spread was not as large for the second, slower trajectory which contained more data points.

Fitting the trajectories with a linear profile was more straightforward in comparison. The stiffnesses showed a smaller uncertainty range but was overall somewhat lower. Partly the fact that a linear force was assumed could explain this discrepancy. The stiffness that was calculated with the more realistic equation corresponds to the local stiffness in the node whereas the linear force assumes a constant, average stiffness. To make a better comparison, a correction could be made to the linear profile based on the work produced by each force.

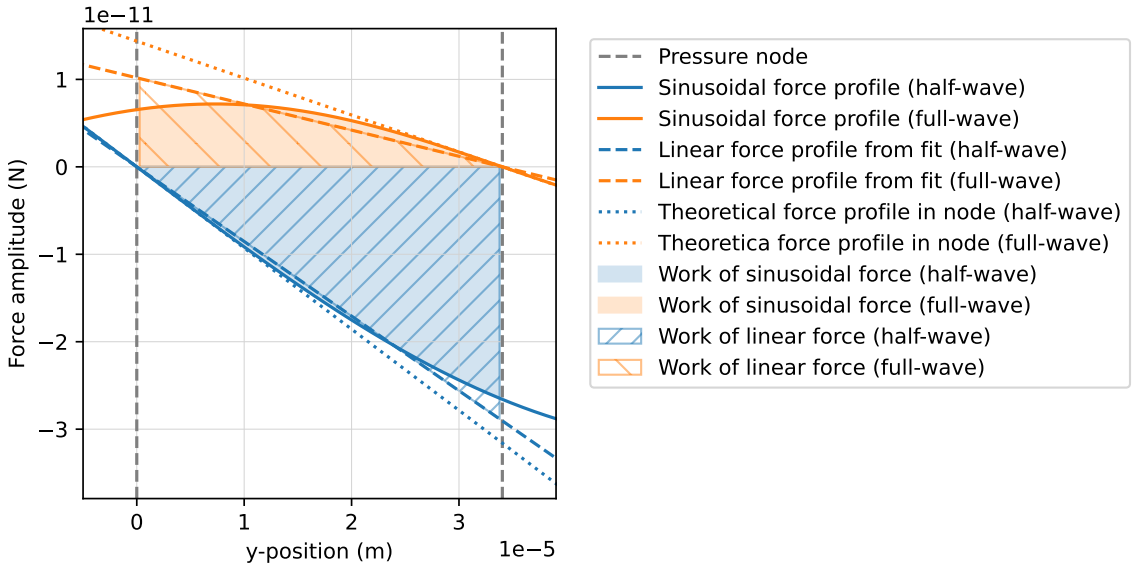


**Figure 4.19:** Figure showing the force profiles of the true, sinusoidal acoustic radiation force and a linearized simplification. The theoretical work on the polystyrene bead produced by each force corresponds to the area under each curve. The local stiffness in each node was calculated by setting the work of both profiles equal to each other.

The work is a measure for the amount of energy added or removed from an object over a certain displacement and is defined as follows:

$$W = \int_C F\,ds \tag{4.9}$$

where $C$ denotes the trajectory, $F$ is the force and $s$ is the displacement along the force. In the force-position plot in Figure 4.19 this corresponds to the shaded and hatched areas under the force curves. The work of the theoretical, sinusoidal profile ($W_{\text{sin}}$) and the linear profile ($W_{\text{lin}}$) should be equal as the trajectories

were also equal. Hence, the amplitude of the sinusoidal profile can be determined by setting both integrals equal to each other. The work of the linear force is as follows:

$$F_{\text{lin}} = -k(y - y_{\text{n}}) \tag{4.10}$$

$$W_{\text{lin}} = \int_a^b -k(y - y_{\text{n}})\, dy = -\frac{1}{2}ky^2 + ky_{\text{n}}y \Big|_a^b \tag{4.11}$$

where $y_{\text{n}}$ denotes the position of the node. A general sinusoidal profile gives:

$$F_{\text{sin}} = -A\sin(k_y(y - y_{\text{n}})) \tag{4.12}$$

$$W_{\text{sin}} = \int_a^b -A\sin(k_y(y - y_{\text{n}}))\, dy = \frac{A}{k_y}\cos(k_y(y - y_{\text{n}})) \Big|_a^b \tag{4.13}$$

Setting the work of both profiles equal and solving for amplitude $A$ allowed us to calculate the stiffness in the nodes. These adjusted stiffness of the half- and full-wave that followed respectively were $0.928 \pm 0.106$ pN µm$^{-1}$ and $0.422 \pm 0.044$ pN µm$^{-1}$. As can also be seen in Figure 4.19 the stiffness in the nodes are 9% and 41% larger than the average stiffness. They are thereby closer to the ones found from the non-linear fit (respectively $(1.003 \pm 0.055)$ pN µm$^{-1}$ and $(0.375 \pm 0.043)$ pN µm$^{-1}$). This gives us more confidence that the obtained acoustic energy density of the half-wave mode is also a reasonable indication. It is then comparable to the value found in Barnkob et al. [142] (6.69 J/m$^3$), albeit at a much higher peak-to-peak driving voltage (1.52 V while we used 38 V).

Overall, this method was fast and especially well-suited for estimating the stiffness for larger beads. Kamsma et al. [90] showed they were able to accurately map the force profile by tracking the velocity. One limitation of this method is however that a sufficient frame rate of the camera is needed. When larger beads are used, the ARF grows and the time response decreases. As the beads move faster, the number of data points for a trajectory reduces which can results in a more erratic velocity-, and subsequently force-, profile for lower frame rates. In addition, this approach is not as sensitive to localization errors as for example the equipartition method.

**Bead manipulation** From Figure 4.16 a clear relation between the mode-switch ratio and the bead position was visible. Furthermore, the predicted equilibrium positions for the true sinusoidal force profile and the simplified linear one both showed good agreement with the experimental data. In contrast with the expected profile when both modes are in phase or anti-phase (as was visualized in Figure 3.7a), the curve shows no steep drop toward the pressure node of the half-wave mode. The effect of this relative shift of both modes was depicted earlier in Figure 4.17. In case the acoustic fields are more aligned and this steep drop is present, our method could then be employed to shape the equilibria positions by adjusting the input power for each mode.

# Conclusion

This study aimed to realize a bulk acoustic wave device capable of trapping microbeads, constraining them in all three dimensions. The project was divided into two subquestions:

1. *How can a bulk acoustic wave device consistently arrange particles in pattern where each potential well holds one particle?*

2. *How can the interparticle distance of the microbeads in the 2D pattern be controlled in a bulk acoustic wave device?*

Regarding the first question, it was unfortunately not possible to create a grid of isolated particles in our device. The chip was made of glass and by avoiding more complex bonding methods like anodic bonding, the scope was narrowed down to the use of adhesives. Although these are cheap and widely available, they do introduce significant damping and it is difficult to obtain a thin and strong bond while preventing clogging of the channel. From our finite element simulations, it was clear that the minimizing the thickness of the adhesive increased the field strength and also enhanced the homogeneity for the in-plane field. Therefore, finding a better way of producing a glue-based device was the initial focus. Employing a mix of cling film and cyanoacrylate glue successfully reduced the adhesive thickness to just 13 µm. The cling film provided a hermetic seal and the glue was added through openings in the cover slip to secure the bond. Despite the thin bonding layer, the trapping efficacy in the vertical direction was limited and no trapping was observed in-plane. The low energy density was likely due to energy losses in all bonding layers. Together with the aberrations in the wall profile from the femtosecond laser and a non-negligible surface roughness, the field strength and quality would be further reduced.

Even though bead patterning was not achieved, it was possible to create a 2D trap in the channels connecting the chamber to the fluid inlet. It is likely that this was mainly enabled by the smaller width. It was shown that the stiffness could be approximated by fitting the trajectory with the knowledge of the relevant forces. This approach was fast and, compared to techniques like the equipartition method, the tracking precision and camera frame rate were less critical. These trajectories were obtained by extending the functionality of the TrackPy package in Python. The radial variance transform algorithm was implemented to increase tracking accuracy while still benefiting from the trajectory linking functionalities of TrackPy. Both the true equation of motion with a the sinusoidal acoustic radiation force as well as a simplified, linear version could be used. For the latter, it was shown that a correction to linearized stiffness could be made to attain an approximation of the local stiffness in the node. This was done by taking the work produced by each force into account. For the half-wave and full-wave mode, acoustic energy densities of 4.01 J/m$^3$ and 0.391 J/m$^3$ were achieved. Furthermore, mode-switching proved to be successful and showed good correspondence with the predicted equilibria.

This research has shown the possibility of trapping and manipulating microparticles in-plane using a simple device that mainly comprises standard lab items. The faster and simpler fabrication method might facilitate a lower barrier for a more widespread adoption in biomedical scenarios, for instance in cell adhesion studies and tissue engineering applications like organ-on-chip devices. Furthermore, the ability to accurately predict the trapping positions using a simple analysis on the stiffness could make the control of these devices easier. This could for example facilitate the design of force- or distance-clamps in single-molecule or in other applications where dynamic fields are needed such as in microfluidic flow-free transport.

## 4.7 Recommendations

In this sections, several recommendations are presented based on the findings from our research.

**Fabrication** One improvement that would be valuable is finding a better way of bonding the cover slip to the microscope slide as this would increase the field strength. When the channel is created using a femtosecond laser, glass-welding could also be possible, which circumvents the need for high-loss adhesives. Kim et al [148] demonstrated this maskless and fast bonding technique whereby the glass is locally melted. They showed that the a bond strength of 1.4 MPa was possible, which is on par with a UV glued bond.

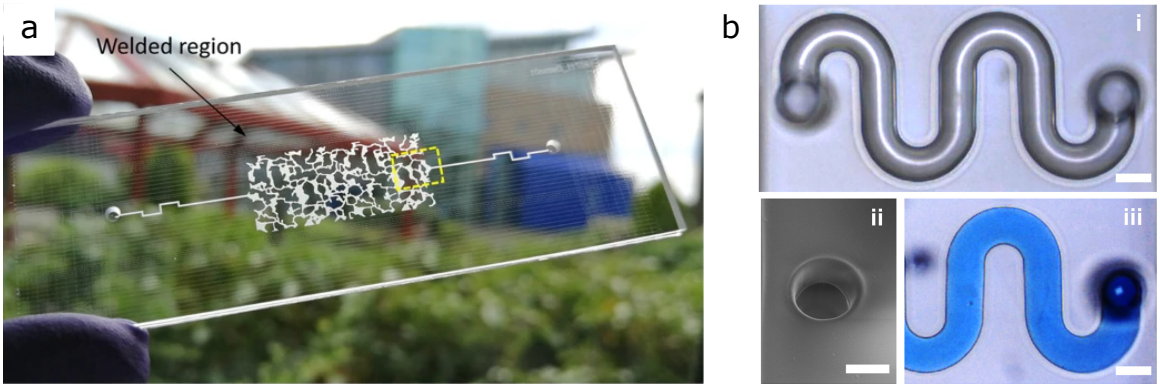


**Figure 4.20: (a)** Photo from Wlodarczyk et al. [149] showing a glass-welded chip. The weld lines surround the chamber in parallel lines. **(b)** Images from Li et al. [150] of a printed microfluidic channel in silica-glass (30 µm scale bars).

Next to that, fabrication by 3D printing could provide more design freedom in the future. Current polymer based printing could work as Moiseyenko et al. [75] showed in their model that PMMA could also provide good acoustophoresis comparable to silicon-glass devices when whole-system resonances are adopted. Furthermore, as the technology advances and the list of available materials grows, printing of lower-loss materials could also have the potential to be adopted in acoustofluidics. Recently, Li et al [150] demonstrated they could make glass structures with photochemistry in less extreme conditions than before. The high resolution and low surface roughness enabled fabricating tiny microlenses and a small microfluidic channel. This channel is shown in Figure 4.20b.

**Characterization** As the coupling was too low, the resonances could not be found using a frequency response analysis. Instead, the the optimal actuation frequency could be found during operation by tracking the response of the bead. Rapidly switching between two modes while gradually changing the frequency of one mode could work as the bead will move more toward the equilibrium position of that mode as the acoustic pressures increases. The frequency with the largest displacement then indicates the strongest resonance.

**Operation** When the modes are in phase (or anti-phase), it was shown that the equilibrium positions during mode-switching show a steep descent. This means that the position changes rapidly over a small range of switching ratios, which reduces the positioning accuracy. With the knowledge of the strengths of each mode, one could try to tweak the actuation voltages and activate more modes to alleviate this. One method that could be employed is based on the proposal of Courtney [106]. He proposed a method in which the trap stiffness could be increased by superimposing several modes. The respective voltages were determined by applying a Fourier series on a certain profile, in his case a square wave to achieve a flatter force profile with a high stiffness in the trap. This approach could be extended to allow for a better controllable equilibrium.

**Applications** There are several applications for which our research could be used. First of all, regarding force spectroscopy, being able to control the position of the bead allows to form a distance clamp where the bead's location is kept constant. This mode of operation has been used to study overstretching double-stranded DNA [90]. In addition, if the force profile could be accurately shaped, a force clamp could also be realized. A force clamp works by keeping the force on the sample constant by adjusting the beads position using active feedback, which has been used to study RNA polymerase activity [151, 152]. Furthermore, acoustic manipulation could be used for force spectroscopy indirectly. This was shown by Nava et al. [153] where an optical stretcher was assisted by an acoustic trap as an easy method to prefocus the cells.

# Appendices

## Appendix A: Microfluidic chip fabrication

### A.1 Design orientation

The design scope was narrowed down based on the best performing devices found in literature. These could broadly be grouped as: side-actuation, where the chip is actuated by transducers located on the sides; chamber-wall-actuation, where the transducers are placed against the chamber walls; non-parallel-actuation, where the direction of excitation is not the same as that of the desired wave field; and actuation using strip electrodes, where one transducer is used to create wave fields in multiple directions. An overview of the relative strengths and weaknesses of each configuration is given in Table 4.2. This comparison is qualitative rather than quantitative as the variation in performance of a device depends to a large extent on the chosen dimensions [90].

**Table 4.2:** Comparison of most promising piezoelectric transducer configurations. The transducers are marked in red in the figures. The colors indicate a relative range from advantages (green) to disadvantages (red), where yellow indicates no preference.

| Type of actuation: | **Parallel, side actuation** | **Parallel, chamber wall actuation** | **Non-parallel, wedge actuation** | **Non-parallel, strip-electrode** |
|---|---|---|---|---|
| | 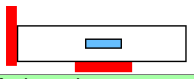 |  | 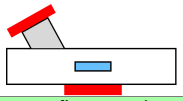 | 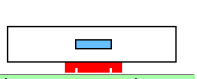 |
| Ease of fabrication | Moderately easy to mount transducers to the side (due to small thickness) and simple connection of electrodes. | Hard to mount and align transducers for small fluid chamber heights. | Easy to fix transducers to the chip and to connect electrodes. | Only one transducer is needed. Making cuts for separate electrodes is straightforward. |
| Materials | Material choice limited to hard materials with high acoustic impedance. | Also softer materials with higher damping can be used. | Material choice limited to hard materials with high acoustic impedance. | Material choice limited to hard materials with high acoustic impedance. |
| Piezo placement | Limited to the sides of the chip. | Limited to the chamber walls, so heating can become an issue. | More flexible, not fixed as long as the correct modes can be excited. | Irrelevant as no additional piezo is needed. |
| Force field | Fluid chamber can be small, resulting in higher forces. | Fluid chamber height is determined by transducer dimensions. | Fluid chamber can be small, resulting in higher forces. | Fluid chamber can be small though strength of the field is likely to be lower as the piezo acts as both a planar and a transversal resonator. |

### A.2 Materials

A list of all the materials used for the three prototypes is given in Table 4.3.

**Table 4.3:** Overview of the materials needed to build the acoustofluidic chip.

| Name | Specifications | Number | Cost per unit | Total cost | Source |
|---|---|---|---|---|---|
| Glass microscope slide (631-1553) | 76x26x1 mm (l x b x h) | 1 | €0.10 | €0.10 | Avantor [154] |
| Glass cover slip (631-0853) | 60x24 mm (l x b ); #1.5 thickness; pre-washed pure white Hydrolytic Class 1 glass | 1 | €0.09 | €0.09 | VWR [154] |
| Piezoelectric transducer PRYY+1119 | PIC255; $d = 10\,\text{mm}$, $t = 0.2\,\text{mm}$ | 3 | €8 | €24 | Physik Instrumente [119] |
| Silver conductive paste | - | 1 | €22.91 | €0.30 | Farnell |
| Double-sided tape | Double-sided tape lucid for optical applications | 1 | €18.00 | €0.05 | Zeiss [155] |
| Cling film | - | 1 | €1.00 | €0.01 | Any grocery store |
| UV-curable glue | KRYLEX KU503, 50G | 1 | €39.98 | €39.98 | Farnell [156] |
| Cyanoacrylate glue | Superglue by Handson was used | 1 | €4.29 | €0.10 | Any grocery store |

## A.3 Laser cutting

**Parameters** An overview of the adopted laser cutting parameters for the LASEA femtosecond laser cutter is given in Table 4.4

**Table 4.4:** Overview of the laser cutting parameters that were used for the final prototype (configuration 3).

| Parameter | unit | value |
|---|---|---|
| Speed | $\text{mm}\,\text{s}^{-1}$ | 200 |
| Repetitions | - | 100 |
| Power | % | 50 |
| Pulse rate | Hz | 15003 |
| Hatch profile | - | vertical |
| Hatch pitch | mm | 0.01 |
| Outlines | - | 1 |
| Outline separation | mm | 0.01 |

**Wall profile** Ideally, the fluid chamber walls should be perfectly straight and vertical. It was however noticed that, often, there would be a trench next to the wall. To find out what caused this issue, several different hatch profiles were tested on a square profile: vertical, horizontal, angled at 45°, the erode pattern (the area is then filled with its contours), first half vertical / second half horizontal, and vertical and horizontal in an alternating manner. However, none of these settings solved the issue completely. For the horizontal and vertical sweeps, the trench was most prominent at the side from which the sweep starts and ends. The angled sweep gave a somewhat lower trench. The erode sweep gave the cleanest profile though there appeared trenches in the central part where the contour profile had its edges. Alternating the vertical and horizontal profiles also gave reasonable results. Taken together, no conclusion could be made on the best hatch as there were also variations over different cavity dimensions.

**Surface roughness** To quantify the surface roughness, the root mean square height is an often used measure. This is defined as follows:

$$S_q = \sqrt{\frac{1}{A}\iint_A [z(x,y) - \bar{z}]^2 \, dx\, dy} \tag{4.14}$$

Here, $z(x,y)$ is the local height, $\bar{z}$ the mean height, and $A$ the evaluated surface. The illustration in Figure 4.21 shows the definition for a line profile.

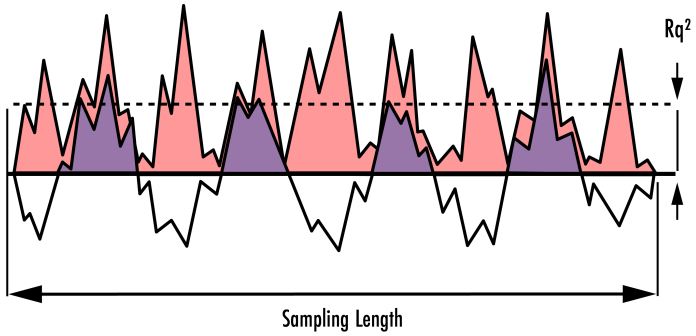


**Figure 4.21:** Schematic from Edmund Optics [157] showing the meaning of the root mean square (RMS) height for a line profile. This measure was used to quantify the surface roughness of the chamber floor and walls.

Lastly, there are some general aspects about operating the Lasea femotosecond laser cutter to keep in mind. First of all, the laser focal point is calibrated by adjusting the height based on the camera view. To find the top surface of the glass slide, a marker can be used. In addition, the cutting range of the laser is limited to a range of about 30 mm, outside of which the drawing will get heavily distorted. The split function can be used to cut up the drawing into smaller parts. For engraving the slide, an overlap of at least 0.05 mm is recommended as otherwise not enough material might be cut away which will result in a blocked channel. Alternatively, in the case of an overlap in smaller features like a channel, a scalpel can be used to cut away the remaining obstructions.

## A.4 Bonding

The hardest part of the fabrication process was to find a way to create a bond that was both strong and leak-tight. Below a summary of all techniques that were tried are described.

**Configuration 1 and 2** An overview of the fabrication of the devices with configuration 1 and 2 can be seen in Figure 4.22.

The devices labelled *c* and *d* are bonded by double-sided optical tape. The use of double-sided tape circumvents the problem of clogging the channel when using glue but comes at the cost of a weaker bond and a restriction on the fluidic chamber height. The tape thickness defines the minimum height, limiting the design freedom and thereby optimal parameter combination.

**UV gluing with tape spacer** One method consisted of simply covering the surface of the slide with UV glue and avoiding a strip around the laser cut channel. The fabrication steps are shown in Figure 4.24. This failed for two reasons. Firstly, it was hard to neatly cover the whole surface with an even thickness of glue. Secondly, staying clear of the area directly next to the channel by a fixed distance was also difficult to achieve by hand.

Spin coating the glue turned out to be a reasonable method for apply a more even and thinner layer of adhesive. The high viscosity of the glue required to use a high rpm and it was difficult to cover the whole surface. To solve the second issues, a temporary tape spacer was created by laser cutting a strip around the channel. This way it was easy to prevent the glue from getting next to or into the channel. After applying the glue, the tape layer could be removed by a tweezer, resulting in a clear are with a well defined boundary to the glue. Different strip thicknesses were tried (between 0.5-3 mm) as shown in Section 4.7. However, when

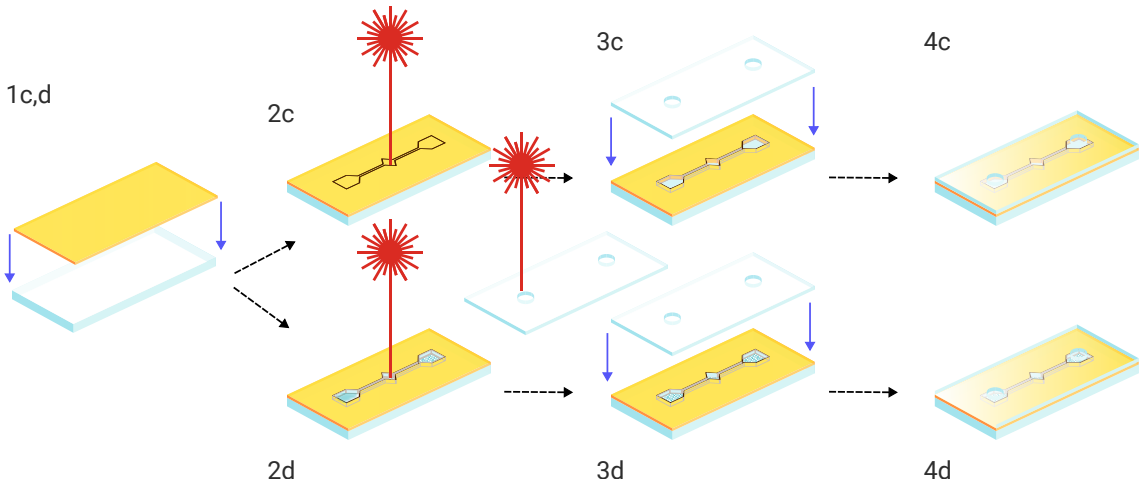


**Figure 4.22:** Schematics showing the fabrication processes of two tape-based devices. After each laser cutting step, the parts are cleaned in an ultrasonic bath for 10 minutes in water. In addition, before the tape (1c,d) is added, the parts are ultrasonically cleaned, first in acetone and then in isopropyl alcohol (IPA), both for 5 minutes. Then they are dried using a regular air gun. These cleaning steps are omitted in the figure.

adding the cover slips, glue still entered the chamber as it was challenging to align the cover slips and apply the right amount of pressure.

**UV gluing with double-sided tape gasket** The previous method was updated with double-sided tape, shown in Section 4.7. The idea behind this was that the tape would not have to be removed as it also functions like an adhesive, albeit less strong than the glue. The tape layer now dictated the height and the glue thickness had to be matched to this. It was however hard to do that by hand and the glue still entered the chamber when the cover slip was placed.

**Piezo bonding** In Figure 4.26 the process of bonding the piezo disk to the chip is presented. This consisted of the following steps:

(a) Cut out a piece of aluminum foil that will act as the ground connection for all piezo disks. Then, apply a droplet of UV glue on the backside of the chip.

(b) Cure the glue for about 5 minutes, depending on the power of the UV lamp.

(c) Apply a droplet of silver paste on top of the aluminum foil.

(d) Place the piezoelectric disks on top of the paste and apply a gentle pressure. Let the paste cure, preferably while maintaining the pressure.

(e) After checking for short-circuits, add cyanoacrylate glue around the edges of the piezo in order to strengthen the bond.

(f) Finalize the chip by soldering the wires to the chip and the aluminum foil ground. To solder to the aluminum foil, gently scratch away the oxide layer shortly before.

## A.5 Validation

To make sure that the chip will work properly, the resistance between the poles of each transducer should be measured using a standard multimeter. It happened multiple times that too much silver paste was applied such that it came out from underneath the piezo disk and made contact with the top electrode as well. If the cyanoacrlate glue was already applied, acetone can be used to gently remove it again using for example a cotten swab.

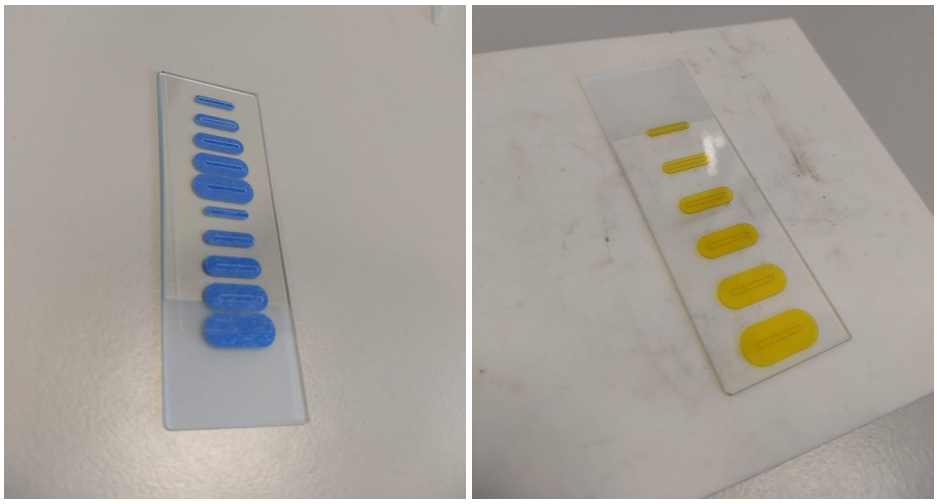

**Figure 4.23:** Photo's of two methods to prevent the UV from entering the chamber when placing the cover slip. (left) A test sample with paper tape strokes of different thickness strips around the chamber. After removing the tape, the uncovered glass area should be free of glue which decreases the odds of clogging the chamber. (right) Double-sided tape test strips with a range of thicknesses to create a barrier for the glue. The tape remains after the glue is applied.

After the connections are checked, the piezoelectric transducers can be tested. Applying a sine wave signal within the audible range (below 20 kHz) is an easy way to verify this should be audible.

The height profile can easily be obtained with the 'depth profile' function in the software of the Keyence digital microscope (Keyence Digital Microscope VHX-6000). The channel edge should be sufficiently zoomed in to get the clearest profile with the least amount of noise. Additionally, a piece of aluminum foil can be placed underneath to improve the lighting.

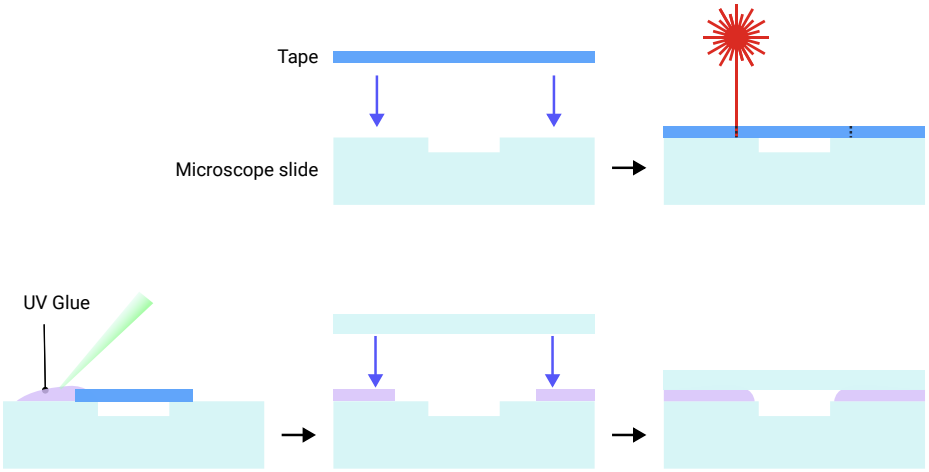


**Figure 4.24:** Schematic of the fabrication method that uses a tape layer to create a distinct boundary when applying the glue in order to keep the glue away from the channel when the cover slip is added.

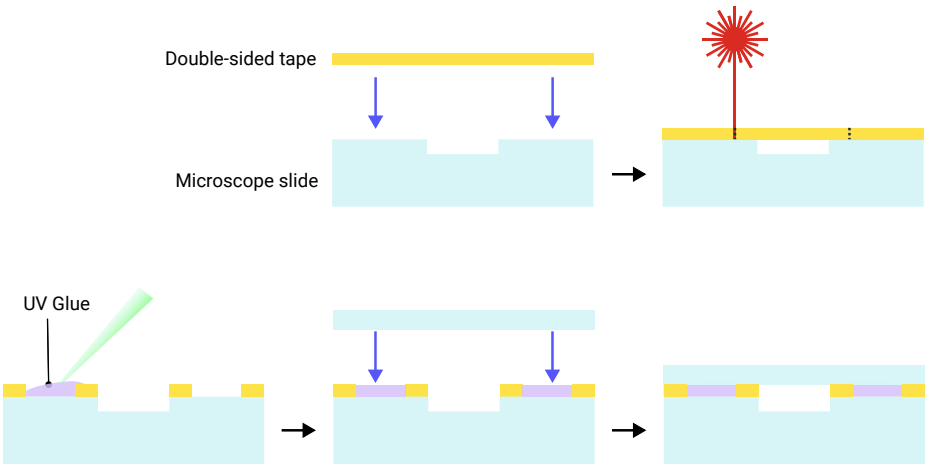


**Figure 4.25:** Schematic of the fabrication method that makes use of the double-sided tape (yellow) as a sealing gasket to prevent the glue (purple) from clogging the channel.

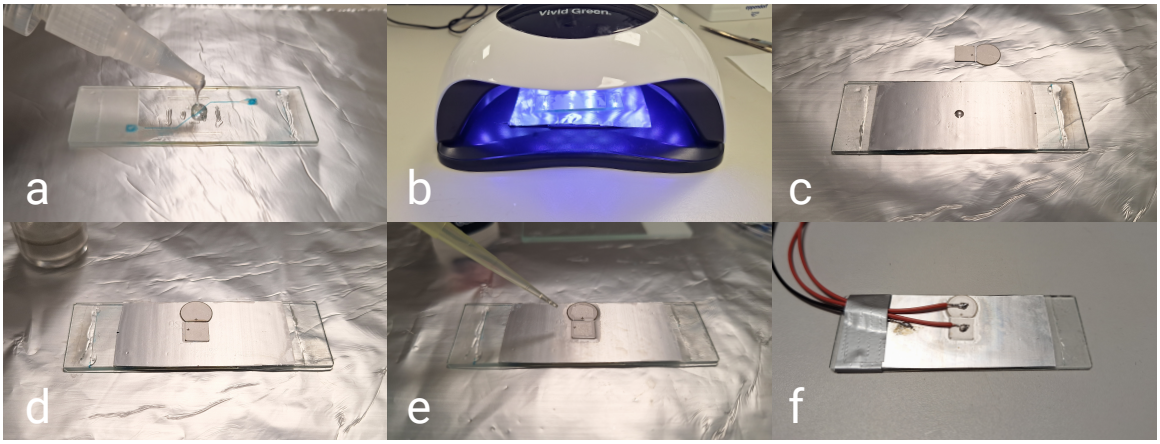


**Figure 4.26:** Bonding process of the piezoelectric disks to the chip.

# Appendix B: Finite element analysis in COMSOL Multiphysics

The COMSOL model was based on the "*3D Acoustic Trap and Thermoacoustic Streaming in Glass Capillary*" model from the Application Gallery on their website [158]. To reduce the computation time, the model was simplified to 2D and streaming and heating effects are left out. The model made use of the Pressure Acoustics, Solid Mechanics, Electrostatics, and Creeping Flow physics components.

The piezoelectric material properties were defined in terms of the strain-charge form, shown in Equation (4.15).

$$S = s_{\mathrm{E}} T + d^{\mathrm{T}} E \tag{4.15a}$$

$$D = dT + \varepsilon_0 \varepsilon_{\mathrm{rT}} E \tag{4.15b}$$

In the first equation expresses the structural strain $S$ in terms of the material compliance $s_{\mathrm{E}}$ (in $\mathrm{Pa}^{-1}$) under constant or zero electric field $E$, the stress $T$ (in Pa), the coupling matrix $d$ (in $\mathrm{C\,N}^{-1}$), and the electric field $E$ (in $\mathrm{N\,C}^{-1}$). In the second equation $E$ is the electric displacement field $D$ (in $\mathrm{C/m}^2$), $\varepsilon_0$ is the permittivity of free space (in $\mathrm{F\,m}^{-1}$), $\varepsilon_{\mathrm{rT}}$ denotes the relative permittivity at constant stress. The material properties of PIC255 are given below.

$$s_{\mathrm{E}} = \begin{bmatrix} 1.38\cdot10^{-11} & -5.699\cdot10^{-12} & -7.376\cdot10^{-12} & 0 & 0 & 0 \\ -5.699\cdot10^{-12} & 2.17\cdot10^{-11} & -7.376\cdot10^{-12} & 0 & 0 & 0 \\ -7.376\cdot10^{-12} & -7.376\cdot10^{-12} & 2.17\cdot10^{-11} & 0 & 0 & 0 \\ 0 & 0 & 0 & 4.492\cdot10^{-11} & 0 & 0 \\ 0 & 0 & 0 & 0 & 4.492\cdot10^{-11} & 0 \\ 0 & 0 & 0 & 0 & 0 & 4.319\cdot10^{-11} \end{bmatrix} \tag{4.16a}$$

$$d = \begin{bmatrix} 0 & 0 & 0 & 0 & 5.35\cdot10^{-10} & 0 \\ 0 & 0 & 0 & 5.35\cdot10^{-10} & 0 & 0 \\ -1.74\cdot10^{-10} & -1.74\cdot10^{-10} & 3.94\cdot10^{-10} & 0 & 0 & 0 \end{bmatrix} \tag{4.16b}$$

$$\varepsilon_{\mathrm{rT}} = \begin{bmatrix} 1649 & 0 & 0 \\ 0 & 1649 & 0 \\ 0 & 0 & 1750 \end{bmatrix} \tag{4.16c}$$

**Table 4.5:** Overview of material properties of PRYY+1119 lead zirconate titanate (PZT) piezoelectric disc transducers

| Property | Symbol | value | Unit |
|---|---|---|---|
| Material | - | PIC255 | - |
| Thickness | $t$ | 0.2 | mm |
| Diameter | $D$ | 10 | mm |
| Quality factor | $Q_{\mathrm{m}}$ | 80 | - |
| Dielectric loss | $\tan(\delta)$ | $20\cdot10^{-3}$ | - |
| Piezo constant | $h_{33}$ | 1.58e9 | V/m |
| Permittivity in polarization direction | $\varepsilon_{33}^{T}/\varepsilon_0$ | 1750 | - |
| Longitudinal speed of sound | $c_{\mathrm{L}}$ | | |
| Density | $\rho$ | 7800 | $\mathrm{kg/m}^3$ |
| Capacitance | $C$ | 5.24 | nF |
| Coupling factor | $k_{\mathrm{p}}$ | 0.62 | - |
| | $k_{\mathrm{t}}$ | 0.47 | - |
| Thickness resonance frequency | $f_{\mathrm{t}}$ | 10 000 | kHz |

To calculate the piezo constant $h_{33}$, the following expression from Kar et al. [159] was used:

$$h_{33}^2 = \frac{k_t^2 c_{33}^D}{\varepsilon_{33}^S} \tag{4.17}$$

The clamped permittivity $\varepsilon_{33}^{S}$ follows from the expression below, as mentioned by Waanders et al. [160]:

$$\varepsilon^{S} = \varepsilon^{T}(1-\kappa^{2}) \tag{4.18}$$

Here, $\varepsilon^{T}$ is the free permittivity and $\kappa$ is the electromechanical coupling coefficient.

**Boundary conditions** An overview of the boundary conditions is shown in Figure 4.27. The acoustic chamber and the surrounding material were coupled through a *Acoustic-Structure Boundary* Multiphysics. The piezoelectric transducers were furthermore connected by the *Piezoelectric Effect* Multiphysics.

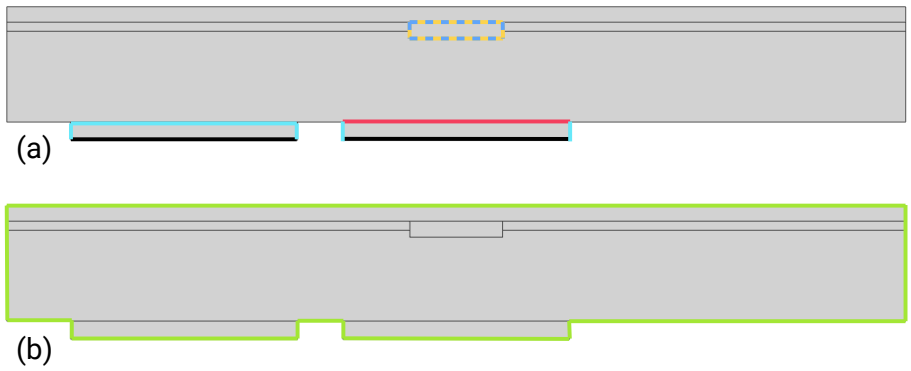


**Figure 4.27:** Overview of the boundary conditions used in the FEM analysis. (a) Boundary conditions for the Electrostatic, Pressure Acoustics and Creeping Flow physics. Yellow denotes the acoustic-structure boundary; dark blue is the no-slip wall condition for the fluid; light-blue indicates zero charge; black is the electric ground; and red is the electric potential. (b) Boundary conditions for the Solid Mechanics physics. Green indicates a free boundary.

# Appendix C: Microfluidic chip electrical characterization

In this section, the electrical characterization of the chip using a frequency response analyzer (FRA) is discussed. The Moku:Pro could also be used for this and the example of a two-port inductance measurement on their website is followed [161]. The FRA works by driving a sine wave over a frequency range and, at the same time, measuring the signal at the two inputs. This way, it is possible to construct the transfer function of the device under test (DUT) in the form of a Bode plot, containing information on the magnitude and the phase over the swept frequency.

To keep the voltage over the piezoelectric disk constant, a 50 Ω resistor was added in parallel to the piezo. The electrical measurement circuit is shown in Figure 4.28 below.

The input impedance $Z_{\text{in}}$ of input 1 and 2 and the output impedance $Z_{\text{out}}$ are all set to 50 Ω.

The impedance $Z_{\text{p}}$ of the piezo that is connected to the microfluidic chip can be now be determined over a frequency range. In this case, this is done by measuring the power ($P_{\text{in},i}$ in dB m). The input voltages $V_{\text{in},1}$ and $V_{\text{in},2}$ can then be calculated as follows:

$$V_{\text{in},i} = \sqrt{\frac{8R_{\text{in},1}}{1000}\left(10^{\frac{P_{\text{in},i}}{10}}\right)} \tag{4.19}$$

The impedance of the piezo follows from applying Ohm's law. For convenience, the impedance of the piezo $Z_{\text{p}}$ and the parallel resistor $R_3$ are first combined into an equivalent resistance $R_{\text{eq}}$.

$$R_{\text{eq}} = R_1\left(\frac{V_2}{V_1}\right) - R_1 \tag{4.20}$$

$$R_{\text{p}} = \frac{R_{\text{p}}R_{\text{eq}}}{R_p - R_{\text{eq}}} \tag{4.21}$$

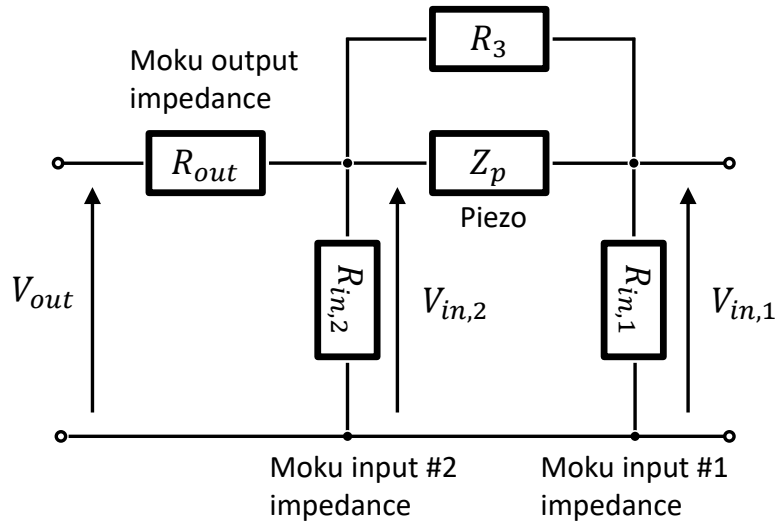


**Figure 4.28:** Schematic of the measurement setup for to perform a frequency response analysis (FRA).

Now the reactance can be calculated from the phase difference ($\phi_2 - \phi_1$) and the resistance $R_\mathrm{p}$.

$$X_\mathrm{p} = \tan\left((\phi_2 - \phi_1) \cdot \frac{\pi}{180}\right) \cdot R_\mathrm{p} \tag{4.22}$$

Finally, the impedance is constructed by adding the resistance $R_\mathrm{p}$ and reactance $X_\mathrm{p}$ together:

$$Z_\mathrm{p} = R_\mathrm{p} + j \cdot X_\mathrm{p} \tag{4.23}$$

# Bibliography


[1] Sleen, L. M. V. D.; Tych, K. M. *nanomaterials* **2021**, *11*, DOI: 10.3390/nano11092424.

[2] Bustamante, C. J.; Chemla, Y. R.; Liu, S.; Wang, M. D. *Nature Reviews Methods Primer* **2021**, DOI: 10.1038/s43586-021-00021-6.

[3] Pesce, G.; Jones, P. H.; Maragò, O. M.; Volpe, G. *Eur. Phys. J. Plus* **2020**, *135*, 949.

[4] Viljoen, A.; Mathelié-Guinlet, M.; Ray, A.; Strohmeyer, N.; Oh, Y. J.; Hinterdorfer, P.; Müller, D. J.; Alsteens, D.; Dufrêne, Y. F. *Nature Reviews Methods Primers* **2021**, *1*, DOI: 10.1038/s43586-021-00062-x.

[5] Sarkar, R.; Rybenkov, V. V. *Front. Phys* **2016**, *4*, 48.

[6] Neuman, K. C.; Nagy, A. *Nature Methods* **2008**, DOI: 10.1038/NMETH.1218.

[7] Evander, M.; Nilsson, J. *Lab on a Chip* **2012**, *12*, 4667–4676.

[8] Sitters, G.; Kamsma, D.; Thalhammer, G.; Ritsch-Marte, M.; Peterman, E. J. G.; Wuite, G. J. L. *Nature Methods* **2015**, *12*, DOI: 10.1038/nMeth.3183.

[9] Mandal, S. S. *ACS Omega* **2020**, *5*, 11271–11278.

[10] Schönfelder, J.; Sancho, D. D.; Perez-Jimenez, R. *Journal of Molecular Biology* **2016**, *428*, 4245–4257.

[11] Miller, H.; Zhou, Z.; Shepherd, J.; Wollman, A. J.; Leake, M. C. *Reports on Progress in Physics* **2018**, *81*, DOI: 10.1088/1361-6633/aa8a02.

[12] Leake, M. C. *Methods (Elsevier)* **2021**, *193*, 1–4.

[13] Lyubchenko, Y. L., *An Introduction to Single Molecule Biophysics*, 2017.

[14] Moerner, W. E. *The Journal of Physical Chemistry B* **2002**, DOI: 10.1021/jp012992g.

[15] Deniz, A. A.; Mukhopadhyay, S.; Lemke, E. A. *Journal of The Royal Society Interface* **2007**, *5*, 15–45.

[16] Shan, Y. *Membrane Biophysics: New Insights and Methods* **2017**, 91–115.

[17] Zhao, D.; Liu, S.; Gao, Y. *Acta Biochimica et Biophysica Sinica* **2018**, *50*, 231–237.

[18] Ashkin, A.; Dziedzic, J. M.; Bjorkholm, J. E.; Chu, S. *Opt. Lett.* **1986**, *11*, 288–290.

[19] Camunas-Soler, J.; Ribezzi-Crivellari, M.; Ritort, F. *Annual Review of Biophysics* **2016**, *45*, 65–84.

[20] Jiao, J.; Rebane, A. A.; Ma, L.; Zhang, Y. In *Optical Tweezers: Methods and Protocols*, Gennerich, A., Ed.; Springer New York: New York, NY, 2017, pp 357–390.

[21] Bustamante, C.; Alexander, L.; Maciuba, K.; Kaiser, C. M. *Annu Rev Biochem* **2020**, *89*, 443–470.

[22] Kaseda, K.; Higuchi, H.; Hirose, K. *Nature Cell Biology* **2003**, *5*, DOI: 10.1038/ncb1067.

[23] Lisica, A.; Grill, S. W. *Biomolecular Concepts* **2017**, *8*, 1–11.

[24] Binnig, G.; Quate, C. F.; Gerber, C. *Phys. Rev. Lett.* **1986**, *56*, 930–933.

[25] Serdiuk, T.; Mari, S. A.; Müller, D. J. *Nano Letters* **2017**, *17*, PMID: 28627175, 4478–4488.

[26] Grandbois, M.; Beyer, M.; Rief, M.; Clausen-Schaumann, H.; Gaub, H. E. *Science* **1999**, *283*, 1727–1730.

[27] Marshall, B. T.; Long, M.; Piper, J. W.; Yago, T.; McEver, R. P.; Zhu, C. *Nature* **2003**, *423*, 190–193.

[28] Lee, G. U.; Chrisey, L. A.; Colton, R. J. *Science* **1994**, *266*, 771–773.

[29] Vlaminck, I. D.; Dekker, C. *Annual Review of Biophysics* **2012**, *41*, 453–472.

[30] Neuman, K. C.; Lionnet, T.; Allemand, J. F. *Annual Review of Materials Research* **2007**, *37*, 33–67.

[31] Vilfan, I. D.; Lipfert, J.; Koster, D. A.; Lemay, S. G.; Dekker, N. H. In *Handbook of Single-Molecule Biophysics*, Hinterdorfer, P., Oijen, A., Eds.; Springer US: New York, NY, 2009, pp 371–395.

[32] Revyakin, A.; Liu, C.; Ebright, R. H.; Strick, T. R. *Science* **2006**, *314*, 1139–1143.

[33] Cui, Y.; Petrushenko, Z. M.; Rybenkov, V. V. *Nature Structural & Molecular Biology* **2008**, *15*, DOI: 10.1038/nsmb.1410.

[34] Rufo, J.; Cai, F.; Friend, J.; Wiklund, M.; Huang, T. J. *Nature Reviews Methods Primers* **2022**, *2*, DOI: 10.1038/s43586-022-00109-7.

[35] Ozcelik, A.; Rich, J.; Huang, T. J. In Elsevier: 2021, pp 297–321.

[36] *Springer Handbook of Acoustics*, 1st ed.; Rossing, T. D., Ed.; Springer: 2007.

[37] Baudoin, M.; Thomas, J. L. *Annual Review of Fluid Mechanics* **2020**, *52*, 205–234.

[38] Ozcelik, A.; Rufo, J.; Guo, F.; Gu, Y.; Li, P.; Lata, J.; Huang, T. J. **2018**, *15*, DOI: 10.1038/s41592-018-0222-9.

[39] Yang, S.; Tian, Z.; Wang, Z.; Rufo, J.; Li, P.; Mai, J.; Xia, J.; Bachman, H.; Huang, P.-H.; Wu, M.; Chen, C.; Lee, L. P.; Huang, T. J. **2022**, *21*, DOI: 10.1038/s41563-022-01210-8.

[40] Tsan, V.-H. Numerical and experimental trapping analysis of simple and cost-effective acoustic tweezers, 2022.

[41] Lim, H. G.; Li, Y.; Lin, M.-Y.; Yoon, C.; Lee, C.; Jung, H.; Chow, R. H.; Shung, K. K. *IEEE Transactions on Ultrasonics, Ferroelectrics, and Frequency Control* **2016**, *63*, 1988–1995.

[42] Dholakia, K.; Drinkwater, B. W.; Ritsch-Marte, M. *Nature Reviews Physics* **2020**, *2*, 480–491.

[43] Jeger-Madiot, N.; Mousset, X.; Dupuis, C. *Citation: The Journal of the Acoustical Society of America* **2022**, *151*, 4165.

[44] Peterman, E.; Gittes, F.; Schmidt, C. *Biophysical Journal* **2003**, *84*, Part 1, 1308–1316.

[45] Blázquez-Castro, A. *Micromachines* **2019**, *10*, DOI: 10.3390/mi10080507.

[46] Wiklund, M. *Lab on a Chip* **2012**, *12*, 2018–2028.

[47] Lenshof, A.; Magnusson, C.; Laurell, T. *Lab on a Chip* **2012**, *12*, 1210–1223.

[48] Devendran, C.; Carthew, J.; Frith, J. E.; Neild, A.; Devendran, C.; Neild, A.; Carthew, J.; Frith, J. E. **2019**, DOI: 10.1002/advs.201902326.

[49] Zhang, S.; Wang, Y.; Onck, P.; Toonder, J. D. **2020**, *24*, 24.

[50] Dulin, D.; Berghuis, B. A.; Depken, M.; Dekker, N. H. *Current Opinion in Structural Biology* **2015**, *34*, 116–122.

[51] Hill, F. R.; Monachino, E.; Oijen, A. M. V. *Biochemical Society Transactions* **2017**, *45*, 759–769.

[52] King, L. V. *Proc. R. Soc. London A* **1934**, *147*, 212–240.

[53] Sollner, B. K.; Bondy, C. *Trans. Faraday Soc.* **1936**, *32*, 616–623.

[54] Trampler, F.; Sonderhoff, S. A.; Pui, P. W. S.; Kilburn, D. G.; Piret, J. M. *Nature Publishing Group* **1994**, *12*, 281–284.

[55] Meng, L.; Cai, F.; Li, F.; Niu, L.; Zheng, H. *Journal of Physics D: Applied Physics To* **2019**, *52*, 273001.

[56] Bruus, H. *Lab on a Chip* **2012**, *12*, 1578–1586.

[57] Akkoyun, F.; Gucluer, S.; Ozcelik, A. *Biomicrofluidics* **2021**, *15*, 61301.

[58] Rayleigh, L. *Proceedings of the London Mathematical Society* **1885**, *s1-17*, 4–11.

[59] Gedge, M.; Hill, M. *Lab on a Chip* **2012**, *12*, 2998–3007.

[60] Gao, Y.; Wu, M.; Lin, Y.; Xu, J. *Micromachines* **2020**, *11*, DOI: 10.3390/mi11100921.

[61] Johnson, D. A.; Feke, D. L. *Separations Technology* **1995**, *5*, 251–258.

[62] Ahmed, H.; Destgeer, G.; Park, J.; Afzal, M.; Sung, H. J. *Analytical Chemistry* **2018**, *90*, PMID: 29911381, 8546–8552.

[63] Xie, Y.; Bachman, H.; Huang, T. J. *TrAC - Trends in Analytical Chemistry* **2019**, *117*, 280–290.

[64] Manneberg, O. Multidimensional ultrasonic standing wave manipulation in microfluidic chips, 2009.

[65] Gesellchen, F.; Bernassau, A. L.; Déjardin, T.; Cumming, D. R. S.; Riehle, M. O. **2014**, *14*, 2266.

[66] Drinkwater, B. W. *Lab Chip* **2016**, *16*, 2360–2375.

[67] Bruus, H. *Lab on a Chip* **2012**, *12*, 20–28.

[68] Bruus, H. *Lab on a Chip* **2012**, *12*, 1014–1021.

[69] Yosioka, K.; Kawasima, Y. *Acta Acustica united with Acustica* **1955**, *5*.

[70] Gor'kov, L. *Soviet Physics Doklady* **1962**, *6*, 773.

[71] Collins, D. J.; Morahan, B.; Garcia-Bustos, J.; Doerig, C.; Plebanski, M.; Neild, A. **2015**, DOI: 10.1038/ncomms9686.

[72] Silva, G. T.; Lopes, J. H.; Leão-Neto, J. P.; Nichols, M. K.; Drinkwater, B. W. *Physical Review Applied* **2019**, *11*, 054044.

[73] Sepehrirahnama, S.; Mohapatra, A. R.; Oberst, S.; Chiang, Y. K.; Powell, D. A.; Lim, K. M. *Lab on a Chip* **2022**, DOI: 10.1039/d2lc00447j.

[74] Dual, J.; Schwarz, T. *Lab on a Chip* **2012**, *12*, 244–252.

[75] Moiseyenko, R. P.; Bruus, H. *Physical Review Applied* **2019**, *11*, DOI: 10.1103/PhysRevApplied.11.014014.

[76] Sadhal, S. S. *Lab on a Chip* **2012**, *12*, 2292–2300.

[77] Bruus, H. *Lab on a Chip* **2011**, *11*, 3742–3751.

[78] Gupta, N.; Suman; Yadav, S. K. *Advance in Electronic and Electric Engineering* **2014**, *4*, 313–318.

[79] Dual, J.; Möller, D. *Lab on a Chip* **2012**, *12*, 506–514.

[80] Lenshof, A.; Magnusson, C.; Laurell, T. *Lab on a Chip* **2012**, *12*, 1210–1223.

[81] Oberti, S.; Neild, A.; Dual, J. *The Journal of the Acoustical Society of America* **2007**, *121*, 778.

[82] Qiu, W.; Baasch, T.; Laurell, T. *PHYSICAL REVIEW APPLIED* **2022**, *17*, 44043.

[83] Tahmasebipour, A.; Friedrich, L.; Begley, M. *Citation: The Journal of the Acoustical Society of America* **2020**, *148*, 359.

[84] Manneberg, O.; Svennebring, J.; Hertz, H. M.; Wiklund, M. *J. Micromech. Microeng* **2008**, *18*, 9.

[85] Owens, C. E.; Shields, C. W.; Cruz, D. F.; Charbonneau, P.; López, G. P. *Soft Matter* **2016**, *12*, 717–728.

[86] Hou, Z.; Zhou, Z.; Liu, P.; Pei, Y. *Extreme Mechanics Letters* **2020**, *37*, DOI: 10.1016/j.eml.2020.100716.

[87] Wang, C.; Ma, Y.; Chen, —. Z.; Wu, Y.; Song, —. F.; Qiu, J.; Shi, —. M.; Wu, —. X.; Wu, X. **2021**, DOI: 10.1002/cyto.a.24362.

[88] Johansson, L.; Nilsson, M.; Lilliehorn, T.; Almqvist, M.; Nilsson, J.; Laurell, T.; Johansson, S. **2005**.

[89] Zhou, Q.; Lam, K. H.; Zheng, H.; Qiu, W.; Shung, K. K. **2014**, DOI: 10.1016/j.pmatsci.2014.06.001.

[90] Kamsma, D.; Creyghton, R.; Sitters, G.; Wuite, G. J.; Peterman, E. J. *Methods* **2016**, *105*, Gives a good summary of the steps of an AFS experiment.¡br/¿, 26–33.

[91] Visscher, K.; Block, S. M. *Methods in Enzymology* **1998**, *298*.

[92] Berg-Sørensen, K.; Flyvbjerg, H. *Review of Scientific Instruments* **2004**, *75*, 594–612.

[93] Kamsma, D.; Wuite, G. J. *Methods in Molecular Biology* **2018**, *1665*, 341–351.

[94] Granéli, A.; Yeykal, C. C.; Prasad, K.; Greene, E. C. **2006**, DOI: 10.1021/la051944a.

[95] Fazio, T.; Visnapuu, M.-L.; Wind, S.; Greene, E. C. *Langmuir* **2008**, *24*, 10524‘–10531.

[96] Liu, W.; Gao, H.; Liu, K.; Lei, D.; Pei, K.; Hu, G. **2022**, DOI: 10.1007/s11051-022-05461-z.

[97] Habibi, R.; Devendran, C.; Neild, A. **2017**, *17*, 3279.

[98] Glynne-Jones, P.; Boltryk, R. J.; Harris, N. R.; Cranny, A. W.; Hill, M. *Ultrasonics* **2010**, *50*, 68–75.

[99] Shaglwf, Z.; Hammarström, B.; Laila, D. S. *Citation: The Journal of the Acoustical Society of America* **2019**, *145*, 945.

[100] Hou, Z.; Li, J.; Zhou, Z.; Pei, Y. *International Journal of Mechanical Sciences* **2022**, *222*, DOI: 10.1016/J.IJMECSCI.2022.107232.

[101] Kandemir, M. H.; Beelen, M.; Wagterveld, R. M.; Yntema, D. R.; Keesman, K. J. *Journal of Sound and Vibration* **2021**, *490*, DOI: 10.1016/J.JSV.2020.115723.

[102] Courtney, C. R.; Ong, C. K.; Drinkwater, B. W.; Bernassau, A. L.; Wilcox, P. D.; Cumming, D. R. *Proceedings of the Royal Society A: Mathematical, Physical and Engineering Sciences* **2012**, *468*, 337–360.

[103] Tian, L.; Martin, N.; Bassindale, P. G.; Patil, A. J.; Li, M.; Barnes, A.; Drinkwater, B. W.; Mann, S. *Nature Communications 2016 7:1* **2016**, *7*, 1–10.

[104] Manneberg, O.; Vanherberghen, B.; Onfelt, B.; Wilklund, M. *Lab on a Chip* **2009**, *9*, 741–848.

[105] Sriphutkiat, Y.; Zhou, Y. *Sensors and Actuators, A: Physical* **2017**, *263*, 521–529.

[106] Courtney, C. R. P. In *2021 IEEE International Ultrasonics Symposium (IUS)*, 2021, pp 1–4.

[107] Cox, L.; Croxford, A.; Drinkwater, B. W. *Scientific Reports* **2022**, *12*, DOI: 10.1038/s41598-022-18554-5.

[108] Liu, Y.; Lim, K.-M. *Lab Chip* **2011**, *11*, 3167–3173.

[109] Zhou, W.; Niu, L.; Cai, F.; Li, F.; Wang, C.; Huang, X.; Wang, J.; Wu, J.; Meng, L.; Zheng, H. **2016**, DOI: 10.1063/1.4954934.

[110] Ding, X.; Shi, J.; Lin, S.-C. S.; Yazdi, S.; Kiraly, B.; Huang, T. J. **2012**, DOI: 10.1039/c2lc21021e.

[111] Ding, X.; Lin, S. C. S.; Kiraly, B.; Yue, H.; Li, S.; Chiang, I. K.; Shi, J.; Benkovic, S. J.; Huang, T. J. *Proceedings of the National Academy of Sciences of the United States of America* **2012**, *109*, 11105–11109.

[112] Weser, R.; Deng, Z.; Kondalkar, V. V.; Darinskii, A. N.; Cierpka, C.; Schmidt, H.; König, J. *Lab Chip* **2022**, *22*, 2886–2901.

[113] Guo, F.; Mao, Z.; Chen, Y.; Xie, Z.; Lata, J. P.; Li, P.; Ren, L.; Liu, J.; Yang, J.; Dao, M.; Suresh, S.; Huang, T. J. *Proceedings of the National Academy of Sciences of the United States of America* **2016**, *113*, 1522–1527.

[114] Mameren, J. V.; Gross, P.; Farge, G.; Hooijman, P.; Modesti, M.; Falkenberg, M.; Wuite, G. J.; Peterman, E. J. *Proceedings of the National Academy of Sciences of the United States of America* **2009**, *106*, 18231–18236.

[115] Hawkes, J. J.; Benes, E.; Wien, T. U. Positioning particles within liquids using ultrasound force fields Vibrations of Human cells View project, 2002.

[116] Groschl, M. *ACUSTICA. acta acustica* **1998**, *84*, 432–447.

[117] Aralekallu, S.; Boddula, R.; Singh, V. *Materials & Design* **2023**, *225*, DOI: 10.1016/j.matdes.2022.111517.

[118] Hwang, J.; Young, ·.; Cho, H.; Park, M. S.; Kim, B. H. *International Journal of Precision Engineering and Manufacturing* **2019**, *20*, 479–495.

[119] Physik Instrumente (PI) GmbH &; Co. KG, https://www.physikinstrumente.com/en/products/piezoelectric-transducers-actuators/disks-rods-and-cylinders/piezoelectric-discs-1206710.

[120] Hahn, S. P.; Hahn, P.; Schwab, O.; Dual, J. **2015**, *14*, 3937.

[121] COMSOL Blog; Damping in Structural Dynamics: Theory and Sources, https://www.comsol.com/blogs/damping-in-structural-dynamics-theory-and-sources/, Online; accessed: 2023-09-12.

[122] Norland Optical Adhesive 61, https://www.norlandprod.com/adhesives/noa61pg2.html, Online; accessed: 2023-09-10.

[123] Dong, S.-S.; Shao, W.-Z.; Yang, L.; Ye, H.-J.; Zhen, L. *RSC Advances* **2018**, *8*, 28152–28160.

[124] Scott, S. M.; Ali, Z. *Micromachines 2021, Vol. 12, Page 319* **2021**, *12*, DOI: 10.3390/MI12030319.

[125] Queste, S.; Salut, R.; Clatot, S.; Rauch, J.-y.; Malek, C. G. K. *Microsyst Technol* **2010**, *16*, 1485–1493.

[126] Lin, Z.; Hong, M. *Ultrafast Science* **2021**, *2021*, DOI: 10.34133/2021/9783514.

[127] Wiklund, M.; Önfelt, B. In Humana Press: 2012, pp 177–196.

[128] Dual, J.; Hahn, P.; Leibacher, I.; Möller, D.; Schwarz, T. *Lab on a Chip* **2012**, *12*, 852–862.

[129] Sherrit, S.; Leary, S. P.; Dolgin, B. P.; Bar-Cohen, Y. *Proceedings of the IEEE Ultrasonics Symposium* **2000**.

[130] Mason, W. P., *Electromechanical Transducers and Wave Filters,* Van Nostrand: Princeton, NJ, 1948, pp 201–209, 399–404.

[131] Krimholtz, R.; Leedom, D. A.; Matthaei, G. L. *Electronics Letters* **1970**, *6*, 398–399.

[132] Kar, B.; Wallrabe, U. *Micromachines* **2020**, *11*, DOI: 10.3390/MI11040355.

[133] Hill, M.; Shen, Y.; Hawkes, J. J. *Ultrasonics* **2002**, *40*, 385–392.

[134] Manzo, C.; Garcia-Parajo, M. F. *Reports on Progress in Physics* **2015**, *78*, DOI: 10.1088/0034-4885/78/12/124601.

[135] Barnkob, R.; Kähler, C. J.; Rossi, M. *Lab Chip* **2015**, *15*, 3556–3560.

[136] Parthasarathy, R. *Nature Methods* **2012**, *9*, 724–726.

[137] Loenhout, M. T. V.; Kerssemakers, J. W.; Vlaminck, I. D.; Dekker, C. *Biophysical Journal* **2012**, *102*, 2362–2371.

[138] Cheezum, M. K.; Walker, W. F.; Guilford, W. H. *Biophysical Journal* **2001**, *81*, 2378–2388.

[139] Kashkanova, A. D.; Shkarin, A. B.; Mahmoodabadi, R. G.; Blessing, M.; Tuna, Y.; Gemeinhardt, A.; Sandoghdar, V. *Optics Express* **2021**, *29*, 11070–11083.

[140] Augustsson, P.; Laurell, T. *Lab on a Chip* **2012**, *12*, 1742–1752.

[141] Yang, S.; Tian, Z.; Wang, Z.; Rufo, J.; Li, P.; Mai, J.; Xia, J.; Bachman, H.; Huang, P.-H.; Wu, M.; Chen, C.; Lee, L. P.; Huang, T. J. *Nature Materials* **2022**, *21*, 540–546.

[142] Barnkob, R.; Augustsson, P.; Laurell, T.; Bruus, H. *Lab on a Chip* **2010**, *10*, 563–570.

[143] Evander, M.; Lenshof, A.; Laurell, T.; Nilsson, J. *Analytical Chemistry* **2008**, *80*, 5178–5185.

[144] Lenshof, A.; Evander, M.; Laurell, T.; Nilsson, J. *Lab on a Chip* **2012**, *12*, 684–695.

[145] Glynne-Jones, P.; Boltryk, R. J.; Hill, M. *Lab on a Chip* **2012**, *12*, 1417–1426.

[146] Nilsson, A.; Petersson, F.; Jönsson, H.; Laurell, T. *Lab on a Chip* **2004**, *4*, 131–135.

[147] Shu, X.; Liu, H.; Zhu, Y.; Cai, B.; Jin, Y.; Wei, Y.; Zhou, F.; Liu, W.; Guo, S. *Microfluidics and Nanofluidics* **2018**, *22*, DOI: 10.1007/s10404-018-2052-6.

[148] Kim, S.; Kim, J.; Joung, Y. H.; Choi, J.; Koo, C. *Micromachines* **2018**, *9*, DOI: 10.3390/mi9120639.

[149] Wlodarczyk, K. L.; Hand, D. P.; Maroto-Valer,
bibinitperiod M. M. *Scientific Reports* **2019**, *9*, DOI: 10.1038/s41598-019-56711-5.

[150] Li, M.; Yue, L.; Rajan, A. C.; Yu, L.; Sahu, H.; Montgomery, S. M.; Ramprasad, R.; Qi, H. J. *Science Advances* **2023**, *9*, eadi2958.

[151] Abbondanzieri, E. A.; Greenleaf, W. J.; Shaevitz, J. W.; Landick, R.; Block, S. M. *Nature* **2005**, *438*, 460–465.

[152] Heller, I.; Dulin, D.; Editors, E. J. G. P., *Single Molecule Analysis: Methods and Protocols*, 2018; Vol. 3.

[153] Nava, G.; Bragheri, F.; Yang, T.; Minzioni, P.; Osellame, R.; Cristiani, I.; Berg-Sørensen, K. *Microfluidics and Nanofluidics* **2015**, *19*, 837–844.

[154] VWR, https://nl.vwr.com/store/, Online; accessed: 2023-09-14.

[155] https://shop.metrology.zeiss.fi/INTERSHOP/web/WFS/IMT-FI-Site/en_FI/-/EUR/ViewProduct-Start?SKU=000000-0630-060, Online; accessed: 2023-10-12.

[156] Farnell, https://nl.farnell.com/, Online; accessed: 2023-09-18.

[157] Marcune, V.; Iles, S. Understanding Surface Roughness, https://www.edmundoptics.in/knowledge-center/application-notes/optics/understanding-surface-roughness/, Online; accessed: 2023-11-30.

[158] https://www.comsol.com/model/3d-acoustic-trap-and-thermoacoustic-streaming-in-glass-capillary-105991, Online; accessed: 2023-10-10.

[159] Kar, B.; Basaeri, H.; Roundy, S.; Wallrabe, U. *Smart Materials and Structures* **2023**, *32*, DOI: 10.1088/1361-665X/acdd39.

[160] Waanders, J. Piezoelectric Ceramics - Properties and Applications, 1991.

[161] https://www.liquidinstruments.com/blog/2023/01/13/impedance-measurements-a-guide-to-measuring-impedance-with-mokulabs-frequency-response-analyzer-part-2-inductance/, Online; accessed: 2023-10-10, 2023.